VNIVERSITAT DE VALÈNCIA

Facultad de Física
Departamento de Física Aplicada

Producción de Nanopartículas metálicas y semiconductoras por ablación láser: propiedades estructurales, ópticas y aplicaciones

(Production of metallic and semiconductor nanoparticles by laser ablation: structural and optical properties and applications)

TESIS DOCTORAL

Presentada por:

Kamal Abderrafi

Dirigida por:

Juan P. Martínez Pastor
Vladimir Chyrvony

Valencia, Noviembre 2013

A mis Padres ....

عندما تشتد بي رياح الحزن .. أبحث عن بقعة أرض تحتويني .. بقعة من الأرض أنزف الحزن عليها .. عندها أتذكرك .. ابـــــــــــي..؛ عندما أجلس اتفقدك بين كتاب العمر.. وأقرأ سطور تاريخك العظيم .. يأخذني الحنين اليك .. ابـــــــــــي ..؛ عندما أسير بينهم ..وفي زحامهم يملأني إحساس باليتم .. أسافر بخيالي وأزورك في قبرك.. أتجول بين القبور .. وانا ارتدي وشاح الالم .. ابـــــــــــي ..؛ عندما أصاب بالمرض وأشعر بالوهن يتملكني الألم.. أشهى حنانك كالحلم ..وتتضخم حاجتي اليك .. لم أعترض يوما لرحيلك انما هي الحاجه لحنانك .. ابـــــــــــي ..؛ مازلت أكتب اسمك على الرمال .. كثيرا ماقالوا لي ستكبر ستنسي ..؛ لكن ابت معارك الايام أن تنتهي ..؛ مازلت أشعر في ماساة رحيلك ..؛ وكلما اصطبغت إكذوبة النسيان ..؛ وجدت ان الكون كله يختفي .. فيغيب أهل الأرض .. ولا يتبقى أمامي سوى اسمي وانت ترده ..؛ ومازالت شواطئك لاتعرف الرحيل ..؛ :: اهديها الي روح ابـــــــــــي..... الله يرحمـــــــك في جنان النعيمـــ ابـــــــي الحبيبـــــــ

INSTITUT DE CIÈNCIA DELS MATERIALS de la Universitat de València
ICMUV
Apdo. Oficial 22085
46071 VALENCIA

Juan P. Martínez Pastor
Catedrático de Física Aplicada
Unidad de Materiales y Dispositivos
(www.uv.es/umdo)
Tfn. +34963544793
Fax.+34963543633
e-mail: martinep@uv.es

Los abajo firmantes, D. Vladimir Chyrvony, Investigador contratado de la Universitat de València, y D. Juan P. Martinez Pastor, Catedrático de Física Aplicada de la Universitat de València,

INFORMAN

Que la tesis doctoral, titulada *"Producción de Nanopartículas metálicas y semiconductoras por ablación láser: propiedades estructurales, ópticas y aplicaciones"* ha sido realizada bajo nuestra dirección por el licenciado D. Kamal Abderrafi, y reúne los requisitos de originalidad y relevancia científica para optar al grado de Doctor en Física.

Y para que así conste, en cumplimiento de la legislación vigente, damos nuestro visto bueno y autorización para que se presente la referida Tesis Doctoral en la Facultad de Física de la Universitat de València, firmando el presente informe en

Paterna, a 18 de Noviembre de 2013

Fdo.: Juan P. Martínez Pastor Fdo.: Vladimir Chyrvony

Contents

Agradecimientos

Al finalizar un trabajo tan arduo y lleno de dificultades como el desarrollado en una tesis doctoral es inevitable que te asalte un muy humano egocentrismo que te lleva a concentrar la mayor parte del mérito en la aportación realizada por uno mismo. Sin embargo, el análisis objetivo te muestra inmediatamente que hubiese sido imposible sin la participación de personas e instituciones que han facilitado las cosas para que este trabajo llegue a un feliz término. Por ello, es para mí un verdadero placer utilizar este espacio para ser justo y consecuente, expresándoles a todos mis agradecimientos.

Debo agradecer de manera especial y sincera al Profesor Juan P. Martínez Pastor por aceptarme para realizar esta tesis doctoral bajo su dirección. Su apoyo y confianza en mi trabajo y su capacidad para guiar mis ideas han supuesto una aportación fundamental, no solamente para el desarrollo de esta tesis, sino también para mi formación como investigador. Las ideas propias, siempre enmarcadas en su orientación y rigurosidad, han sido la clave del buen trabajo que hemos realizado juntos, el cual no se puede concebir sin su siempre oportuna participación. Le agradezco también el haberme facilitado siempre los medios suficientes para llevar a cabo todas las actividades propuestas durante el desarrollo de esta tesis. Muchas gracias, Profesor.

Quiero expresar también mi más sincero agradecimiento al Dr. Vladimir Chivrony su importante aportación y participación activa en el desarrollo de esta tesis. Debo destacar, por encima de todo, su disponibilidad y paciencia, que hizo que nuestras siempre acaloradas discusiones redundaran beneficiosamente, tanto en el plano científico como en el personal. No cabe duda que su participación ha enriquecido enormemente el trabajo realizado. También quiero expresar mi más sincero reconocimiento al Dr. Ernesto Jiménez por su colaboración científica y amistad durante el comienzo de mi tesis.

Quiero extender un sincero agradecimiento al Dr. Rafael Abargues, por su paciencia, disponibilidad y generosidad para compartir su experiencia y amplio conocimiento sobre los aspectos químicos relativos a la fabricación de los nanomateriales estudiados en esta tesis doctoral, además de agradecer sus rápidas respuestas a las diferentes inquietudes surgidas durante el desarrollo de este trabajo, lo cual se ha visto también reflejado en los buenos

resultados obtenidos. Igualmente, aprovecho para agradecer la colaboración estrecha con D. Raúl García Calzada en una parte de los experimentos desarrollados en esta tesis doctoral (preparación de nanopartículas de silicio).

Para mis demás compañeros del grupo UMDO tengo sólo palabras de agradecimiento, especialmente por aquellos momentos en los que pude ser inferior a sus expectativas: ha sido un camino largo y duro en el que, algunas veces, la fijación por lograr tus objetivos te hace olvidar la importancia del contacto humano. Sin embargo, como en todas las actividades de la vida, siempre al final hay algunos criterios que te permiten priorizar, y es por ello que debo resaltar mis agradecimientos para algunas personas. Quiero expresar mi agradecimiento especial al Dr. Josep Canet quien fue un compañero siempre generoso y dispuesto como pocos, que compartió conocimientos y experiencias de tipo profesional y personal que fueron de gran valor. Para el resto de compañeros: Pepe, Esteban, Jose, Lorenzo, Guillermo, Alejandro, Maribel, Sandra, Rachid, Karim, Isaac, Pedro, Jamal, mil y mil gracias! Hago extensivo este agradecimiento a todos los miembros del Instituto de Ciencia de los Materiales de la Universidad de Valencia (ICMUV).

Finalmente, muchas gracias a la Dra. Luisa González y a todo su grupo por permitirme vivir una experiencia tan importante para mi formación como investigador en el IMM (CNM-CSIC), con especial mencionar a los Drs. Benito Alén, David Fuster y Yolanda González, por su apoyo y paciencia en estos últimos años.

Abbreviations

Ag	*Silver*
$AgNO_3$	*Silver Nitrate*
As	*Arsenic*
Au	*Gold*
BE	*Binding Energy*
BF	*Bright-Field*
CCD	*Charge Coupled Devise*
CCl_4	*Carbon Tetrachloride*
$CHCl_3$	*Chloroform*
CMA	*Cylindrical Mirror analyzer*
CNOs	*Carbon Nano-Onions*
DF	*Dark-Field*
EDX	*Energy Dispersive X-Ray*
EELS	*Electron Energy Loss Spectroscopy*
EOBF	*Electro-Optical Beam Deflector*
FCC	*Face-Centered Cubic*
FFT	*Fast Fourier Transformation*
FWHM	*Full With at Half Maximum*
Ga	*Gallium*
GaAs	*Gallium Arsenide*
Ge	*Germanium*
GPa	*Gigapascal*
$HAuCl_4$	*Gold(III) Chloride Trihydrate*
HF	*Hydrofluaric Acid*
HRTEM	*High Resolustion Electron Microscopy*
K	*Kelvin*
KHz	*Kilohertz*
LA	*Laser Ablation*
LEDs	*Light Emitting Diode*
LIP	*Laser Induced Pressure*
LIT	*Laser Iradiation Time*
LPP	*Laser Plasma Plume*
LSPR	*Localized Surface Plasmon Resonance*
NCs	*Nanocrystals*
Nd:YAG	*Neodymium-doped Yttrium Aluminium Garnet*
NPs	*Nanoparticles*
ns	*Nanosecond*
NWs	*Nanowires*
ºC	*Celsius*

OLC	*Onion-Like Carbon*
PIP	*Plasma Induced Plasma*
PL	*Photoluminescence*
PLA	*Pulsed Laser Ablation*
PLAL	*Pulsed Laser Ablation in Liquid*
PLD	*Pulsed Laser Deposition*
RF	*Radio Frecuency*
SAED	*Selected Area Electron Diffraction*
SERS	*Surface Enhanced Raman Spectroscopy*
Si	*Silicon*
SiC	*Silicon Carbide*
SiO_2	*Silicon Dioxide*
SW	*Shock Wave*
τ	*Decay Lifetime*
TEM	*Transmission Electron Microscopy*
TEOS	*Tetra-Ethyl-Ortho-Silicate*
TRPL	*Time Resolved Photoluminescence*
UV	*Ultraviolet*
UV-VIS	*Ultraviolet-Visible*
W	*Tungsten*
XPS	*X-Ray Photoelectron Spectroscopy*
XRD	*X-Ray Diffraction*

List of Figures

1. General Introduction

1.1. Introducción General

La aparición del láser de rubí en 1960 [1,2] abrió muchas puertas nuevas en el campo del procesado de materiales. La ablación con láser pulsado o, en inglés, "Pulsed Laser Ablation" (PLA), el proceso de evaporación o de arrancar material de un blanco haciendo incidir sobre éste un rayo láser pulsado intenso, fue una de las muchas aplicaciones que pronto encontraron los investigadores en la década de los 60. El uso de la radiación láser como una fuente externa de energía para evaporar materiales en vacío, que se deposita en forma de capas finas, fue reportado por primera vez por Smith y Turner en 1965 [3]. Sin embargo, investigaciones posteriores en esta área fueron esporádicas. No fue hasta la década de los 80 cuando se empezó a extender su uso, después de demostrarse con éxito el uso de la técnica PLA para obtener capas finas a base de materiales superconductores de alta temperatura crítica [4,5]. Durante los años siguientes la PLA se ha revelado como un poderoso instrumento para la fabricación de nanoestructuras en distintos medios: Alto vacío [6,7], atmósfera inerte [8,9] y líquidos [10,11].

Sin embargo, en comparación con las aplicaciones de PLA bajo condiciones de ultra-alto vacío o en presencia de un gas inerte, las aplicaciones en medio líquido (en adelante PLAL) están limitadas a los casos que implican una interacción entre el láser pulsado utilizado y el material que se ablaciona, por su gran potencial para la elaboración de nuevos materiales nanoestructurados, nanocompuestos y nanopartículas (NPs). Esto se puede explicar por la complejidad en comparación al caso de la interacción entre el pulso láser y un blanco sólido en vacío o en ambiente gaseoso [12]. En general el PLA ocurre en condiciones de equilibrio no termodinámico que obedece a condiciones extremas de fluencia de energía, cambios súbitos y muy significativos con la temperatura, tanto de los electrones como de los iones. La pluma de ablación se caracteriza por tener iones, electrones, agregados de átomos que se encuentran en un ambiente termodinámicamente inestable. En el caso de PLAL la pluma de plasma estaría confinada en el líquido, por lo que dicho estado termodinámico sin duda difiere del producido por PLA en gas o en ultra-alto vacío.

La ablación láser en medio líquido se ha perseguido intensamente en las últimas décadas debido a su simplicidad y a su enorme potencial en aplicaciones tecnológicas. Es de destacar su uso para provocar procesos de síntesis química a alta temperatura, que tendrían un gran impacto en las Ciencias biomédicas, gracias a los diversos efectos que

tienen lugar al interactuar el láser con los tejidos (foto-vaporización, foto-disrupción, fotocoagulación o foto-estimulación). Por este motivo, hoy día, el uso de láseres en el campo de la Urología nos ofrece un amplio abanico de posibilidades, que van desde la cirugía desobstructiva, fragmentación de cálculos renales o la resección y ablación de tejido prostático hasta la cirugía reconstructiva, como el caso de la soldadura de tejidos en la vasectomía o en la reparación de una estenosis uretral [13, 14,15].

Hasta la fecha no se habían realizado grandes esfuerzos de investigación dirigidos en la aplicación de la técnica PLAL para la elaboración de materiales avanzados. Por ejemplo, ya existían indicios en los años 90 referentes a la aplicación de la técnica PLAL en la ingeniería de materiales nanoestructurados, habiéndose demostrado como una técnica especialmente eficaz en el proceso de generación y fragmentación de material, dando lugar a NPs de geometría esférica. Concretamente, fue en 1993 cuando se demostró el uso de la técnica PLAL para obtener NPs irradiando un blanco de metal en varios líquidos [16, 17].

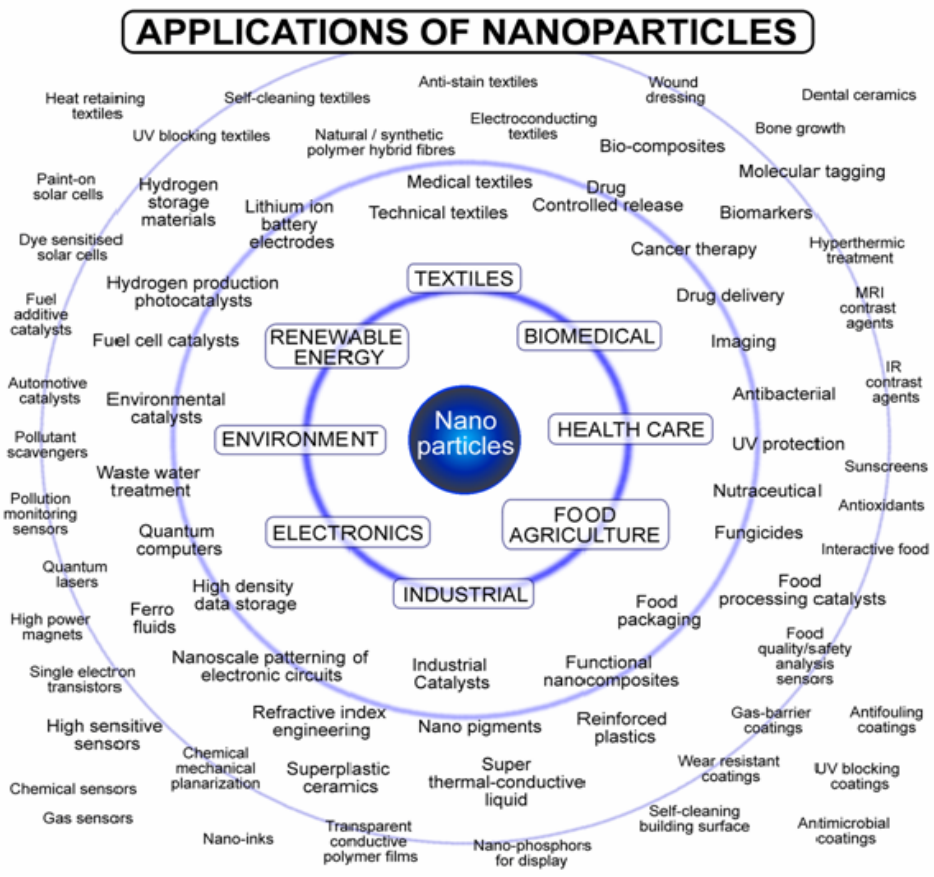

Figura 1.1: Producción a escala comercial de NPs inorgánicas publicado en 2010 por el "Centre for Material and Fibre Innovation", Deakin University (Australia) [18].

Las propiedades de las NPs (piezas de material con dimensiones nanométricas) se suelen diferenciar notablemente de su comportamiento como material masivo, dependiendo del tipo de material que las conformen, pero típicamente en el rango de unos pocos nm hasta unos 100 nm, típicamente. Desde la Ingeniería y la Física Aplicada se trabaja en forma interdisciplinaria hacia el estudio y desarrollo de nuevos materiales nanoestructurados con propiedades novedosas, que se puedan diseñar para aplicaciones específicas. La Figura 1.1 resume el uso de NPs inorgánicas en diversos campos de aplicación.

El método PLAL se ha desarrollado como un método simple (ver el esquema en la Figura 1.2), toda vez que potente y versátil para preparar NPs de metales, de semiconductores e incluso de polímeros. El desarrollo de nanomateriales mediante PLA en gas o en vacío exige condiciones de ultra-alto vacío en cámaras especiales y un gas inerte para evitar cualquier reacción entre las partículas y el medio ambiente circundante, que pueda modificar las propiedades ópticas y estructurales de los productos. Además, las partículas se obtienen en forma de películas, lo que limitaría su uso posterior. El método PLAL, por el hecho de realizarse en un medio líquido, permite obtener partículas en suspensión en dicho líquido, sin la necesidad de estar bajo ciertas condiciones de presión. Por otro lado, en los métodos químicos, la producción de NPs es más fácil, pero tiene aspectos negativos, como la contaminación de la superficie de los productos formados, lo que limita su potencial en muchas aplicaciones. El PLAL permite obtener NPs también de una manera rápida y con ausencia de disolventes tóxicos, esto es, un método intermedio a las vías puramente físicas y puramente químicas, en condiciones de satisfacer ciertas necesidades de materiales, como aquéllos que resulten difíciles de obtener, como el diamante.

Como técnica de fabricación, el método PLAL ha tenido ventajas con respecto al PLA en alto vacío o en presencia de un gas inerte, pues no sólo permite controlar algunos parámetros de fabricación, sino que también afecta considerablemente a la morfología y la estructura de las NPs formadas. Esto ha llamado la atención de varios grupos de investigación para usar este método en la generación y la modificación de NPs.

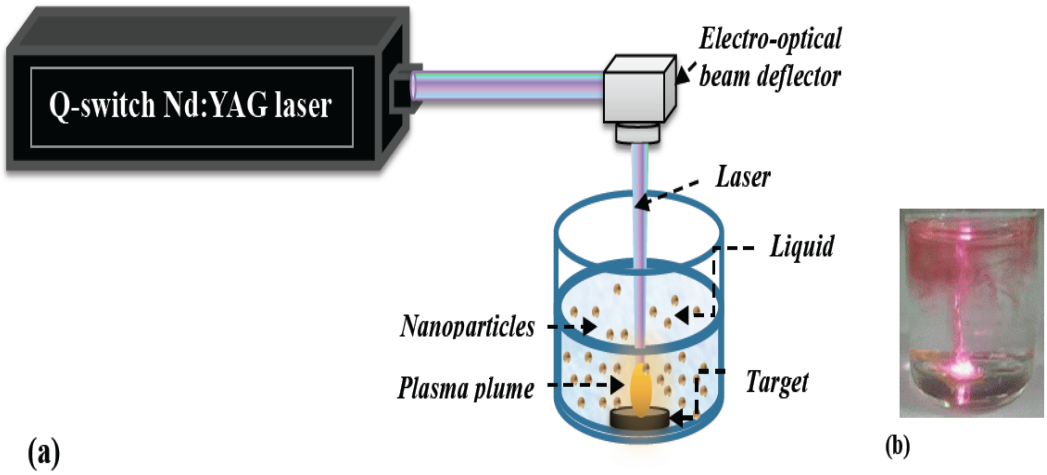

Figura 1.2: (a) Esquema simplificado del montaje experimental de PLAL. (b) Imagen real del recipiente usado para la fabricación de NPs oro a partir de un blanco de oro masivo.

Los primeros estudios de PLAL se centraron en los siguientes temas:

- Fabricación de NPs a base de irradiación de un blanco metálico sumergido en medio acuoso [19,20].
- La modificación del tamaño y la forma de NPs usando medios líquidos reactivos y NPs de 100-500 nm a como blancos para el PLAL [21,22].
- Usar las características únicas del PLAL para la fabricación de nanoestructuras con morfologías [23,24], estructuras y fases novedosas [25,26], que permiten explorar nuevas aplicaciones, como biodetectores o dispositivos de luminiscencia controlable [27,28].

Zengy et al. realizaron un estudio detallado sobre la formación de nanoestructuras a base de Zn, Fe y S utilizando para el PLAL un láser de Nd:YAG intenso (1064 nm, 10 ns de pulso a 10 Hz de frecuencia de repetición, 80 mJ de energía por pulso sobre un área del blanco de 2 mm^2) con una densidad de energía del orden de 4.10^8 $W.cm^{-2}$, con el que relacionaban el enfriamiento ultra rápido de la plasma y su interacción con el medio circundante con la formación de las nanoestructuras [29, 30,31]. En otros experimentos de PLAL con un láser Nd:YAG doblado (532nm, 10 ns de pulso a 10 Hz de frecuencia de repetición y una densidad de energía promedio del orden de 10^7 $W.cm^{-2}$, *Yang* propuso otro modelo de evaporación térmica en la que participan dos tipos de plasma, uno inducido por el láser desde el blanco sólido y otro inducido desde el medio líquido, de

forma que ambos pueden mezclarse y reaccionar entre sí [32]. El enfriamiento y la condensación del material eyectado pueden llevar a la formación de nuevas nanoestructuras con composición distinta a la del blanco [32, 33]. *Phuoc et al.* propusieron otro mecanismo de formación de nanogotas metálicas [34], según el cual la irradiación láser podría causar una fusión local del blanco. La capa de líquido adyacente al plasma se calienta dando lugar a un estado de vapor con una presión elevada [34, 35]. La expansión del vapor-plasma salpica la parte fundida en nanogotas, que después reaccionaría con el medio líquido produciendo las nanoestructuras [36]. Este mecanismo de expulsión explosiva de la plasma se propuso para explicar la producción de nanoestructuras de óxidos y sulfuros metálicos con diferentes morfologías [23].

En otros experimentos de PLAL se propone que esos mecanismos, la evaporación térmica (es decir, formación de la plasma pluma) y la expulsión explosiva de nanogotas pueden ocurrir simultáneamente. Esto es, sus efectos deben superponerse para producir nanoestructuras. *Nichols*, reportó que la evaporación térmica genera capas de NPs de Pt con un tamaño uniforme, mientras que la expulsión explosiva produce NPs grandes con una distribución de tamaño ancha y un rendimiento significativamente más alto [36, 37].

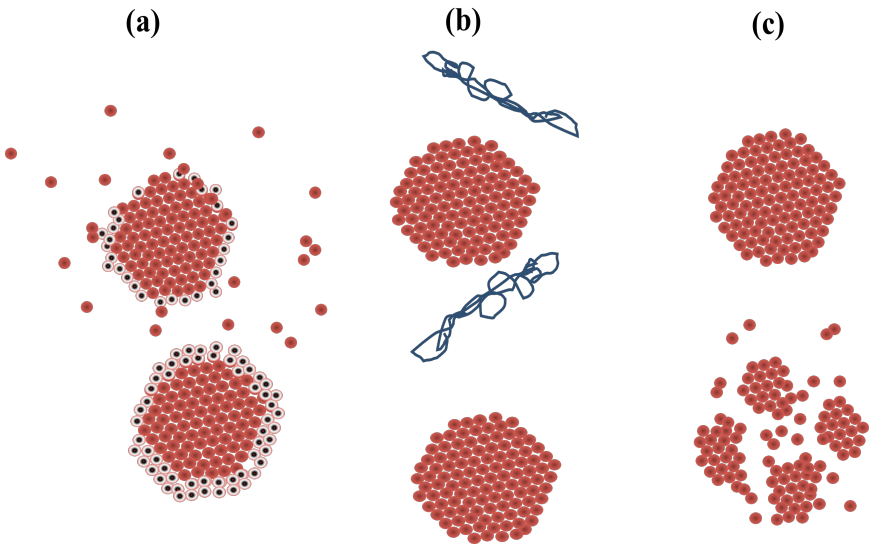

Figura 1.3: Ejemplos relevantes del PLAL usando una solución de NPs como blanco: (a) el nuevo material creado por PLAL reacciona con las NPs para dar un compuesto diferente, (b) interacciones físicas o químicas en la superficie de las NP pueden parar su crecimiento o producir nuevas nanostructuras, (c) la fragmentación de una sola partícula en varias más pequeñas.

Otros investigadores han preferido sustituir el blanco solido por soluciones coloidales de NPs o solventes con precursores de éstas (caso de una parte de la presente tesis). De esta forma, los solventes y las NPs (o micropartículas) serían el propio blanco expuesto a la irradiación láser (Figura 1.3), transformándose en partículas de tamaño más pequeño y con formas, fases y composiciones iguales o diferentes [38, 39]. Para obtener estos cambios se propusieron dos mecanismos:

- Mecanismo de fusión-evaporación: el láser induce fusión y/o vaporización de partículas de mayor tamaño en átomos o moléculas, y luego las especies atómicas o moleculares producidas se reorganizan en pequeñas nanoestructuras con las misma o distinta forma y estructura cristalina, dependiendo de las condiciones experimentales [40,41,42,43].
- Mecanismo de la explosión Coulombiana: implica la expulsión de los fotoelectrones o electrones térmicos, por efecto de la irradiación láser, de la superficie de las nanoestructuras (blanco), dejando cargas positivas en la parte interior de la superficie. Estas cargas superficiales inducidas derivan en una repulsión electrostática entre diferentes partes de las partículas primarias, que originaría la fragmentación de una sola partícula en varias más pequeñas [44, 39].

Resultados más recientes parecen apuntar que la importancia de un mecanismo frente al otro depende de las propiedades del láser. Así, la fragmentación sería el proceso dominante para la irradiación con láseres pulsados en femtosegundos, mientras que la evaporación térmica domina en el caso de irradiación con láseres de nanosegundos, incluso con excitación a longitudes de onda en ultravioleta[38, 45]. También se pueden obtener NPs con la irradiación directa con un láser pulsado de un líquido conteniendo un precursor de ellas (por ejemplo, $HAuCl_4$ para obtener NPs de oro), debido a la fotoreducción de éste [46,47,48]. Aplicando este concepto "físico-químico" se podrían formar nano-compuestos de tipo núcleo-corteza, por ejemplo un núcleo de material semiconductor (TiO_2, ZnO_2, …) recubierto de una corteza metálica (Au, Ag, …) [49, 50]. Finalmente, destacar que también se pueden obtener tales tipos de nanocompuestos núcleo-corteza directamente por ablación láser [51-54].

En esta tesis vamos a tratar fundamentalmente la aplicación del método PLAL usando tres tipos de aproximación i) blancos sólidos en agua, ii) blancos sólidos en

líquidos orgánicos y iii) blancos sólidos en líquidos con sales precursoras de NPs de Au y Ag (por separado y mezcladas). Los materiales se han elegido atendiendo a su importancia en la Tecnología actual: semiconductores como el GaAs y el Silicio y metales nobles como la plata y el oro. El objetivo principal es obtener NPs de estos materiales, dado que éstas, en forma de disolución coloidal, podrían usarse en nuevos tipos de aplicaciones en campos diversos como nanomedicina, sensores, electrónica/optoelectrónica, por ejemplo usándolas como tintas para depositarse sobre substratos diversos (Si, III-V, vidrios, plásticos, etc.). Más abajo se resumen algunos detalles sobre aplicaciones de estos materiales en forma de NPs.

Arseniuro de Galio (GaAs): Es uno de los semiconductores más importantes de la familia III-V, ampliamente usado en Electrónica (transistores de alta velocidad) y Optoelectrónica (LEDs, láseres, células solares, …)[55,56]. En las NPs de GaAs, si su tamaño es suficientemente pequeño (< 20 nm), podría observarse efecto de confinamiento cuántico (radio de Bohr de unos 15 nm) y, por tanto, aumentar su banda prohibida efectiva [57]. Al contrario de lo que sucede con soluciones coloidales de nanocristales II-VI (CdTe, CdSe y CdS), la preparación y caracterización de semiconductores compuestos III-V en forma nanocristalina y, en particular, de GaAs, no está tan documentada usando síntesis química con propiedades reproducibles (la alta temperatura necesaria para el proceso conduciría a oxidación de las NPs).

Silicio (Si): Las NPs de silicio tienen un gran potencial de aplicación como marcadores biológicos o agentes terapéuticos y en tecnología fotovoltaica, entre otras. Las NPs de Si también se pueden usar como precursores de materiales nanoestructurados de C-Si para fabricar electrodos de baterías de iones de litio [58]. Si bien se han usado diversas técnicas para obtener nanoclusters de Si, monocapas y películas finas de NPs de Si, como la implantación de iones [59] y la ablación láser en ultra alto vacío [60], hay todavía muy pocos ejemplos de soluciones coloidales con NPs de Si.

Metales nobles Au, Ag, Au-Ag: Las NPs de plata y oro exhiben unas excelentes propiedades físicas, químicas y biológicas, que son intrínsecas a su tamaño nanométrico. [61-62-63] Presentan un extraordinario potencial como agentes foto-terapéuticos en el tratamiento del cáncer, así como para la elaboración de nanoestructuras útiles para el transporte y la vectorización selectiva de fármacos y macromoléculas terapéuticas y en terapia génica (vehiculización de plásmidos, DNA, RNA…) [64,65]. También es de

destacar su utilidad en la elaboración de sistemas transportadores inteligentes que permiten controlar, en el espacio y en el tiempo, la liberación del compuesto terapéutico asociado activado por estímulos biológicos internos [66-67] o por activación de un estímulo externo (por ejemplo luz láser) [68-69]. Otra aplicación interesante de las NPs metálicas en el campo de la biología es la detección de concentraciones muy bajas de moléculas mediante el efecto denominado "Surface-Enhanced Raman Scattering" (SERS), descubierto a finales de la década de los 70. Este fenómeno está relacionado con un incremento gigantesco de la dispersión Raman (10^{10}-10^{15}) en el entorno de las NPs metálicas. Este fenómeno se relaciona con la Resonancia Superficial de Plasmón Localizado (LSPR, siglas de su denominación en inglés, "Localized Surface Plasmon Resonance") debida a la oscilación de los electrones del metal por inducción de un campo eléctromagnético externo, fenómeno que también es la base para la realización de sensores químicos y biosensores.

Fabricación de NPs de GaAs y GaAs-SiO_2

La fabricación de NPs de GaAs a través de métodos químicos es la más desarrollada hasta la fecha [70-71], obteniéndose NPs de GaAs con forma alargada, con una relación de aspecto del orden de 1.2-1.3 [70,72]. Las partículas tienden a ser ricas en galio en una proporción Ga/As de hasta 5/4 [70-72]. Varios estudios han encontrado la presencia de una capa de óxido amorfo en la superficie de las NPs de GaAs y otras especies moleculares [73-74], así como impurezas de cloro debido al uso de $GaCl_3$ como precursor de Ga.

La preparación de NPs de GaAs se puede realizar otros métodos, como epitaxia de haces moleculares [70-72-75], pulverización catódica RF [77] y ablación laser [78,79,80]. La técnica PLA bajo atmósfera de gas inerte ha confirmado que se producen NPs de GaAs de 5-8 nm estequiométricas [78], mientras en el caso de la ablación en vacío las NPs eran más pequeñas (1.5 nm) y rodeadas de una corteza amorfa con exceso de Ga o As [79]. En el caso de NPs de GaAs obtenidas por PLAL se observa una distribución de tamaños mucho más amplia, 5-20 nm, así como un exceso de Ga. Sin embargo, esta última técnica es la más simple y menos costosa, por lo que se ha elegido en esta tesis, además de considerar, a priori, que se pueden obtener NPs con una mayor pureza química y cristalinidad, partiendo de blancos adecuados.

En esta tesis se presentará la preparación de soluciones coloidales estables de nanocristales de GaAs de tamaños entre 9 y 13 nm (puntos cuánticos, porque su tamaño es lo suficientemente pequeño como para exhibir efecto de confinamiento cuántico) usando ablación laser de un blanco masivo de GaAs de alta pureza y monocristalino sumergido en agua, así como un estudio de sus propiedades ópticas más básicas y estructurales:

- Distribución de tamaños de las NPs de GaAs, a través de imágenes de microscopia electrónica de transmisión (TEM).
- Análisis de la calidad estructural y propiedades cristalinas de las NPs por TEM de alta resolución (HRTEM).
- Correlación entre las propiedades estructurales y morfológicas con las propiedades ópticas de las NPs.

Como una manera de mejorar la estabilidad de los coloides de NPs de GaAs y tener más posibilidades de ulteriores aplicaciones, se procedió a intentar lograr un encapsulado las NPs de GaAs con cortezas de SiO_2 mediante el método de Stöber [81] (hidrólisis de TEOS, $Si(OCH_2CH_3)_4$, a un temperatura de 0º y posterior tratamiento por ultrasonidos).

Este material es ampliamente conocido y adecuado para una funcionalización fácil con diferentes tipos de moléculas orgánicas, como tioles, aminas y carboxilos [82][83], lo que constituye un paso preliminar necesario para utilizar estas NPa en protocolos de conjugación biomolecular (aplicaciones para biomarcadores y biosensores).

- ***Fabricación de NPs de Silicio:***

Otro tema que hemos abordado en esa tesis es la fabricación de NPs de silicio (Si) por PLAL, dado que es una línea de investigación de gran interés y repercusión industrial, pero todavía en sus inicios. Los métodos de química clásica, que son muy útiles para preparar las soluciones coloidales de varios metales o semiconductores, no lo son en el caso del Si. Este es el obstáculo más importante para el uso extenso de las NPs de Si en la multitud de aplicaciones que conocemos para este material. Además, el uso de NPs de Si como biomarcadores en sistemas vivos impone requisitos estrictos, como la pureza química del producto, un requisito difícil de cumplir si se usa la síntesis química (alta

temperatura y agentes de reducción potentes) en el proceso de fabricación. En las técnicas químicas las NPs de Si sufren modificaciones superficiales al estar en contacto con distintos reactivos químicos, que determinan su recubrimiento y distribución de tamaños, lo que afecta a sus propiedades ópticas. El uso de PLAL con agua des-ionizada evitaría este problema y se considera en la literatura como un método de síntesis verde, libre de contaminación [84]. En esta tesis, en una primera etapa se trabajó en la producción de varias muestras por irradiación de un blanco de Si de alta pureza (comercial) en H_2O, para continuar luego con otros solvantes orgánicos (Etanol-Metanol, n-Propanol, Hexano, Cloroformo, …), usando láseres de varios longitudes de onda (1064, 532 y 355 nm). Para evitar las problemas de oxidación hemos usado líquidos orgánicos sin oxígeno en la fabricación de NPs de Si por PLAL, y así lograr mejores propiedades físico-químicas que en el caso de síntesis química. Las NPs de Si producidas por PLAL suelen ser bastante grandes (decenas a centena de nanómetros) y una distribución de tamaños ancha [85]. Para algunas aplicaciones puede ser suficiente, pero existen otras de gran interés en el caso de tamaños inferiores a los 5 nm, para los que existiría confinamiento cuántico, esto es, las NPs se comportarían como puntos cuánticos.

Las propiedades ópticas básicas de estas muestras se caracterizaron por espectroscopia ultravioleta-visible, fotoluminiscencia y Raman, mientras que se utilizó TEM para obtener información sobre la geometría y tamaño de las NPs. Con el objetivo de estudiar la formación de NPs de Si en líquidos orgánicos se evaluaron distintas condiciones del proceso PLAL y varios tratamientos químico-físicos posteriores. De los resultados que hemos logrado en el presente trabajo podemos destacar la posibilidad de fabricar NPs de Si por PLAL con pequeño tamaño. Por ejemplo, usando cloroformo ($CHCl_3$), compuesto orgánico que contiene átomos de carbono, hidrógeno y cloro, se sustituirían las interacciones Silicio-Hidrocarburos por las de Silicio-Halógenos predominarían. [86] Los resultados de la caracterización óptica y estructural (TEM, HRTEM) sobre NPs de Si preparadas con este líquido relevan que su tamaño está en el rango 20-200 nm y son poli-cristalinas. La aplicación de un post-tratamiento con ultrasonidos y en presencia de HF conduce a la desintegración de esas NPs grandes y a la formación de nanocristales individuales, tal y como se pone de manifiesto en imágenes TEM (distribución de tamaños) y HRTEM (estructura cristalina). Con espectroscopia Raman observamos un ensanchamiento asimétrico del pico y un corrimiento hacia alta energía, lo que se puede atribuir a efectos de confinamiento del fonón. Por otra parte, el

espectro de fotoluminiscencia consiste en una banda en el rango 450-900 nm, cuya cinética de recombinación sería característica de NPs de Si con confinamiento por reducción de tamaño.

- ***Nuevas Nanostrucuras Silicio-Carbono***

Durante la fabricación de NPs con PLAL, la interacción del medio líquido con las NPs recién sintetizadas a menudo se supone que es despreciable, por lo tanto, no destructiva con respecto al líquido. Sin embargo, para muchos líquidos orgánicos (hidrocarburos) esta hipótesis resulta ser incorrecta, incluso cuando se utilizan láseres de energías moderadas. *Amendola et al.* fueron los primeros que realizaron PLAL sobre un blanco de oro en tolueno usando un laser Nd:YAG (9 ns de pulso, 1064 nm), demostrando que se forman NPs de Au recubiertas con multicapas de grafito [87], argumentando que estas multicapas podían ser un producto de la destrucción de tolueno. Recientemente se demostró que se forman también NPs de SiC, además de las de Si, en experimentos de PLAL sobre un blanco de Si en Etanol usando láseres de ns (10 ns, 1064 nm) y de fs (35-1000 fs, 1064 nm) [88]. En otros trabajos se presentan evidencias de la formación de grandes esferas huecas de carbono (fullerenos) bajo tiempos largos del proceso PLAL sobre un blanco de Silicio en tolueno usando un laser de ns (10 ns, 1064 nm)[89]. En esta misma línea también se ha realizado recientemente un estudio detallado para investigar la dependencia y la eficacia de la formación de una corteza alrededor de las NPs de Si con PLAL sobre Si con un láser de ns (5 ns, 1064 nm,) con diferenes líquidos: H_2O, Etanol, 2-Propanol, Hexano, Octano, Tryoctina-amina, Tolueno, encontrando que este último es el medio más eficiente para la producción de cortezas grafito [90]. Por tanto, el mecanismo de formación de las estructuras de carbono aludidas (corteza en forma de multicapas de grafito, SiC, nanoestructuras de fullereno, …) requieren estudios más detallados.

En esta tesis demostramos que el PLAL con un láser de ns (40 ns, 355 nm) sobre un blanco de Si en cloroformo durante un tiempo largo de proceso (entre 60 y 90 min) conduce a la formación de:

- Nanocomposites multi-cristalinos formados por nanocristales de Si y SiC con tamaños del orden de 5 -10 nm.

- Multicapas de grafito rodeando los nanocomposites Si-SiC.
- Multicapas de carbono o formando nanoestructuras especiales dispersas en el coloide ("*carbon nano-onions"*).

Basándonos en una comparación de la eficiencia de formación de nanoestructuras de carbono usando $CHCl_3$ y CCl_4 mediante PLAL, más un tratamiento posterior con ultrasonidos reportado en nuestro trabajo previo (ver sección siguiente), se sugiere que la descomposición del disolvente da lugar a radicales CH- muy reactivos es el mecanismo responsable de la formación de la corteza de grafito sobre las NPs de Si. En el trabajo anterior no se llegan a formar nanostructuras de carbono porque el tiempo del proceso PLAL es muy corto (algunos segundos), en comparación al proceso que describimos en esta parte [II]. Esto es, un tiempo corto de irradiación impediría la ablación secundaria de las NPs de Si que se están produciendo en el proceso PLAL. Por el contrario, en esta parte de la tesis estamos utilizando un tiempo largo de ablación (60-90 min), lo que nos permite alcanzar altas concentraciones de NPs de Si en suspensión, por lo que podemos suponer que una parte de la radiación láser incidente se estaría absorbiendo por las propias NPs y no exclusivamente por el blanco. Como resultado, es muy probable que se puedan producir reacciones químicas (a alta temperatura) del líquido en la superficie de las NPs de Si.

- ***Nanopartículas metálicas a base de ablación de un blanco de silicio***.

En esta parte de la tesis presentamos un nuevo método de síntesis química de NPs metálicas que está activada, y es altamente eficiente, por la irradiación de un blanco sólido adecuado sumergido en una disolución acuosa de las sales metálicas precursoras correspondientes. Este método se presentó en 2007 como patente y se publicaron los resultados preliminares en 2008 (ver sección siguiente). Con posterioridad se hizo un trabajo más detallado estudiando la formación de NPs Ag-Au partiendo de diferentes proporciones de las sales precursoras de ambos metales en la disolución acuosa en la que se sumerge el blanco sólido. El mecanismo de formación de las NPs metálicas usando nuestro método se basa en las reacciones químicas de reducción de los iones metálicos, provocadas por la ablación del blanco sólido, a diferencia de no usar blanco como en experimentos anteriores [46,47,48]. La reducción de los iones metálicos origina centros de

nucleación sobre los que crecerán las NPs metálicas. Además, las partículas producidas directamente por ablación del blanco sólido se oxidan y recubren las partículas metálicas dándoles un carácter inerte, además de obtener un un coloide estable (después de filtrar tales partículas típicamente grandes de la disolución). Esta hipótesis se probó comparando el uso de Si (la oxidación del material en forma micro/nanocristalina es más eficiente que en el caso masivo) con otros blancos, como Ge y W.

De todos los resultados que hemos obtenido en el desarrollo de este trabajo podemos resumir que el uso del PLAL tienes algunas ventajas frente al PLA tradicional u otros métodos:

- PLAL es una aproximación única y versátil para la síntesis de una gran variedad de nanomateriales con la adecuada selección de blancos y disoluciones líquidas.
- PLAL es un proceso "limpio", compatible con algunos de los principios de la "química verde"', pues requiere menos agentes químicos que los procesos de síntesis usuales y la producción de residuos es mucho menor.
- PLAL es un método rápido y de muy bajo coste, por la extremada sencillez del montaje experimental (basta un sistema láser como los usados en grabación/estampación).
- Algunos de los precursores químicos de las NPs se pueden sustituir por el material masivo que se usa como blanco en el PLAL.
- En varios casos, las NPs inorgánicas recubiertas con moléculas orgánicas se pueden obtener en una sola etapa, in situ (por ejemplo, durante la ablación) o ex situ (por ejemplo, después de la ablación).

1.2. Publicaciones asociadas a esta tesis doctoral

Listado de publicaciones (compendiadas)

I. K. Abderrafi, E. Jiménez, T. Ben, S.I. Molina, R. Ibáñez, V. Chirvony, and J.P. Martínez-Pastor, ***Production of nanometer-size GaAs nanocristals by nanosecond laser ablation in liquids***, J. Nanosci. Nanotechnol. **12**, 6774-6778 (2012).

II. K. Abderrafi, R. García Calzada, M.B. Gongalsky, I. Suárez, V. Chirvony, R. Abargues, V.Yu. Timoshenko, R. Ibáñez, and J. Martínez-Pastor, ***Silicon quantum dots produced by nanosecond laser-ablation in an organic liquid*****,** J. Phys. Chem C **115**, 5147–5151 (2011)

III. K. Abderrafi, R. García-Calzada, J.F. Sánchez-Royo, V. Chirvony, S. Agouram, R. Abargues, R. Ibáñez, and J.P. Martínez-Pastor, ***Laser ablation of a silicon target in chloroform: formation of multilayer graphite nanostructures***, J. Phys. D: Appl. Phys. **46**, 135301 (9 pp) (2013).

IV. E. Jiménez, K. Abderrafi, J. Martínez-Pastor, R. Abargues, J.L. Valdés, and R. Ibáñez, ***A novel method of nanocrystal fabrication based on laser ablation in liquid environment***, Superlattices & Microstructures **43**, 487-493 (2008). Sobre la base de este trabajo también se presentó una patente (P200702415, PCT/ES2008/070156, publicación WO 2009/030799 Al).

V. E. Jiménez, K. Abderrafi, R. Abargues, J.L. Valdés, and J.P. Martínez-Pastor, ***Laser-ablation induced synthesis of metal-oxide beads in a single step***, Langmuir **26**, 7458-7463 (2010).

Listado de publicaciones (NPs metálicas y aplicaciones de éstas)

VI. R. Abargues, K. Abderrafi, E. Pedrueza, R. Gradess, J. Marqués-Hueso, E. Jimenez, J.L. Valdés, and J.P. Martinez-Pastor, ***Optical properties of different polymer thin films containing in situ synthesized Ag and Au nanoparticles***, New Journal of Chemistry **33**, 1720-1725 (2009).

VII. R. Abargues, R. Gradess, J. Canet-Ferrer, K. Abderrafi, J.L. Valdés, E. Jiménez, and J.P. Martinez-Pastor, ***Scalable heterogeneous synthesis of metallic nanoparticles and aggregates with polyvinyl alcohol***, New Journal of Chemistry **33**, 913-917 (2009).

VIII. R. Abargues, S. Albert, J.L. Valdés, K. Abderrafi, and J. Martinez-Pastor, ***Molecular-mediated assembly of silver nanoparticles into controlled interparticle spacing and chain length***, J. Materials Chemistry **22**, 22204-22211 (2012).

IX. G. Fuertes, E. Pedrueza, K. Abderrafi, R. Abargues, O. Sánchez, J. Martínez-Pastor, J. Salgado and E. Jiménez, ***Photoswitchable bactericidal effects from novel silica-coated silver nanoparticles***, Proc. SPIE 8092, 80921M (2011); http://dx.doi.org/10.1117/12.889675;

X. G. Fuertes, O. L. Sánchez-Muñoz, E. Pedrueza, K. Abderrafi, J. Salgado and E. Jiménez, ***Switchable Bactericidal Effects from Novel Silica-Coated Silver Nanoparticles Mediated by Light Irradiation***, Langmuir, **2011**, *27* (6), pp 2826–2833.

XI. R. García Calzada, K. Abderrafi, I. Suárez, R. Abargues, J.F. Sánchez-Royo, A. Segura, R. Ibáñez, V. Chirvony, J. Martínez-Pastor, ***Simple laser-ablation based method to produce suspensions of luminescent silicon quantum dots for photovoltaic applications***, Proceedings of the 25th European Photovoltaic Solar Energy Conference (ISBN: 3-936338-26-4), DOI: 10.4229/25thEUPVSEC2010-1DV.3.67, p. 707-709.

Más arriba se ha justificado el tema de trabajo de esta tesis, ubicado en el campo científico correspondiente (literatura), y referido el tipo de resultados que se ha obtenido

(los cuales se resumirán ampliamente en el siguiente capítulo). Las publicaciones centrales de esta tesis doctoral se han listado arriba como I (NPs de GaAs), II (NPs de Si) y IV-V (NPs metálicas), en las que el autor de esta tesis ha realizado la mayor parte del trabajo de fabricación (PLAL), caracterización estructural (TEM, HRTEM) y óptica (espectroscopia UV-VIS y fotoluminiscencia), formando parte exclusiva de esta tesis doctoral. En el caso de la publicación III, que en parte surge del trabajo preliminar recogido en la publicación II, el trabajo de fabricación y caracterización estructural se ha realizado en colaboración con otro doctorando del grupo, D. Raúl García, siendo así punto de partida de un trabajo ulterior y más detallado en la misma línea de investigación.

También es de destacar la labor realizada por el autor de esta tesis doctoral en caracterización estructural y óptica de NPs metálicas obtenidas por métodos de síntesis química (Refs. VI-VII-VIII), y su aplicación como sensor químico, en colaboración con otros miembros del grupo. Estos trabajos no forman parte de ninguna tesis doctoral del grupo, pero no se incluyen en el resumen de resultados de esta tesis (capítulo siguiente), por consistencia con la temática principal de la tesis (fabricación de NPs por PLAL). Tampoco se incluyen en el anexo de publicaciones compendiadas (capítulo 4), para no incrementar innecesariamente el tamaño de esta tesis.

Las NPs metálicas obtenidas por PLAL (Refs. IV-V) se usaron también para estudiar su efecto bactericida (Ref. IX) en colaboración con un grupo de Biología del ICMOL, publicación relativa a la aplicación de estas nanopartículas, aunque tampoco se ha compendiado en la presente memoria. Finalmente, la publicación X tiene que ver con la presentación de los resultados obtenidos sobre producción de NPs de Si por PLAL (Ref. II) en la 25ª Conferencia Europea de Fotovoltaica 2010, por ser uno de los campos de aplicación más directos para éstas.

1.3. References to Chapter 1

1. T. H. Maiman, *Nature* **187**, 493 (1960).

2. "*Laser inventor Maiman dies; tribute to be held on anniversary of first laser*", *Laser Focus World*. ***2007***-05-09.

3. H. M. Smith and A. F. Turner, *Appl. Opt.* **4**, 147 (1965).

4. D. Dijkkamp, T. Venkatesan, X. D. Wu, S. A. Shaheen, N. Jisrawi, Y. H. Min-Lee, W. L. McLean and M. Croft, *Appl. Phys. Lett.* **51**, 619 (1987).

5. X. D. Wu, D. Dijkkamp, S. B. Ogale, A. Inam, E. W. Chase, P. F. Miceli, C. C. Chang, J. M. Tarascon and T. Venkatesan, *Appl. Phys. Lett* **51**, 861 (1987).

6. A. Okano and K. Takayanagi, *Appl. Surf. Sci* **127**,362 (1998).

7. J. M. Ballesteros, J. Solis, R. Serna and C. N. Alfonso, *Appl. Phys. Lett.* **74**, 2791 (1999).

8. J. R. Heath, Y. Liu, S. C. O'Brien, Q. Zhang, R. F. Curl, F. K. Tittel and R. E. Smalley, *J. Chem. Phys*. **83**, 5520 (1985).

9. D. P. Yu, X. S. Sun, C. S. Lee, I. Bello, S. T. Lee, H. D. Gu, K. M. Leung, G. W. Zhou, Z. F. Dong and Z. Zhang, *Appl. Phys. Lett.* **72**, 1966 (1998).

10. G. Yang, "*Laser Ablation in Liquids: Principles and Applications in the Preparation of Nanomaterials",* Stanford publications (2012).

11. A. Fojtik, M. Giersig and A. Henglein, *Ber Bunsen. Phys. Chem.* **97**, 1493 (1993).

12. H. Zeng, X.W. Du, S. C. Singh, S. A. Kulinich, S. Yang, J. He, and W. Cai *Adv. Funct. Mater.* **22**, 1333 (2012).

13. K. Nouri, "*Lasers in Dermatology and Medicine- Book*", DOI 10.1007/978-0-85729-281-0.

14. J. H. Amón Sesmero. "*Monográfico: ENDOUROLOGÍA Y LÁSER*", Arch. Esp. Urol. 61, 1.163 (2008).

15. L. STARK and P. CAR, *J. Urol.* **165**, 362 (2001).

16. A. Fojtik and A. Henglein, *B. Bunsen. Phys. Chem.* **97**, 252 (1993).

17. J. Neddersen, G. Chumanov and T. M. Cotton, *Appl. Spectrosc.* **47**, 1959(1993).

18. T. Tsuzuki, *Int. J. of Nanotechnology* **6**, 567 (2009).

19. A. Pyatenko, K. Shimokawa, M. Yamaguchi, O. Nishimura and M. Suzuki, *Appl. Phys.* A **79**, 803 (2004)

20. J. P. Sylvestre, A. V. Kabashin, E. Sacher, M. Meunier and J. H. Luong, *J. Am. Chem. Soc.* **126**, 7176 (2004).

21. F. Mafune, J. Y. Kohno, Y. Takeda and T. Kondow, *J. Phys. Chem. B* **105**, 9050 (2001).

22. J. Bosbach, D. Martin, F. Stietz, T. Wenzel and F. Trager, *Appl. Phys.Lett.* **74**, 2605 (1999).

23. K. Y. Niu, J. Yang, S. A. Kulinich, J. Sun, H. Li and X. W. Du, *J. Am. Chem. Soc.* **132**, 9814 (2010)**.**

24. K. Y. Niu, J. Yang, S. A. Kulinich, J. Sun and X. W. Du, *Langmuir* **26**, 16652 (2010).

25. Q. A. Drmosh, M. A. Gondal, Z. H. Yamani and T. A. Saleh, *Appl. Surf. Sci*. **256**, 4661 (2010).

26. P. Liu, Y. L. Cao, X. Y. Chen and G. W. Yang, *Cryst. Growth. Des.* **9**, 1390 (2009).

27. S. H. Stelzig, C. Menneking, M. S. Hoffmann, K. Eisele, S. Barcikowski, M. Klapper and K. Muller, *Eur. Polym. J.* **47**, 662 (2011).

28. H. B. Zeng, S. Yang, X. Xu and W. Cai, *Appl. Phys. Lett.* **95**, 191904 (2009).

29. H. B. Zeng, W. Cai, Y. Li, J. Hu and P. Liu, *J. Phys. Chem. B* **109**,18260 (2005).

30. P. S. Liu, W. P. Cai and H. B. Zeng, *J. Phys. Chem. C* **112**, 3261 (2008).

31. H. B. Zeng, X. Xu, Y. Bando, U. K. Gautam, T. Zhai, X. Fang B. Liu and D. Golberg, *Adv. Funct. Mater.* **19**, 3165 (2009).

32. G. W. Yang, *Prog. Mater. Sci.* **52**, 51 (2007)

33. Q. X. Liu, C. X. Wang and G. W. Yang, *Eur. Phys. B* **41**, 479 (2004).

34. T. X. Phuoc, B. H. Howard, D. V. Martello, Y. Soong and M. K. Chu, *Opt. Lasers Eng.* **46**, 829 (2008)

35. P. V. Kazakevich, A. V. Simakin, V. V. Voronov and G. A. Shafeev, *Appl. Surf. Sci.* **252**, 4373 (2006).

36. W. T. Nichols, T. Sasaki and N. Koshizaki, *J. Appl. Phys.* **100**, 114911 (2006).

37. W. T. Nichols, T. Sasaki and N. Koshizaki, *J. Appl. Phys.* **100**, 114913 (2006).

38. D. Werner and S. Hashimoto, *J. Phys. Chem. C* **115**, 5063 (2011).

39. H. Muto, K. Miyajima and F. Mafune, *J. Phys. Chem. C* **112**, 5810 (2008).

40. F. Mafune, J. Y. Kohno, Y. Takeda and T. Kondow, *J. Phys. Chem. B* **31**, 7577 (2002).

41. Y. Takeuchi, T. Ida and K. Kimura, *J. Phys. Chem. B* **101**, 1322 (1997).

42. S. C. Singh, S. K. Mishra, R. K. Srivastava and R. Gopal, *J. Phys. Chem. C* 114, 17374 (2010).

43. F. Mafune, J. Kohno, Y. Takeda and T. Kondow, *J. Phys. Chem. B* **107**, 12589 **(**2003).

44. a) P. V. Kamat, M. Flumiani and G. V. Hartl *J. Phys. Chem. B* **102**, 3123 (1998). b) H. Fujiwara, S. Yanagida and P. V. Kamat, *J. Phys. Chem B*. **103**, 2589 (1999).

45. A. Pyatenko, M. Yamaguchi and M. Suzuki, *J. Phys. Chem. C* **113**, 9078 (2009).

46. J. Zhang, J. Worley, S. Denommee, C. Kingston, Z. J. Jakubek, Y. Deslandes, M. Post and B. Simard, *J. Phys. Chem. B*. **107**, 6920 (2003)

47. K. Kurihara, J. Kizling, P. Stenius and J. H. Fendler, *J. Am. Chem. Soc.* **105**, 2574 (1983).

48. M. Sakamoto, T. Tachikawa, M. Fujitsuka and T. Majima, *Langmuir* **22**, 6361 (2006).

49. S. J. Tauster, S. C. Fung and R. L. Garten, *J. Am. Chem. Soc*. **100**, 170 (1978).

50. A. Wood, M. Giersig and P. Mulvaney, *J. Phys. Chem. B* **105**, 8810 (2001).

51. V. Amendola and M. Meneghetti, *Phys. Chem. Chem. Phys*. **11**, 3805 (2009).

52. C. L. Sajti, R. Sattari, B. N. Chichkov and S. Barcikowski, *J. Phys. Chem. C.* **114**. 2422 (2010).

53. V. Amendola, P. Riello, S. Polizzi, S. Fiameni, C. Innocenti, C. Sangregorio and M. Meneghetti, *J. Mater. Chem*. **21**, 18665 (2010).

54. Z. Yan, G. Compagnini and D. B. Chrisey, *J. Phys. Chem. C*.**115**, 5058 (2011).

55. A. Bar-Lev, "*Semiconductors and Electronic Devices, 2nd ed.*", Prentice Hall, New York (1984).

56. A. Luque, A. Marti and A. J. Nozik*, MRS bulletin.* **32**, 236 (2007).

57. Y. Fu, M. Willander and E. L. Ivchenko, *Superlattices & Microstructures* **27**, 255 (2000).

58. J. Rong, X. Fang, M. Ge, H. Chen, J. Xu and C. Zhou, *Nano Research March* **6**, 182 (2013).

59. L. Nikolova, R.G. Saint-Jacques, C. Dahmoune and G.G. Ross, *Surface Coatings Technology* **203**, 2501 (2009).

60. B.R. Tul, J.E. Carey, M.A. Sheehy, C. Frien and E. Mazur, *Appl. Phys. A* **83**, 341 (2006).

61. M. A. Garcia, *J. Phys. D: Appl. Phys.* **44**, 283001 (2011).

62. J. H. Hodak, A Henglein, and G. V. Hartland*, J. Phys. Chem. B*. **104**, 9954 (2000).

63. *(a)* P. L. Freund and M. Spiro, J. Phys. Chem. **89**, 1074 (1985).*(b)* C. A. Mirkin, R. L. Letsinger, R. C. Mucic and J. J. Storhoff, *Nature.* **382**, 607 (1996) *(c)* K. Sokolov, J. Aaron, B. Hsu, D. Nida, A. Gillanwater, M. Follen, C. Macaulay, K. Adler-Storthz, B. Korgel, M. Discour, R. Pasqualini, W. Arap, W. Lam and R. Richartz-Kortum, *Technol. Cancer Res. Treat.* **2**, 491 (2003) *(d)* Y. Sun and Y. Xia, Science. **298**, 2176 (2002) *(e)* K. L. Kelly, E. Coronado, L. L. Zhao and G. C. Schatz, *J. Phys. Chem. B*. **107**, 668 (2003).

64. R. Bhattacharya and P. Mukherjee, *Advanced Drug Delivey Reviews* **60**, 1289 (2008).

65. P.K. Jain, X. Huang, I.H. El-Sayed and M.A. El-Sayed, *Accounts of Chemical Research.* **41**, 1578 (2008).

66. S. Gunnarsdottir, M. Rucki and A.A. Elfarr, *J. Pharm. Exp*. **301**, 77 (2002).

67. R. Hong, G. Han, J.M. Fernández, B.J. Kim, N.S. Forbes and V.M. Rotello, *J. Am. Chem. Soc.* **128**, 1078 (2006).

68. G. Han, C.T. Martín and V.M. Rotello, *Chem. Biol. Drug*. **67**, 78 (2006).

69. G. Han, C.C. You, B.J. Kim, R.S. Turingan, N.S. Forbes, C.T. Martin and V.M. Rotello, *Angew Chem Int*. **45**, 3165 (2006).

70. M. A. Olshavsky, A. N. Goldstein and A. P. Alivisatos, *J. Am. Chem. Soc.* **112**, 9438 (1990).

71. M. A. Malik, P. O'Brien, S. Norager and J. Smith, *J. Mater. Chem*. **13**, 2591 (2003).

72. S. S. Kher, R. L. Wells, *Chem. Mater.* **6**, 2056 (1994).

73. P. C. Sercel, W. A. Saunders, H. A. Atwater and R. C. Flagan, *Appl. Phys. Lett.* **61**, 696 (1992).

74. H. Uchida, C. J. Curtis, P. V. Kamat, K. M. Jones and A. J. Nozik, *J. Phys. Chem.* **96**, 1156 (1992).

75. O. V. Salata, P. J. Dobson, P. J. Hull and J. L. Hutchison, *Appl. Phys. Lett.* **65**, 189 (1994).

76. C. J. Sandorff, J. P. Harbicon, R. Ramesh, M. J. Andrejco, M. S. Hedge, D. M. Hwang, C. C. Chang and E. M. Vogel, *Science* **245**, 391 (1989).

77. M. Hirasawa, H. Shirakawa, H. Hamamura, Y. Egashira and H. Komiyama, *J. Appl. Phys*. **82**, 1404 (1997).

78. J. Perriere, E. Millon, M. Chamarro, M. Morcrette and C. Andreazza, *Appl. Phys. Lett*. **78**, 2949 (2001).

79. T. W. Trelenberg, L. N. Dinh, C. K. Saw, B. C. Stuart and M. Balooch, *Appl. Surf. Sci.* **221**, 364 (2004).

80. R. A. Ganeev, M. Baba, A. I. Ryasnyansky, M. Suzuki and H. Kuroda, *Appl. Phys. B* **80**, 595 (2009).

81. W. Stöber, A. Fink and E. Bohn *J. Coll. Inter. Sci*. **26**, 62 (1968).

82. S. T. Selvan, C. Li , M. Ando, N. Murase**,** *Chem. Lett***. 33**, 4 (2004).

83. M. T. Harris, R. R. Brunson, C. H. Byers, *J. Non-Cryst. Solids* **121**, 397 (1990).

84. A. V. Kabashin and M. J. Meunier, *Appl. Phys.* **94**, 7941 (2003).

85.(a) S. I. Dolgaev, A. V. Simakin, V. V. Voronov, G. A. Shafeev and F. Bozon-Verduraz, *Appl. Surf.Sci.* **186**, 546 (2002) (b) P. V. Kazakevich, A. V. Simakin and V. V. Voronov and G. A. Shafeev, *Appl. Surf. Sci* **252**, 4373 (2006) (c) V. Svrcek, T. Sasaki, Y. Shimizu and N. Koshizaki, *Appl. Phys. Lett.* **89** 213113(2006) (d) X.W. Du, W. J. Qin, Y. W. Lu, X. Han, Y.S. Fu and S.L. Hu, *J. Appl. Phys.***102**, 013518 (2007) (e) I. Umezu, H. Minami, H. Senoo and A. Sugimura, *J. Phys. Conf. Ser*. **59**, 392 (2007). (f) V. Svrcek, T. Sasaki, Y. Shimizu and N. J. Koshizaki,. *Laser Micro/Nanoeng.* **2**, 15 (2007) (g) N. Takada , T. Sasaki and K. Sasaki, *Appl. Phys. A: Mater. Sci. Process* **93**, 833 (2008). (h) S. Yang , W. Cai , H. Zeng and Z. Li , *J. Appl. Phys*. **104**, 023516 (2008**)** (i) V. Svrcek, T. Sasaki, R. Katoh, Y. Shimizu and N. Koshizaki, *Appl. Phys. B: Laser Opt*. **94**, 133 (2009).

86. X. H. Sun, C. P. Li, N.B. Wong, C.S. Lee, S.T. Lee and B. K. Teo, *J. Am. Chem. Soc.* **124**, 14856 (2002).

87. V. Amendola, G. A. Rizzi, S. Polizzi and M. Meneghetti *J. Phys. Chem. B* **109**, 23125 (2005).

88. S. Yang, W. Cai, H. Zeng and X. Xu and *J. Mater. Chem.* **19**, 7119 (2009).

89. S. Yang, H. Zeng, H . Zhao, H. Zhanga and W. Cai, *J. Mater. Chem.* **21**, 4432 (2011).

90. C. C. Huang, K. Y. Chuang, C. J. Huang, T. M. Liu and C .S. Yeh, *J. Phys. Chem. C* 115. 9952 (2011).

2. Summary of Results

In this chapter we present a summary of the results obtained in the work. A previous section will be devoted to the experimental techniques used in this thesis to produce and characterize the different nanoparticles (section II.1). In the other sections a summary of results is presented: formation and characterization of GaAs and GaAs@SiO_2 nanoparticles (section II.2), production and characterization of silicon nanoparticles by PLAL of a Si target in an organic liquid (section II.3 and II.4) and the production of metal nanoparticles by PLAL using a Si target in water and precursors of the metal nanoparticles in solution (section II.5).

2.1. Experimental techniques

2.1.1. Pulsed Laser Ablation in Liquids (PLAL)

The ejection of macroscopic amounts of material from solids following irradiation with a short, intense laser pulse above a well-defined threshold fluence (*energy per unit area*) is a process known as Pulsed Laser Ablation (PLA).[1] Despite its apparent violent nature, this efficient material removal method has provided the basis for a wide spectrum of highly successful applications, ranging from nanoparticle synthesis, analytical chemistry [2-3] microelectronics [4-5], medicine [6], to restoration of painted artwork [7] etc. The origin and evolution of this superheated and super-pressurized material as the initial energy redistributes can lead to non-equilibrium processes as well as the formation of new materials. [8-9]

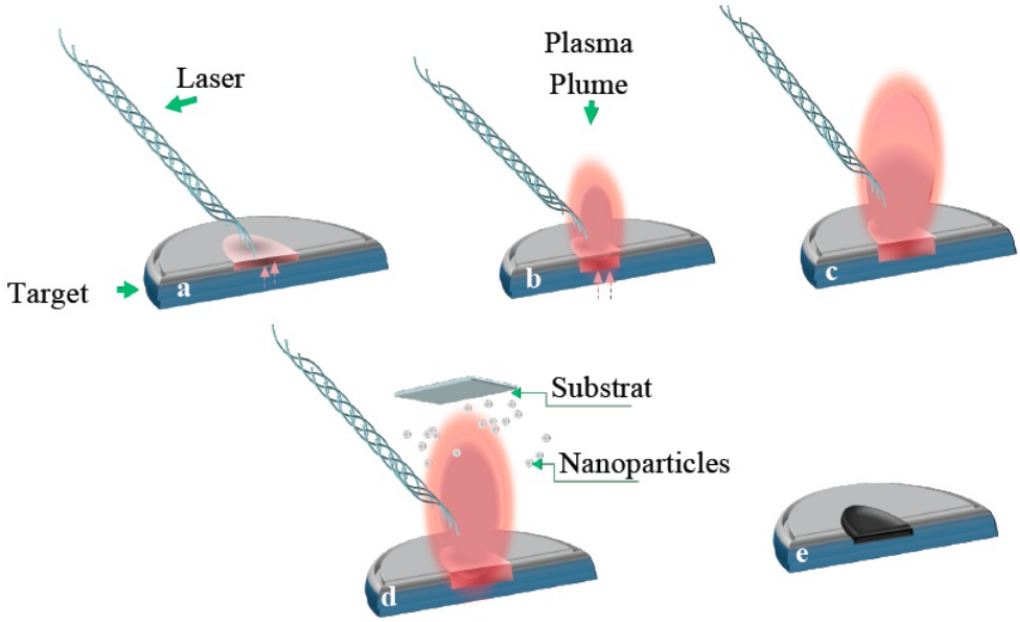

Figure 2.1: Scheme illustrating key elements of the PLA event:
(a) Initial absorption of laser radiation, melting and vaporization (shaded area corresponds to melted material and short arrows indicate motion of the solid–liquid interface).
(b) Melt front propagates into the solid, the vaporization continues and laser-plume interactions start to become important.
(c) Absorption of incident laser radiation by the plume, and plasma formation.
(d) Two different condensations of the laser-induced plasma: one is used to deposit thin films on substrates, and another one is used to synthesize nanoparticles.
(e) Melt front leading to eventual resolidification.

This is a very complex phenomenum when it is investigated more deeply, however, the hidden complexity soon becomes apparent. Much of this complexity is illustrated, schematically, in Figure 2.1.

Intense studies had been carried out in the field of interaction between laser pulses and solid targets. Therefore, the systemic and general information involved in these phenomena is available.[10-11] The initial laser beam-target interaction can create excited electrons in the solid, leading to the ejection of electrons by photoelectric or thermionic emission [12-13], and eventually forming a plasma above the sample surface.

We start by considering some of the mechanisms that can contribute to material loss following irradiation of the target with a pulse of photons. Following *Kelly and Miotello*, [14] these are generally sub-divided into primary and secondary processes. Suggested sub-divisions of the former include thermal, electronic and macroscopic sputtering; their relative importance will depend on the nature of the target material, and on the laser excitation wavelength and pulse duration. The materials ejection begins on a picosecond timescale. Thus, unless one is working with very short duration laser pulses, the ensuing plume of ejected material will be irradiated by the later part of the incident laser pulse. This radiation will, in many cases, be absorbed by the plume, leading to an attenuation of the light intensity incident on the target and excitation and ionization of species in the plume. Plasma formation and subsequent optical emission will result.

2.1.2. Pulsed Laser Ablation in Liquids (PLAL) of a solid target

The basic difference between the laser ablation of solids in vacuum or “diluted gas” and in liquids is caused by the movement of the laser plasma plume (LPP), which is confined by the liquids environment. Therefore, all processes including generation, transformation, and condensation of the plasma plume resulting from laser ablation of solids in liquid takes place under the condition of the liquid confinement. In this case the thermodynamic and kinetic properties of the evolution of the plasma plume, and further are greatly influenced by the confinement from liquids. Therefore the laser ablation products are different from that of LA in vacuum or diluted gas. The understanding of fundamental aspects of the evolution of the plasma plume from laser ablation of solids in liquids is essential to control the materials processing by this advantageous technology.

Similarly, the LPP will be generated directly, following interaction of incident pulsed laser and solid target. Once it is generated, it is confined by the liquid. The confinement of liquids could drive the laser-induced plasma into the thermodynamic state that definitely differs from that of laser ablation in gas environments. The fundamental aspects related to

formation evolution and condensation of the plasma plume are illustrated schematically in Figure 2.2 according to the references.[15-16] At the initial stage of the interaction of incident laser pulse with the interface between the solid and the liquid, species are ejected from the solid target surface which have a large kinetic energy. Due to the covering effect of the liquid, these ejected species form a dense region in the vicinity of solid-liquid interface. This stage is similar to that which occurs in vacuum or diluted gas with low pressure, where the laser ablation generates plasma "plume". This phenomenon was previously described in detail demonstrate higher pressure and higher density than that formed in vacuum or diluted gas and is accompanied by a localized high temperature.

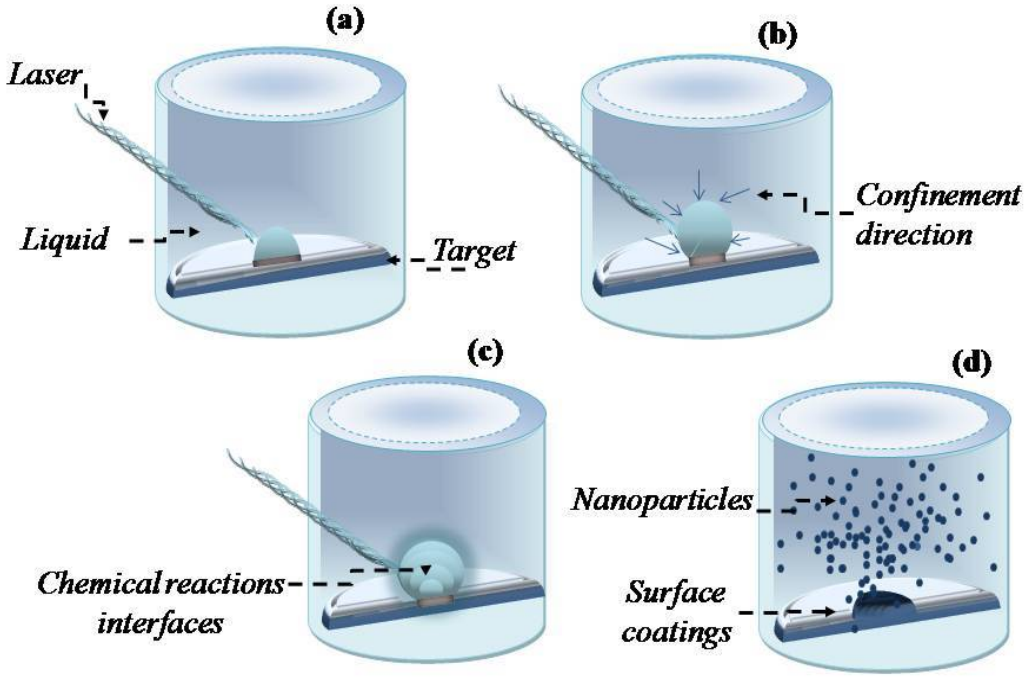

Figure 2.2: The PLAL process can be divided into four stages as follows:
(a) Early stage: laser energy absorption, material ejection, plume formation.
(b) 1st Intermediate stage: plume expansion in the presence of a confining liquid environment.
(c) 2nd Intermediate stage: plume mixing with the liquid, four kind of chemical reactions taking place inside the plasma and liquid and at the interface between the plasma and liquid.
(d) Last stage: NP coalescence/aggregation processes is used to fabricate nanoparticles in liquid and to prepare surface coatings on the target surface.

In the laser ablation of a solid target in liquid environment, since the plasma plume is generated under a confinement by the liquid, it expands adiabatically with supersonic velocity creating two *shock waves* (SW): one is propagating inside the target (SW_1) and another one is moving outside through the liquid material (SW_2), as it was shown by

Fabbro and co-workers.[17-18] When the target absorbs the later part of the laser pulse, the quantities of evaporate species from the solid target raise. Then the shockwave will induce an instantaneous extra pressure in the laser-induced plasma. This "*laser induced pressure*" (L.I.P) will result in the temperature increase in the plasma.[19] The plasma plume formed in a liquid

During the transformation stage of *laser induced plasma* (LIP) interesting chemical reactions occur. Four kind of chemical reactions can take place in the LIP and at the interface between LIP and liquid. Figure 2.2(c) illustrates schematically these chemical reactions mentioned above.

The 1st type chemical reactions occur inside the laser-induced plasma. Since the laser-induced high-density plasma is in a state with high temperature and high pressure, the new phase, a new metastable phase could form by the high temperature chemical reactions between the species ejected from the target.

The 2nd type chemical reactions take place inside the laser-induced plasma, and here the reactant species are from the target and the liquid. At the interface between the laser-induced plasma and the liquid new thermodynamic conditions take place, which create new plasma from the liquid molecules at the interface, the new plasma is called *Plasma Induced Plasma* (PIP), which can be rapidly mixed into the LIP once it is generated. Thus the chemical reactions between the ejected materials and the species from the liquid molecules excitation would occur inside the LIP.

The 3rd type chemical reactions are a result of the thermodynamics condition presented by the LIP, which provides a good opportunity to the high-temperature chemical reactions between the ejected species from the target and the molecules of the liquid. This reaction takes place at the interface between LIP and the liquid.

The 4th type chemical reactions are caused by the extremely high pressure in front of the laser-induced plasma which will impinge the ejected species from the solid target at the plasma-liquid interface into the liquid, and then, the chemical reactions between the ejected species and the liquid molecules will occur inside the liquid. These chemical reactions provide occasions for the fabrication of new materials by the combination of the elements of the target and the liquid.

The condensation of LPP formed by species by cooling down of surrounding liquid is the last stage in the process evolution of pulsed laser ablation of solid target in liquid. Like the PLA in vacuum, the condensation process depends on thermodynamic and kinetic of condensation. Generally there are two different kind of condensation. In one kind of condensation the plasma plume condenses and deposits back on the surface of the solid target during the plasma quenching in the liquid due to the confined pressure from the liquid. This leads to the surface coating formation, and a special *pulsed laser deposition* (PLD) method has been developed to prepare surface coatings in a liquid environment.[20-21] Another kind of condensation (involved in the nucleation, and growth of nanocrystals) takes place during LIP evolution and in shorter quenching time, which can be achieved in the confining liquid.

Clearly, in the PLA in liquids, the plasma with high temperature, high pressure and high density can continuously etch the solid target at the plasma-solid interface to promote the total ablation, which can be achieved in the confining liquid. Thermodynamically these facts favor the nucleation leading to formation of small nanoparticles (n-monomer nucleus) and open a unique route to synthesize nanostructures, especially metastable nanophases. The mechanisms involved in the formation are not well understood. Up to date few works have addressed this topic. [22-16-15] As a general approach, the physical and chemical tools involved in the processing of these phenomena were limited in the thermodynamic nucleation of clusters, phase transition, and growth.

The laser pulse duration and laser intensity affect the nanoparticles size and density. In the case of ultra-short laser pulses and when plume does not absorb laser energy, a collisional quenching effect occurs at the delays of only several microseconds. By that time, the size of NPs is rather small, and their typical size distribution can be fitted by a decreasing function.[23-24] If laser pulse is long or many laser shots are applied, particles absorb laser radiation and a liquid temperature increases, so the final size distribution of NPs and their mean hydrodynamic diameter can be affected.[25] Other possibility, which allows to formation of nanoparticles by laser ablation in liquid, is based on the fragmentation mechanism, a laser-induced Columbic explosion, which involves ejection of photoelectrons or thermal electrons from the surfaces of target nanostructures, leaving positive charges behind on the surface. The induced surface charges derive electrostatic repulsion between different parts of the primary particles, thus causing consequent fragmentation of a single particle into several smaller ones.[26-27] Recent theoretical

investigations suggested that the fragmentation is the dominating process for femtosecond laser irradiation, while purely thermal evaporation occurs for nanosecond laser irradiation, even with an excitation UV-wavelength.[28-29]

Here, we describe a very simple, single step method for a fast and scalable synthesis of nanoparticles in stable colloids. The interaction of the laser with the target causes the surface to vaporize in the form of an ablation plume, which contains species such as atoms, ions, and clusters, travelling with high kinetic energy. The species in the plume collide and react with molecules of the surrounding liquid, producing new compounds containing atoms from both the original target and the liquid. Due the intensity of the laser and the nanosecond timescales, the instantaneous temperatures and pressures within the reaction volume can be extreme (many thousands of K at tens of GPa).[30]

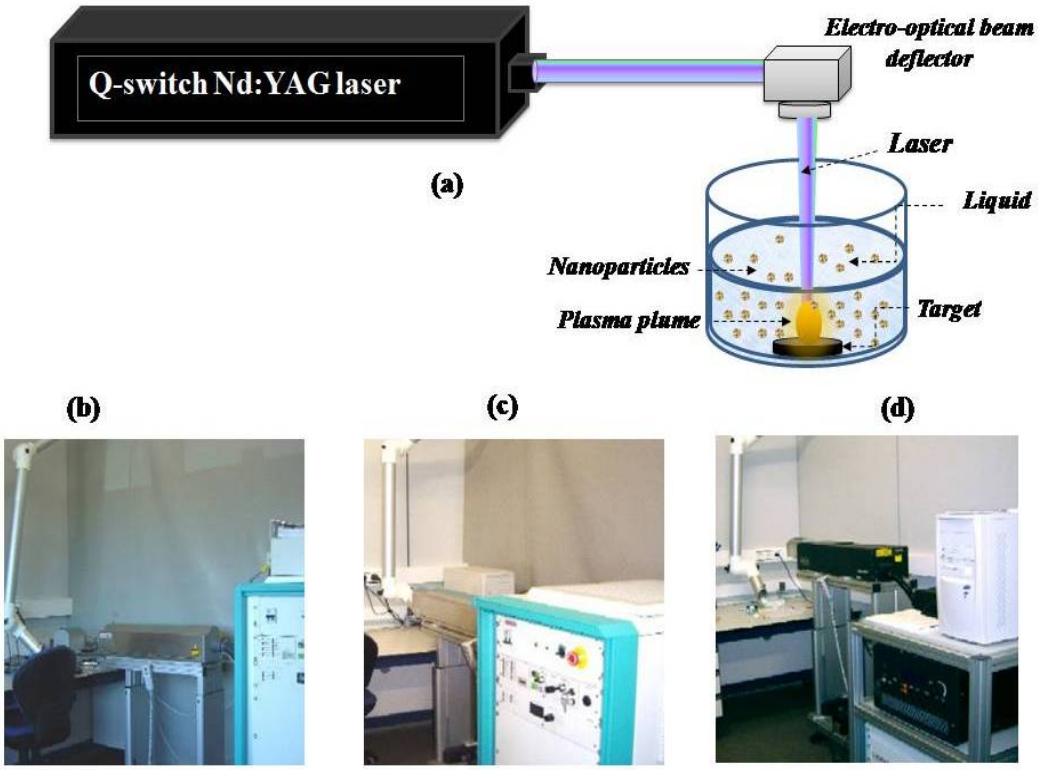

Figure 2.3: (a) Scheme of the experimental setup. (b), (c) and (d) are images of real laser systems used in this work*: 3 W Nd:YAG AVIA* 3rd harmonic (355 nm), *5 W Nd:YAG AVIA* 2nd harmonic (532 nm) and *12 W Nd:YAG AVIA* fundamental (1064 nm), respectively.

Such high temperature, high pressure, and high density conditions provide a 'brute force' method of synthesizing novel materials that have hitherto been inaccessible using milder, more conventional techniques. The proposed method of synthesis is based on the

laser irradiation of a given solid target immersed in a liquid, using the simple experimental setup shown in Figure 2.3.

In this work we have used various type of lasers like a 3rd harmonic (λ =355 nm) - 2nd harmonic (λ =532 nm) of a *Q-switch Nd:YAG* laser, giving pulses < 40 ns wide at a repetition rate of 5 kHz. The exact focal position of the beam on the sample surface could be found by viewing the beam through a mirror (by wearing laser protective glasses).

The solid target, such as GaAs, silicon, germanium and tungsten (purity of 99.99%), is placed and fixed in a holder and submerged under variable levels (several millimeters) of liquid. The liquid-containing vessel may be open, or include a transparent window in order to prevent splashing during the PLAL process. Laser pulses of a given energy (fluence) are arriving at the target during a fixed processing time (minutes to hours) in order to produce a sufficient quantity of nanoparticles. As an advantage, our experimental set-up is equipped by an *electro-optical beam deflector* (BF), which is computer controlled and hence the laser beam can sweep a chosen pattern on the target surface. In this way, the PLAL process developed during a giving time period is not taking place at the same surface site, but sweeping a given surface area. For example, in typical processes, 1 cm^2 of the target surface was swept at a rate of 30 lines/s, which is equivalent to 1000 lines/cm. In this way, a reduction in the density of fissures at the target surface, production of big target fragments and undesired particles, is expected. At the same time, nanoparticles generated by PLAL in this way are moving away from the ablation site and experiences enough cooling before returning to the same site (due to liquid circulation induced by the PLAL process in a smaller container).

2.1.3. Samples and experimental conditions

Colloidal GaAs

A bulk GaAs target is placed at the bottom of a glass vessel containing 20 ml of a liquid, such as methanol or ethanol with a purity of 99.99 %. The laser used for PLAL is the 2nd harmonic (green) of Nd:YAG laser (λ = 532 nm) generating pulses of 10 ns duration at a maximum repetition rate of 5 KHz. The laser radiation was focused on the target surface to deliver power densities (fluences) per pulse below 14 J/cm^2. After a few minutes of the GaAs target irradiation (see sweeping details in last section) at room temperature, the appearance of nanoparticles is clearly observed by a change of the liquid

color. In a second stage, NPs were covered with amorphous SiO_2 by hydrolysis of *Tetra-Ethyl-Ortho-Silicate* [TEOS, formula $Si(OCH_2CH_3)_4$] at T = 0 ºC by using the well-known *Stöber method* [43]. The preparation consisted in mixing 20 ml of the NP colloidal solution with 250 μl of TEOS and 25 μl of water in an ultrasonic bath. The injection of water and TEOS was made separately to prevent agglomeration and sedimentation effects of SiO_2. The maintenance of a low temperature (T = 0 ºC) during the process to form the NP capping by SiO_2 enables one to avoid a rapid TEOS hydrolysis since the reaction rate is proportional to the H_2O concentration and temperature.

Silicon Nanocrystals

A p-type Cz-silicon wafer of (100) was used as a target, immersed in a liquid medium ($CHCl_3$ or *chloroform*, 20 ml in an open glass vessel), and irradiated with the 3rd harmonic of pulsed Nd:YAG laser (355 nm, 40 ns pulse duration, 5 kHz repetition rate). The laser beam was focused by a lens having a focal length of 60 mm on the silicon target surface with a spot of about 30 μm diameter giving power densities per pulse ≈ 40 J/cm^2 (1 W of average power). The solution was continuously stirred during laser irradiation. An area of 56 mm^2 of the target surface was swept twenty times by the laser beam (see details in the last section) in order to observe the appearance of brownish color of the liquid, but usually hundreds of repetitions are applied to have a colloidal suspension with a sufficiently high concentration of Si nanoparticles, typically microcristalline.

After the PLAL processing an appropriate physicochemical post-treatment was applied to obtain small-size monocrystalline silicon nanoparticles (NPs). Firstly, the chloroform suspension was transferred to a plastic vessel and chloroform evaporated under vacuum. Secondly, the precipitate formed on the vessel bottom was re-dissolved in a mixture of *isopropanol*, HF and *hexane* (3:1:3), and immersed in an ultrasound bath.

Metal nanoparticles

The proposed method of synthesis is based on the laser irradiation of a given solid target immersed in a solution of metal salts. The laser used for PLAL is the 3rd harmonic (λ = 355 nm) of a *Q-switch Nd:YAG* UV laser, giving pulses of around 40 ns wide at a maximum repetition rate of 5 kHz. The laser power densities per pulse on the target surface were always below 40 J/cm^2 (1 W of average power). Several targets such as silicon, germanium, and tungsten with a purity of 99.99% were placed at the bottom of a glass vessel containing 20 ml of $AgNO_3$ ($HAuCl_4$ or a mixture of both salts) in a water

solution in order to produce silver (gold and a silver-gold alloy) NPs. (Patent: WO2009030799-A1)

2.1.4. Transmission Electron Microscopy (TEM), Size & Crystallinity.

Transmission electron microscopy (TEM) is an imaging technique in which a beam of electrons is transmitted through an ultra-thin specimen, interacting with the specimen as it passes through.[31] An image is formed from the interaction of the electrons transmitted through the specimen; the image is magnified and focused onto an imaging device, such as a fluorescent screen, on a layer of a photographic film, or to be detected by a sensor such as a CCD camera.[32] TEM systems are capable of imaging at a significantly higher resolution than optical microscopes, owing to the small de *Broglie wavelength* of electrons. The first TEM was built by *Knoll* and *Ruska* in 1931, having a resolution greater than that of light in 1933 and the first commercial TEM is dated in 1939.

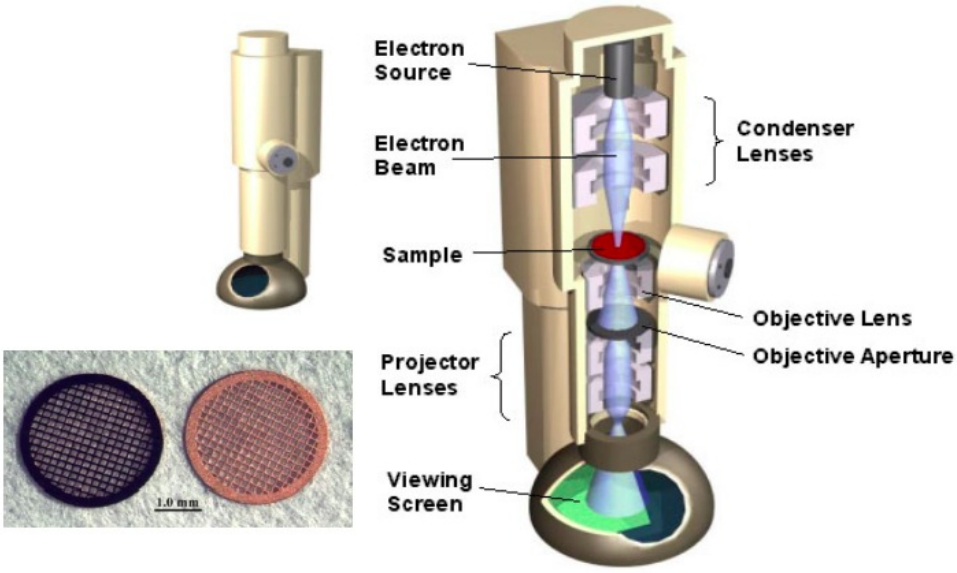

Figure 2.4: Scheme of a transmission electron microscope and images of TEM grids used as sample holders.

TEM or high resolution TEM (HRTEM) has been the analytical workhorse of nanostructured materials for the past three decades. It can be used to determine particle size, shape, and surface structure more precisely than other techniques. A schematic of the essential features of a TEM is shown in Figure 2.4. The high voltage is typically set between 100 and 300 kV, although this can be as high as 1000 kV. A TEM can be operated in many different modes and can combine many analytical techniques, making it a very versatile tool for the composition and structure of nanoscale materials.

If the aperture is placed to allow only the transmitted (un-diffracted) electrons, a *bright-field* (BF) image is formed. If the aperture is placed to allow only a set of diffracted electrons, a *dark-field* (DF) image is formed. In a BF image, areas that are thick and/or made of a high-Z material will appear darkest. In a DF image, the areas which have caused diffraction inthe selected direction will appear brightest; this can be very useful when determining the orientation of crystallites and defects. In HRTEM, the transmitted (forward scattered) beam and at least one diffracted beam are collected. These beams result in an interference pattern, which must be translated into an image, giving rise to the other name for HRTEM, phase contrast imaging.[31] It is important to note that HRTEM does not "image" individual atoms, but rather gives interference patterns generated by columns of atoms. In this work we have used a *JEOL JEM 1010* and a *TECNAI G2 F20* (FEI) with the following properties:

- 40 to 100 KV of acceleration voltage.
- Side entry goniometer stage, two specimens.
- Tilt to +/-60º.
- High contrast objective (FL=5mm).
- Point resolution: 0.45 nm.
- Lattice resolution: 0.2 nm.
- Bright and dark field imaging.
- Selected area and microbeam diffraction.
- Gatan cold trap and Gatan Bioscan CCD camera.

- 80 to 200KV of acceleration voltage.
- Schottky Field emitter.
- High Maximum beam current (> 100 nA).
- High current in probe (0.5 nA in 1 nm spot).
- Point resolution: 0.24 nm.
- Lattice resolution: 0.1 nm.
- Excellent information limit (<0.15 nm)
- High tilt (40º) and large field of view.
- Maximized tilts for any X, Y, Z α, β, combination.
- Embedded EDX and EELS spectrum imaging available.

We note that in the present work the size distributions of NPs is based on TEM images by counting more than 500 NPs using *image pro-plus* software.

2.1.5. X-ray photoelectron spectroscopy XPS, chemical analysis.

XPS is a sensitive and surface-sensitive quantitative spectroscopic technique that measures the elemental composition, empirical formula, chemical state and electronic state of the elements that exist within a given material. The main components of a conventional XPS spectrometer are an X-ray source (typically an Mg or Al anode), a sample holder, and an electron detector (cylindrical mirror analyzer (CMA) or hemispherical analyzer) housed in an ultrahigh vacuum chamber. The sample is irradiated with X-rays (Mg K_α = 1253.6 eV, Al K_α = 1486.6 eV) that results in the ejection of photoelectrons, Figure 2.5.

Photoelectrons can be generated from either core levels or valence levels, although core level photoelectrons are the more commonly investigated for chemical analysis because they have a much higher photoionization cross section. The binding energy (BE) of emitted electrons is indicative of the element and chemical state of the atom they are ejected from and can be calculated by: $E_K = h\vartheta - BE - \emptyset_s$ where $h\vartheta$ is the photon energy of the incident X-rays, E_K is the kinetic energy of the detected photoelectron, and $\emptyset_s$ is the work function of the spectrometer.[34] The number of peaks produced by a single element varies from 1 to more than 20. Tables of binding energies (BEs) that identify the shell and spin-orbit of each peak produced by a given element are included with modern XPS instruments, and can be found in various handbooks [35] and websites.[36]

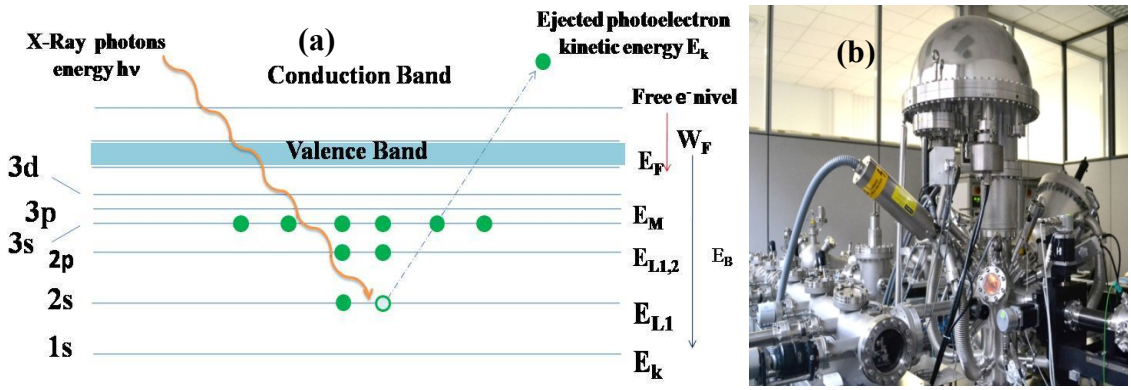

Figure 2.5: (a) Photoemission principle: when an x-ray (orange arrow) impinges on the sample surface, some electrons (green spheres) become excited enough to escape the atom. (b) Image of XPS system.

2.1.6. X-ray Diffraction: structure, composition and size.

X-ray diffraction (XRD) analysis is based on the interference between X-ray waves scattered from multiple planes in a certain crystallographic orientation (Figure 2.6). Constructive interference, which gives rise to peaks in the diffractogram, [37] arises when the path length of the top and bottom rays is equal to an integer number of wavelengths (*bragg's low*):

$$n\lambda = 2dsin(\theta)$$

For a particular set of crystallographic planes in a cubic crystal with lattice parameter a_0 and Miller index *(hkl)*, the angles at which diffraction peaks occur (except those not allowed by the structure factor of the crystal) are: $2\theta_{hkl} = 2\arcsin\left(\frac{\lambda(\sqrt{h^2+k^2+l^2})}{2a_0}\right)$

Lattice constants can be determined by XRD and can be useful in the determination of the structure and composition of bimetallic nanoparticles. For very small nanoparticles, the lattice constant increases slightly. If NPs are single crystalline, their size can be inferred from the broadening of the diffraction peaks. For an infinite crystal, diffraction intensity only occurs exactly at the Bragg angle, θ_B, but as the number of crystallographic planes decreases, this constraint loosens and partial constructive interference gives rise to a broadening of the diffraction peaks. The full-width at half maximum (FWHM), $\Delta\theta$, for diffraction from N planes is given by: $\frac{\Delta\theta}{\theta_B} = \frac{0.9}{N}$. For nanoparticles, the average particle size D (or crystallite size if the particles are not single crystalline) size has been estimated by using *Debye-Scherrer* formula [38, 39] is approximately given by: $D = \frac{0.89\lambda}{\Delta(2\theta)cos\theta}$

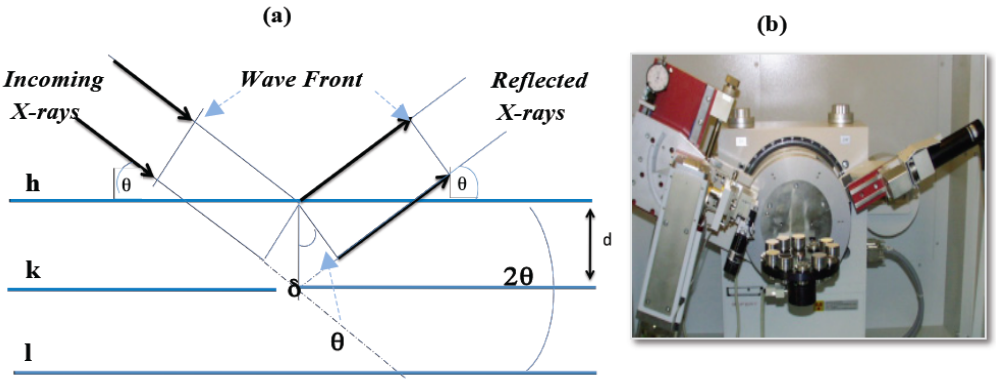

Figure 2.6: (a) Bragg Formulation of X-Ray Diffraction. (b) Image of the X-Ray Diffractometer *Seifert TT 3003 – STD.*

2.1.7. Optical Spectroscopy Techniques

- **UV-visible electronic absorption spectroscopy**

UV-vis spectroscopy [40] is named electronic absorption spectroscopy because the absorption in the UV-visible regions involves mostly electronic transitions.[41]Based on Beer's law, the absorbance, *A*, is related to the incident light intensity, $\mathbf{I_0}$, and transmitted light intensity, **I**, concentration of a solution sample, **c**, path length of the sample, ***l***, absorption coefficient, **α**, and molar absorptivity, **ε**, by the following equation:

$$\boldsymbol{A = log\frac{I_0}{I} = \varepsilon lc = \alpha c}$$

In an experiment (Figure 2.7), both $\mathbf{I_0}$ and **I** can be measured and thus **A** can be determined experimentally. If ***l*** and **c** are known, the absorption coefficient can be determined from last equation. The absorption coefficient is wavelength dependent and a plot of **α**as a function of wavelength **λ** is the spectrum of interest.

Instrument: UV-visible spectrometer:

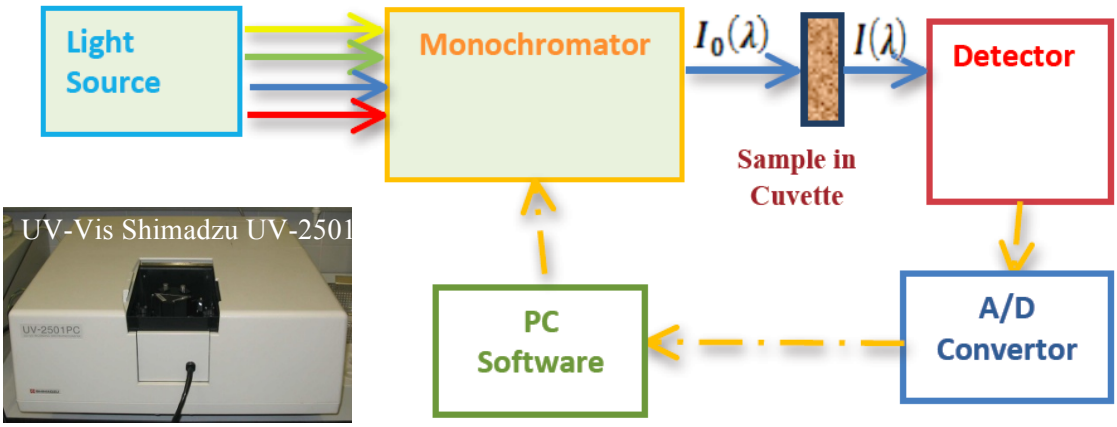

Figure 2.7: Schematic diagram of key components of a typical UV-vis spectrometer that includes a light source, e.g. a lamp, monochromator to disperse the incident light, sample cuvette and holder, detector, e.g. PMT, photodiodes or CCD, analog-to-digital (A/D) convertors, and computer with software to control the scan of the monochromator and data acquisition.

- **Photoluminescence spectroscopy**

At the fundamental level, the principle underlying photoluminescence (PL) spectroscopy is very similar to that of electronic absorption spectroscopy.[42] They both

involve electronic transition of initial and final states coupled by the electrical dipole operator. The main difference is that the transition involved in PL is from a higher energy level or state to a lower energy level. A typical PL spectrum is just a plot of the PL intensity as a function of wavelength for a fixed excitation wavelength. Figure 2.8 shows a schematic of the key components of a typical set up used for PL measurements. While several components are similar to that in a UV-vis spectrometer, including light source, sample cuvette and detector, the detection scheme is different.

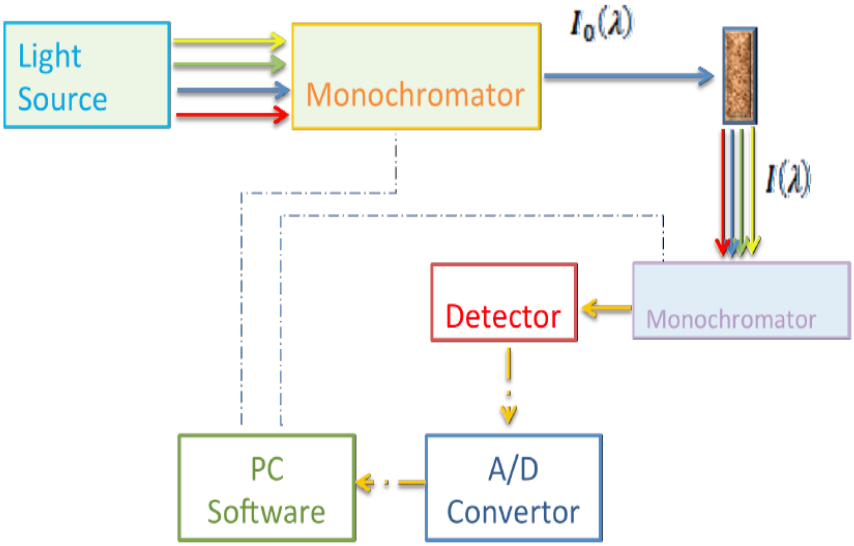

Figure 2.8: Schematic illustration of the key components in a typical spectro-fluorometer that include a light source, e.g. a lamp, monochromator to disperse the incident light, sample cuvette and holder, a second monochromator to disperse the emitted light, detector, e.g. PMT, photodiodes or CCD, analog-to-digital (A/D) convertors, and computer with software to control the scan of the monochromators and data acquisition.

Rayleigh scattering, which has the same wavelength as the excitation light, should be avoided in the detection of PL. Basically, in a typical PL set-up, a specific wavelength of light is selected from a light source by a monochromator, and directed at the sample of interest. Light emitted from the sample is collected through lenses, dispersed by another monochromator, and detected by a photo detector. The analog electrical signal generated by the photo-detector is converted into a digital signal by an A/D (Analogue to Digital) convertor and processed by software on a computer. The spectrum is displayed in terms of intensity of emitted PL light as a function of the wavelength of emitted light

We outline that photoluminescence (PL) and time resolved PL (TRPL) measurements was realized in collaboration with the Department of Physics, Lomonosov Moscow State University. PL and TRPL spectra are measured under excitation with a N_2-laser

(wavelength λ = 337 nm, pulse duration τ = 10 ns, pulse energy E = 1 μJ, repetition rate ν = 100 Hz). The laser beam was focused by using a 20 cm lens into a spot of about 1 mm in diameter onto the sample (Si NPs on a quartz plate deposited by suspension dropping cast method). PL signal was collected on a 50 cm spectrometer equipped with a S1 photomultiplier (time resolution of 100 ns). The Raman spectra were measured by using an equipment of the Center of User's Facilities of Lomonosov Moscow State University

2.2. GaAs nanoparticles produced by PLAL in organic liquids

In the present work we report the preparation of stable colloidal solutions of GaAs quantum dots (QDs, i.e. NPs possessing sufficiently small size to exhibit quantum confinement effect) by PLA of the corresponding bulk material in liquids and the investigation of their optical and structural properties. The absorption spectra of the colloids exhibit blue shift of the band gap edge as compared to bulk GaAs, which is better observed in the case of NPs capped with SiO_2, the shift being consistent with the measured average size of GaAs QDs (about 8–10 nm, depending on the PLA conditions). The NPs are typically polycrystalline, but perfectly monocrystalline NPs or monocrystalline NPs with planar defects were also detected. As a way to improve stability of the GaAs NP colloids and to have more possibilities for their applications, we have also encapsulated GaAs NPs into SiO_2 shell by a standard chemical technique. Silica surface is known to be well suitable for easy functionalization by thiol, amine, and carboxylate molecules.[44][45]

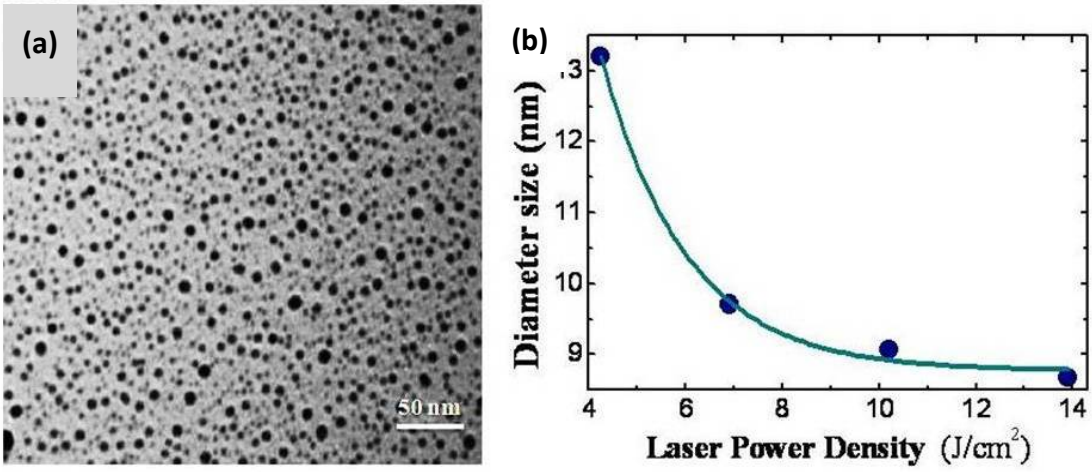

Figure 2.9. (a) TEM micrograph of GaAs nanoparticles grown by laser ablation in methanol using a laser power density per pulse (*fluence*) of 4.25 J/cm^2. (b) The average size is plotted as a function of the laser fluence.

GaAs colloidal QDs were grown by using a simple experimental approach based on the laser irradiation of a bulk GaAs target placed at the bottom of a glass vessel containing 20 ml of methanol with a purity of 99.99%. The laser used for ablation is a 2nd harmonic (green) Nd:YAG laser (λ = 532 nm) generating pulses of 10 ns duration at a maximum repetition rate of 5 KHz.

Figure 2.9(a) shows the TEM image obtained for GaAs NPs produced by laser ablation in methanol and then drop casted on carbon-coated copper grids. The GaAs NPs are predominantly spherical in shape (Fig. 2.9(a)) and exhibit a size dispersion, which depends on the laser power density used for a GaAs target ablation: the dispersion is rather wide for the low laser fluence (4.2 J/cm^2) and considerably narrows under increase of the excitation power density (not shown). In particular, the dispersion of the NPs diameter measured at half of the dispersion curve maximum is only 2.5 nm for the highest laser fluence used that is rather close to the values known for NPs obtained by chemical synthesis (around 1 nm).[46] The absolute value of the average diameter also decreases significantly, from 13.7 to 8.7 nm, as the laser fluence from 4.25 to 13.9 J/cm^2. Figure 2.9(b) shows this variation, which can be well fitted by an exponential decrease of NP diameter as a function of PLA laser fluence. This behavior is consistent with the existence of a threshold power to obtain NPs that can be a result of the plume plasma confinement in a liquid and the corresponding increase of temperature and pressure caused by increasing laser power.

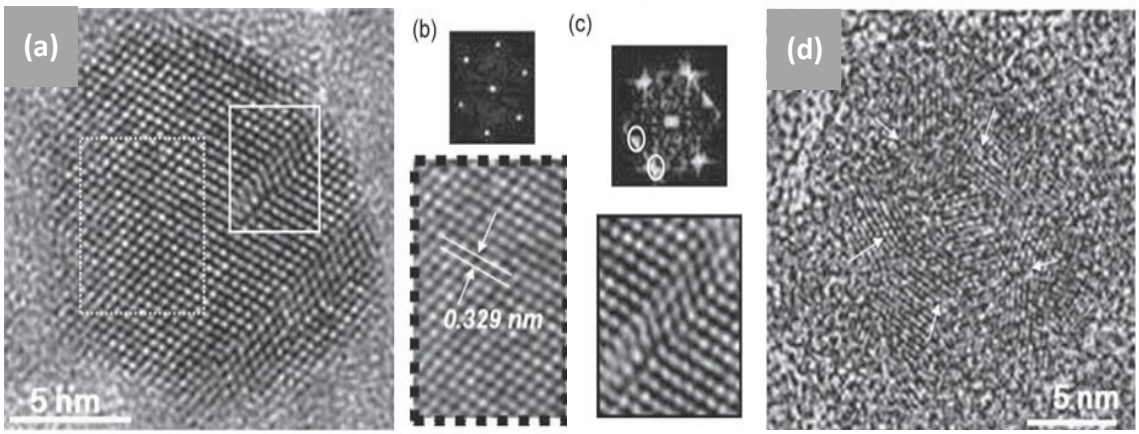

Figure 2.10. (a) HRTEM image of a nanoparticle of GaAs prepared by laser ablation in methanol with the laser power density 4.25 J/cm^2. (b) Perfect crystalline area within the dashed square of HRTEM image (a) with its corresponding FFT. (c) Area within the solid square in (a) exhibiting twinning with its corresponding FFT showing characteristic spots from this defect. (d) HRTEM image of a polycrystalline nanoparticle. White arrows mark the position of polycrystalline grains in the nanoparticle.

We obtained also HRTEM micrographs of GaAs colloidal QDs produced in our PLAL experiments. Most of them have been identified as possessing edge dislocations, promoting some portions of the nanocrystals along the direction perpendicular to the dislocation, as well as micro-twin boundaries and even multi-twin defects.

However, as shown in Figure 2.10(a), single twin boundaries do not exclude that the growth of the particles can occur following a preferential crystallographic orientation. This orientation can be determined, for example, on the basis of the magnified images of the two areas marked by solid and dotted squares in HRTEM micrographs shown in Figure 2.10(a).

The magnified image of the dotted square area is shown in Figure 2.10(b). It corresponds to the face-centered cubic *(fcc)* structure with a periodic fringe spacing of 0.329 nm, associated to {111} planes of bulk GaAs.[47] This can be clearly observed in the Fast Fourier Transformation (FFT) image obtained from the real image of the GaAs quantum dot crystalline material (upper image in Fig. 2.10(b)). On the other hand, an example of crystalline defects is displayed in the HRTEM image of Figure 2.10(c), the image corresponds to the solid square area of Figure 2(a). An analysis of this image and its respective FFT (see Fig.2.10(c)) shows that the defect is a microtwin. Such twin defects can alter the right crystal growth by giving rise to surfaces with multiple crystallographic orientations. Figure 2.10(d) shows an example of a HRTEM image of a NP consisting of several polycrystalline grains, which are marked by white arrows. These defects can arise from condensation effects of laser ablation during NPs production rather than from strain relaxation.[48]

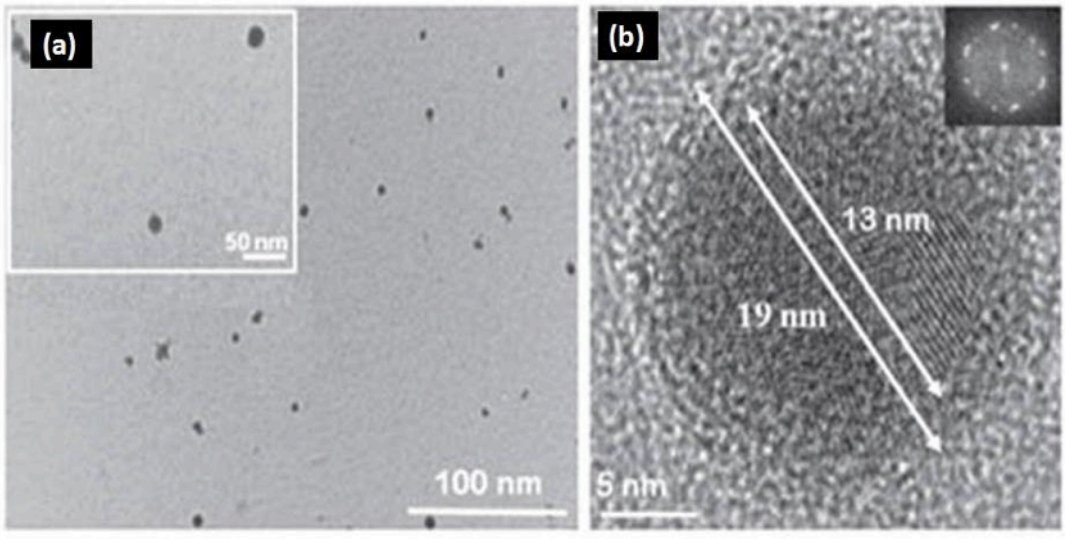

Figure 2.11. TEM micrographs (a) and HRTEM image (b) of GaAs/SiO_2 core/shell nanoparticles. The core diameter is about 13 nm and the shell thickness is 3 nm. The inset shows the FFT from the HRTEM image.

GaAs-SiO_2 core–shell particles of nanometer dimensions have also been prepared in the present work via the chemical procedure based on hydrolysis of TEOS ($Si(OCH_2CH_3)_4$) at 0º C in a GaAs NP colloidal solution previously fabricated by laser ablation at a laser fluence close to the maximum values used. The SiO_2-covered NPs have an average diameter of about 14 nm (Figure 2.11(a)), that is, they are larger than bare NPs obtained with the use of a laser fluence of 13.9 J/cm^2. This difference is consistent with the incorporation of SiO_2 as an outer shell capping GaAs NPs that is demonstrated by the HRTEM image in Figure 2.11(b). The core diameter and the thickness of the silica shell measured for several NPs by HRTEM were found to be in the ranges of 8–13 nm and 3–6 nm, respectively. These values are consistent with the average GaAs/SiO_2 diameter (14 nm) and that of bare GaAs NPs (8,7 nm), i.e., the average SiO_2 shell thickness would be 2,7 nm, very close to the values measured by HRTEM in some NPs arbitrarily selected.

As one can see from the Figure 2.12, the absorbance spectra of uncapped and SiO_2 capped GaAs NPs are rather different. The plot is made logarithmic after substracting a λ^{-4} background in order to better distinguish intrinsic features that could be associated to optical transitions in the NPs. A first absorption edge can be distinguished at around 1.75 eV in the case of SiO_2 capped GaAs NPs, whereas any feature (a monotonous increase) is observed in bare GaAs NPs. In the range 3.1–3.3 eV a second band edge is observed in both kinds of NPs (a broad maximum in the case of capped NPs).

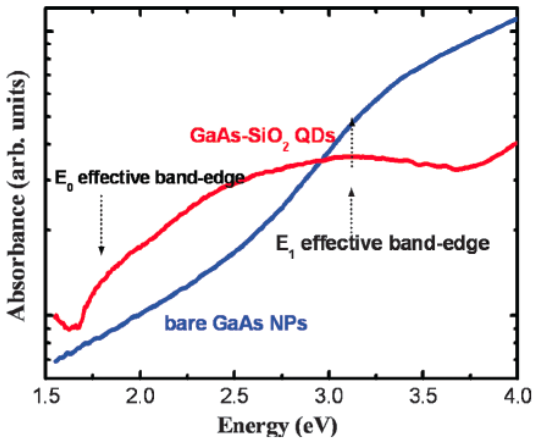

Figure 2.12. The absorption spectra of uncapped and SiO_2-capped GaAs NPs.

2.3. Small silicon nanocrystals produced by PLAL of a Si target in organic liquids and etching

A p-type Cz-silicon wafer of (100) orientation was ultrasonically rinsed first with deionized water and then with ethanol for 1 h. The cleaned silicon wafer was used as a target, immersed in the liquid medium under study ($CHCl_3$, or chloroform, 20 ml in an open glass vessel) and irradiated with Nd:YVO_4 laser 40 ns pulses (Coherent) at 355 nm, with 5 kHz repetition rate and giving power densities per pulse ~ 40 J cm^{-2}. Silicon NPs are produced in chloroform due to such a procedure (Figure 2.13) and are found to be spherical in shape (Figure 2.13(a,b)) with an average diameter around 50 nm, as can be obtained from the size distribution shown in Figure 2.13(d). We found that these NPs are polycrystalline and suggested that they may consist of at least two materials: small Si crystallites visible in HRTEM images (see Figure 2.13(c)) and silicon dioxide produced due to the presence of dissolved molecular oxygen in the liquid.

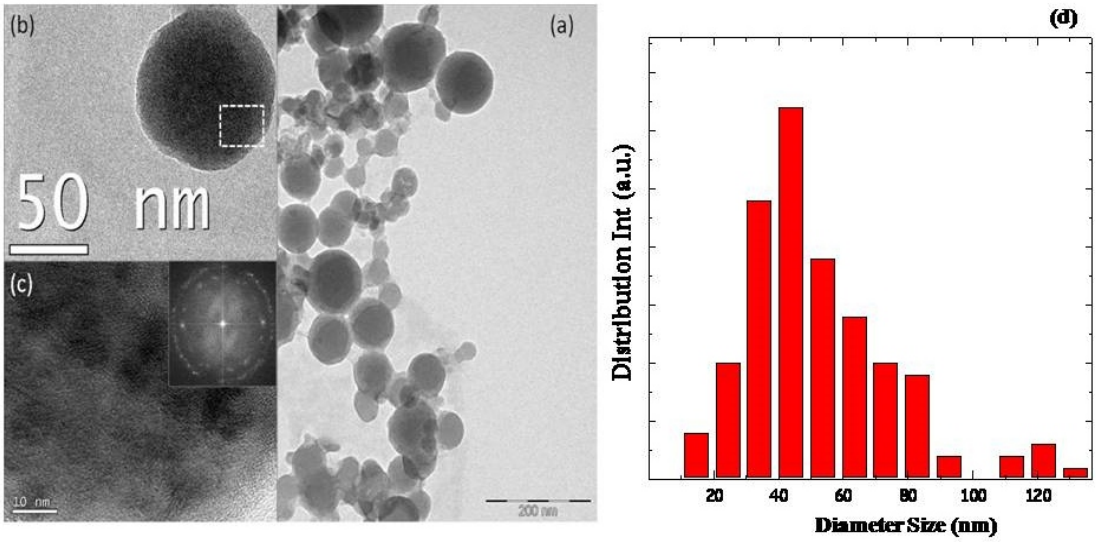

Figure 2.13: (a) TEM micrograph of silicon nanoparticles produced by laser ablation in chloroform. (b) HRTEM image of one big nanoparticle. (c) Amplified HRTEM image of the rectangular area outlined in (b); the Fast Fourier Transformation (FFT) pattern is shown as an inset. (d) Size distribution calculated from TEM images of Si nanoparticles obtained by nanosecond laser ablation in chloroform.

We hypothesized that these complex structures can be disintegrated with simultaneous release of monocrystalline Si nanocrystals (Si-NCs) by applying an ultrasonic treatment for disaggregation of the multicrystalline aggregates and subsequent immersion in a HF

solution for silicon dioxide etching. The treatment consists of several steps, as illustrated in Figure 2.14. After complete evaporation of chloroform the vessel was filled with a mixture of solvents isopropanol/HF/hexane (3:1:3), after shaking by hand for a few seconds, the liquid mixture splits into two parts: (1) a bottom (polar) part consisting of isopropanol, water (as a part of the HF solution) and HF, and (2) an upper (nonpolar) part consisting of hexane.

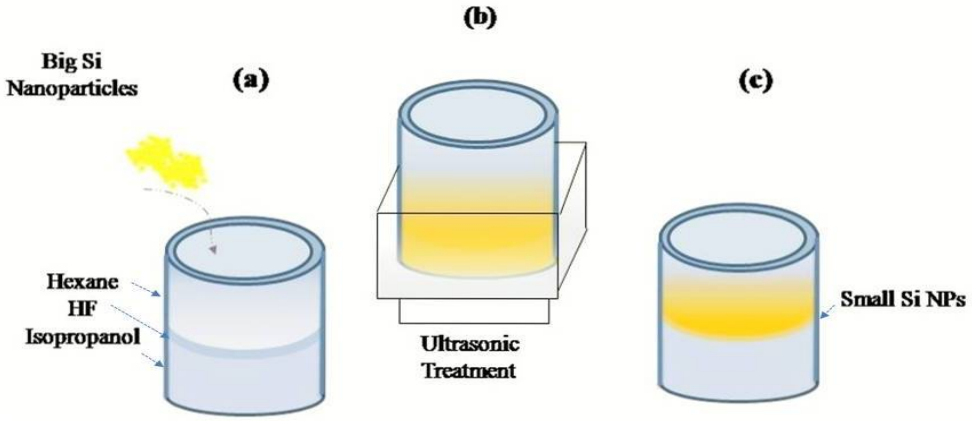

Figure 2.14. Illustration of the procedure applied to initial Si NPs suspension for disaggregation of the initial big NPs: (a) chemical treatment in isopropanol /HF/ hexane (3:1:3) together with (b) a strong ultrasonication; (c) localization of small Si NPs in the upper layer.

Next, the suspension was subjected ultrasonic treatment for 30 min. As a result, the bottom layer of the mixture became transparent, whereas the upper layer (hexane) acquired a yellowish color because most of Si NPs were transferred to this layer as a result of Si NPs surface hydrogenation due to the contact with HF

TEM micrographs of Si NCs after combined ultrasonic and chemical (HF) treatment are shown in Figure 2.15. By increasing the magnification we can see, on the periphery of the big agglomerate formed due to solvent evaporation process, the presence of individual nanoparticles and small clusters of them consisting of a few NPs (Figure 2.15(a,b)). Figure 2.15(c) shows typical HRTEM image of one such individual nanoparticle. Interplanar spacing can be directly determined from the images by measuring the lattice fringes. In addition, the Fast Fourier Transformation (FFT) was also applied to the HRTEM image, allowing one to identify the family of diffracting planes in that region. An interplanar spacing of ~ 3.1 Å (spots 1, 2 at the left top inset, which coincides with the value for (111) planes of Si, confirms our interpretation of the data as formation of small monocrystalline Si NCs. Figure 2.15(d) shows the size histogram of these Si NCs

obtained by laser ablation in chloroform with the following ultrasonic post-treatment in the presence of HF. The experimental most probable diameter of Si NCs is around 4 nm approximately.

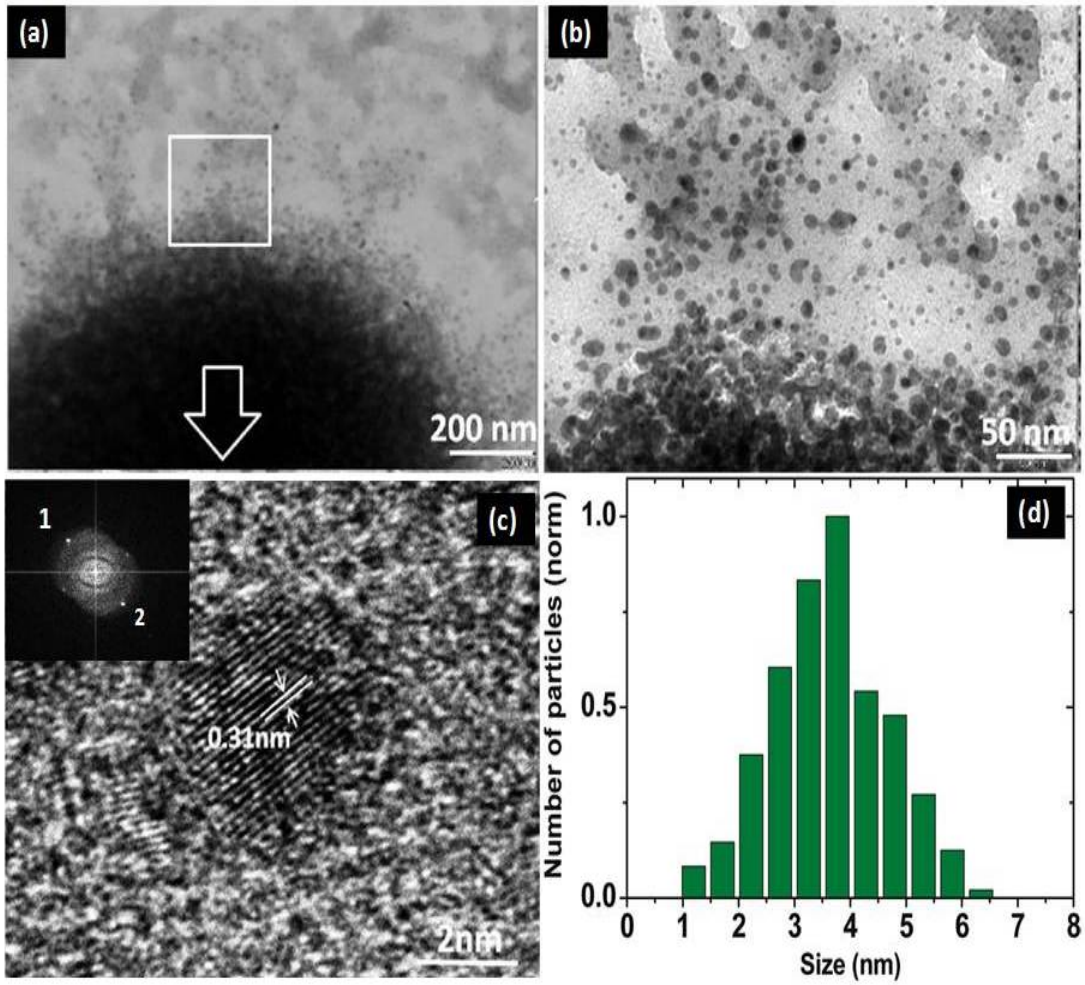

Figure 2.15: TEM micrographs of Si NCs after combined ultrasonic and chemical (HF) treatment: general view of the NC agglomerates formed on the carbon membrane of the TEM grid (a) and individual NCs on the periphery of the agglomerates (b). (c) HRTEM micrograph obtained for an individual Si NC; the inset corresponds to the FFT of a Silicon nanoparticle. (d) Size distribution calculated from TEM images of Si NCs obtained by laser ablation in chloroform and then subjected to ultrasonic/HF post-treatment.

Figure 2.16(a) shows the Raman spectra of Si NPs after the above described post-treatment (red line). For a comparison, Raman spectra of commercial Si NPs from "Aldrich" (blue line), and of bulk silicon (black line) are also shown. It is well known that bulk Si crystal displays a narrow optical phonon resonance at 520.5 cm^{-1}.

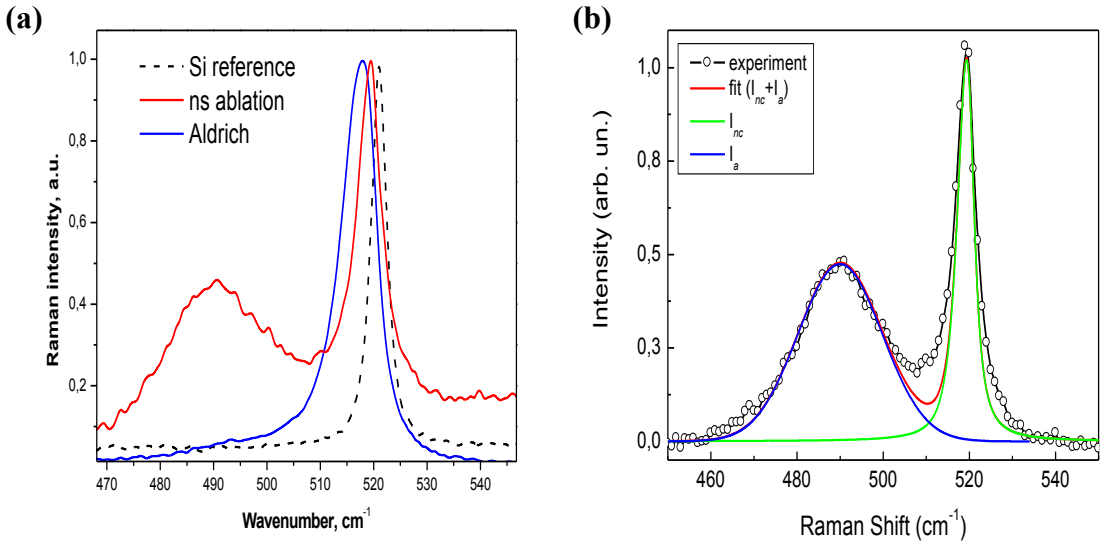

Figure 2.16: (a) Raman spectrum of Si NCs after post-treatment (red) as compared to the spectra of bulk silicon (black) and of 100 nm diameter Si NPs from Aldrich (blue). (b) The same experimental Raman spectrum is shown (open circles) along with the model spectrum (red) obtained by summation of a Gaussian (blue, accounting for the wide band at ~ 490 cm^{-1}) and a modified Lorentzian (green, accounting for the narrow band at ~520 cm^{-1}) curves.

When Si crystallites become small enough (≤10 nm), the Raman phonon band broadens and shifts down in energy, and this shift can be correlated with the crystallite size due to phonon confinement model by this equation. [49]

$$\Delta v = -52.3\left(\frac{0.543}{D}\right)^{1.586} \text{ eq (1)}$$

Where Δν is the shift of the Raman peak position due to spatial confinement in Si NCs compared with respect to the bulk value and D is their size (Δν and D are given in cm^{-1} and nm, respectively).

Besides the band near 520 cm^{-1}, a broad band centered at 490 cm^{-1} is also detected for our Si NCs (Figure 2.16(a)). As one can see in Figure 2.16(b), the experimental two-band Raman spectrum (open circles) can be satisfactorily fitted by the sum of a Lorentzian (narrow resonance at 520 cm^{-1}) and a Gaussian (wide band at 490 cm^{-1}) functions. The lower-energy Raman band is commonly attributed in literature to a disordered (amorphous) Si phase.[50]

Emission properties of our Si NCs have been also studied. It should be noted that, immediately after ultrasonic/ HF post-treatment, Si NCs in hexane suspension do not show any remarkable PL. However, photoluminescence appears if hexane (with HF trace) is replaced by any liquid (in which dissolved oxygen from air can be present) or the Si NCs in the hexane solution is deposited on substrate and kept in air. In both cases the photoluminescence (PL) spectrum is observed in the visible-near IR region, as shown in Figure 2.17(a) for the case of Si NCs dispersed in isopropanol.

The PL spectrum is rather broad (from 400 up to 900 nm) with a maximum near500 nm. In addition to the steady state PL, the PL transients have been also measured (Figure 2.17(b)). The PL decay kinetics can give additional information and shed further light on the nature of the emitting states,[51] at least to distinguish between optically forbidden and optically allowed transitions..

Decay kinetics of the PL presented was measured at 750, 679 and 600 nm within the emission band. Representative PL decay kinetics obtained for 750 nm is shown again in Figure 2.17(b). We applied a three-exponential decay function (red line) for fitting the experimental PL transient (Red line).

$$I_{PL} = A_1 \exp\left(\frac{-t}{\tau_1}\right) + A_2 \exp\left(\frac{-t}{\tau_2}\right) + A_3 \exp\left(\frac{-t}{\tau_3}\right)$$

where τ_i and A_i , i = 1-3, are the three PL decay times and their relative amplitudes. For the kinetics measured at 750 nm, the following PL decay times (relative amplitudes) were obtained: τ_1 = 0.1 μs (A_1 = 0.78), τ_2 = 7.8 μs (A_2 = 0.06) and τ_3 = 63 μs (A_3 = 0.16). At shorter detection wavelengths the PL transient profile remains approximately the same, but the short-lived signal becomes more prevalent. In this way for λ = 675 nm, the PL decay times (relative amplitudes) were found to be τ_1 = 0.08 μs (A_1 = 0.87), τ_2 = 6.3 μs (A_2 = 0.05) and τ_3 = 34 μs (A_3 = 0.08), whereas for λ = 600 nm, τ_1 = 0.1 μs (A_1 = 0.95) and τ_2 = 14 μs (A_2 = 0.05), that is, the shortest PL decay time is dominating completely the PL transient. All these best fitting parameters for the PL transients detected at λ = 600, 675 and 750 nm are listed in Table 1.

λ (nm)	A1	τ_1 (μs)	A_2	τ_2 (μs)	A_3	τ_3 (μs)
750	0.78	0.1	0.06	7.8	0.16	63
675	0.87	0.08	0.05	6.3	0.08	34
600	0.95	0.1	0.05	14	0	--

Table 1: PL decay times τ_i(μs) (i = 1, 2, 3) and their relative amplitudes extracted from a three-decay fitting curve to the experimental TRPL measured at 750, 675 and 600 nm.

Thus, as shown in Figure 2.17, the PL band is not homogeneous and includes the emission of at least two centers with different decay times. Preliminarily, we suggest that emission centers with long-lived luminescence (lifetimes of tens of microseconds) may belong to the excitonic photoluminescence of silicon nanocrystals passivated by oxygen: in this case, yellow-red PL is usually observed possessing submillisecond lifetimes.[52]

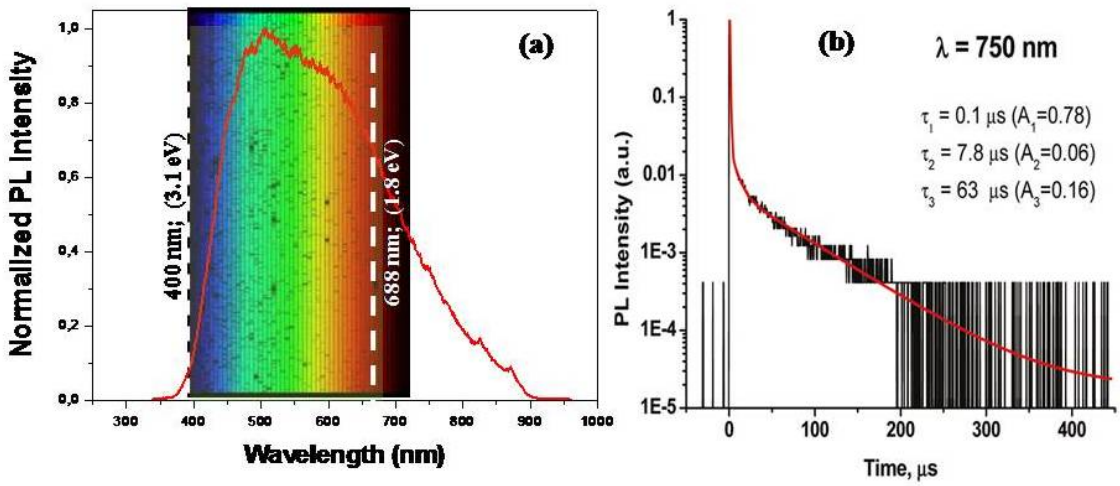

Figure 2.17: (a) PL spectrum of isopropanol suspension of Si NPs produced by nanosecond LA in chloroform. (b) The PL decay kinetics detected at λ_{reg}= 750 nm from Si NPs produced in chloroform (after post treatment). The blue-red shaded area corresponds to the PL spectral region of Si NCs passivated by chlorine.

As for the nature of the luminescence with a short lifetime (less than 100 ns, time resolution of the setup), we found that the relative intensity of the short-lived PL grows with time on the time scale of hours and days as a result of interaction with air that

suggests the Si-oxide origin of this PL, the more so as Si-O related PL is usually short lived (nanosecond time scale).[53] These assumptions about the origin of the two components of luminescence are in agreement with the PL behavior of Si NPs in the presence of hydrofluoric acid.

Indeed, HF removes silicon oxides that should result in the quenching of short-lived photoluminescence. On the other hand, replacement of the oxygen passivation of Si NCs that emit long-lived PL by hydrogen passivation in the presence of HF, should significantly change the PL properties. Indeed, unlike Si NPs passivated by oxygen, hydrogen-passivated Si NCs exhibit PL with nanosecond lifetimes, and this PL is usually observed in a different (blue-green) region.[54-55] In any case, the long-lived luminescence component belonging to oxygen-passivated Si NPs should be quenched in the presence of HF.

Finally, it is known from the literature that Si NCs passivated by chlorine show luminescence in the 1.8-3.1 eV spectral region,[56] which agrees very well with the region of the emission of our Si NPs (in our case chlorine atoms can be released from chloroform during the laser ablation). Therefore, the origin of the observed PL and its relation to the Si NC surface require further investigation.

2.4. Core-shell silicon-graphite nanoparticles and carbon nano-onions produced by PLAL of a Si target in organic liquids

The irradiation of a silicon target immersed in chloroform ($CHCl_3$) by nanosecond UV pulses during large time (60 min of minutes) results in the formation of a stable colloidal suspension with a brownish color.

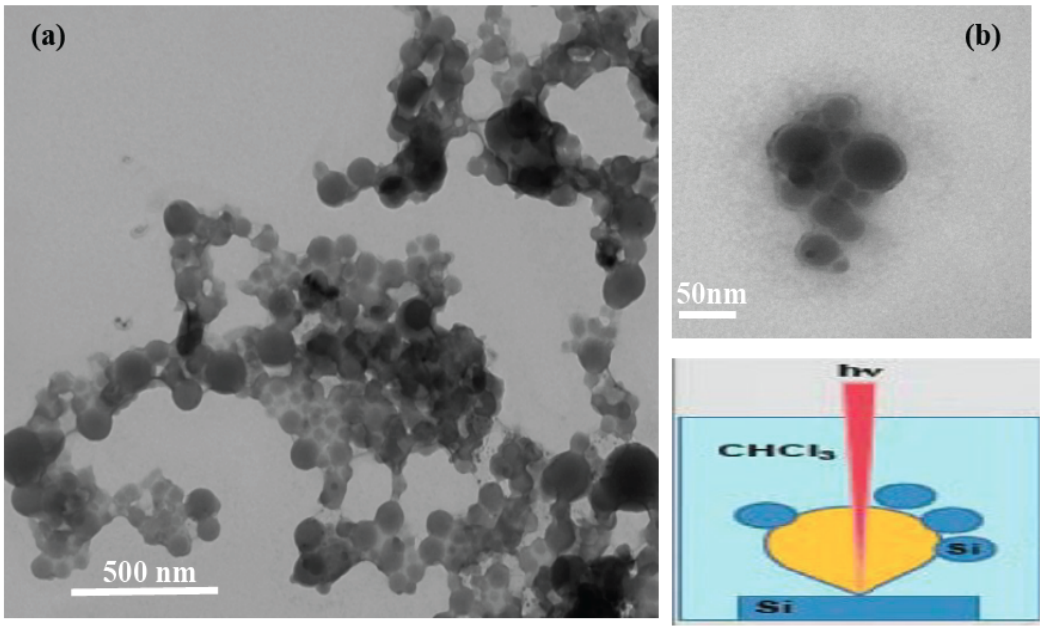

Figure 2.18: TEM micrographs of Silicon nanoparticles produced by long-time PLAL of silicon target in chloroform. Images (a) and (b) show two different grouping modes. In image (a) Si NPs form a wire-like structure.

Figure 2.18 shows a TEM micrograph of the sample collected on copper grid after evaporation of chloroform. The nanoparticles do not exhibit a serious agglomeration, but instead they tend to form (in drop cast layers) linear chains in which an amorphous "soup" glues Si NPs to each other (Figure 2.18(a)). As shown in Figure 2.18(b) some Si NPs seem to exhibit a core/shell structure.

Figure 2.19(a) shows the HRTEM micrograph of a part of one individual NP. The NP presents a policrystalline structure composed of mono-crystallites (separately analysed in Figures 2.19(b-d)) with mean diameters in the range 5–10 nm. The micrograph shows the coexistence of two types of mono-crystallites with lattice fringe spacing (indicated by parallel lines in Figures 2.19(b) and (d)) of 2.540Å (minor contribution) and 3.167Å (dominant), respectively.

These values agree well with the (111) lattice constants for silicon carbide and silicon, respectively, in standard diamond crystal structures. The selected area electron diffraction (SAED) analysis indicates the coexistence of a relatively weak ring corresponding to $SiC_{(2\ 0\ 0)}$ and $SiC_{(1\ 1\ 1)}$with the rings of $Si_{(1\ 1\ 1)}$, $Si_{(2\ 2\ 0)}$ and $Si_{(3\ 1\ 1)}$, as observed in Figure 2.19(e) that includes the assignment of such rings.

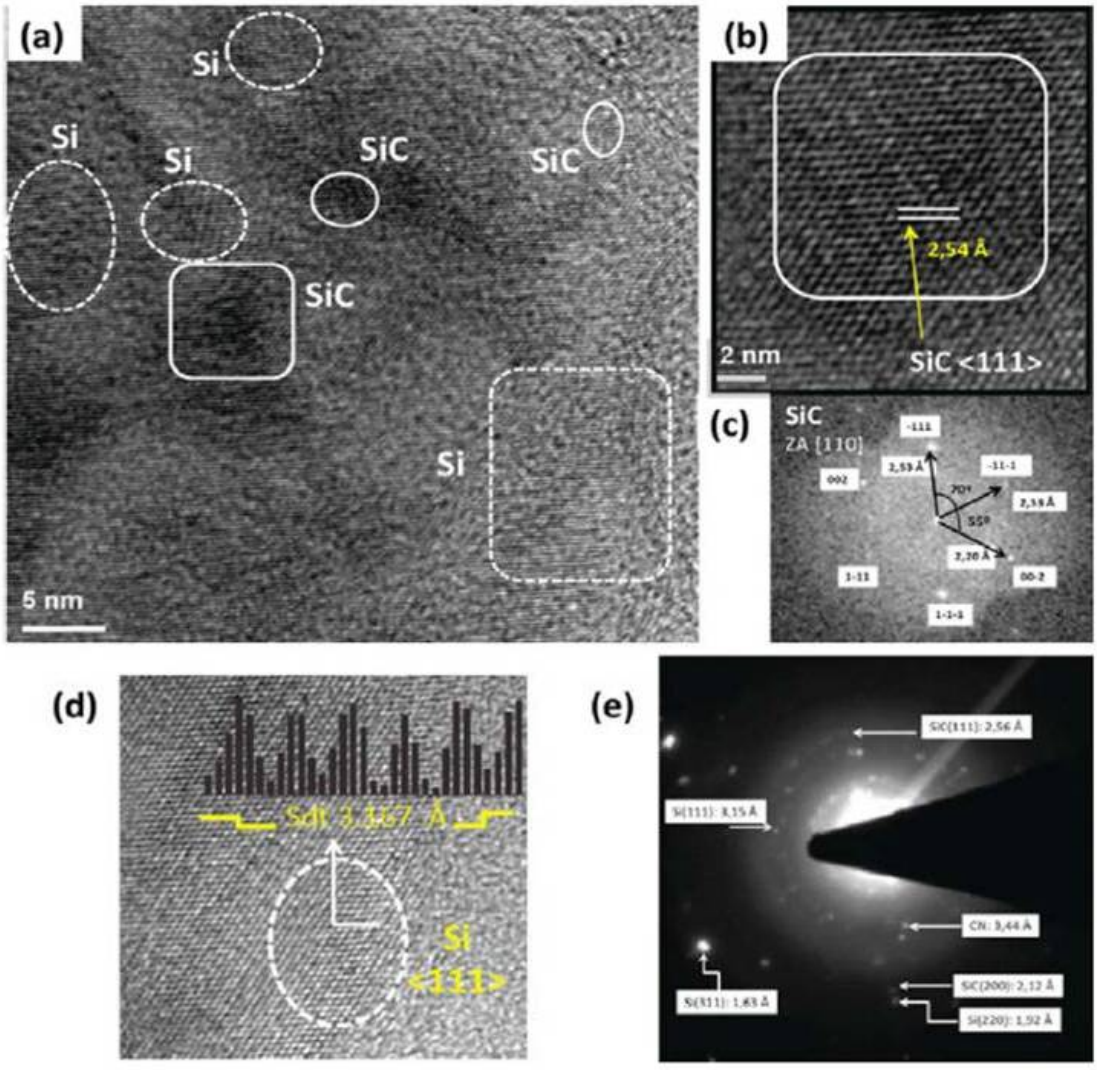

Figure 2.19: (a) HRTEM micrograph of a part of a single polycrystalline NP consisting of Si and SiC mono-crystallites, which are encircled by dashed and solid lines, respectively. A zoom of a SiC nanocrystallite is depicted in (b), together with its FFT analysis in (c). In (d) a zoom corresponding to a Si (111) nanocrystallite is presented including the details of the plane period (3.167 Å). Finally, the SAED pattern corresponding to the NP in micrograph (a) is included as (e).

Since FFT offers information about a small selected zone of the HRTEM image, the well defined spots in the FFT pattern, in comparison with SAED, evidence that the small NPs constituting a big polycrystalline NP possess the structure close to the mono-crystalline one.

As one can see in Figure 2.20(a), the surface of an individual Si NP obtained by PLAL in chloroform is coated with several layers of a material, the measured inter-plane spacing for which was ranging from 3.3 to 3.6 Å.

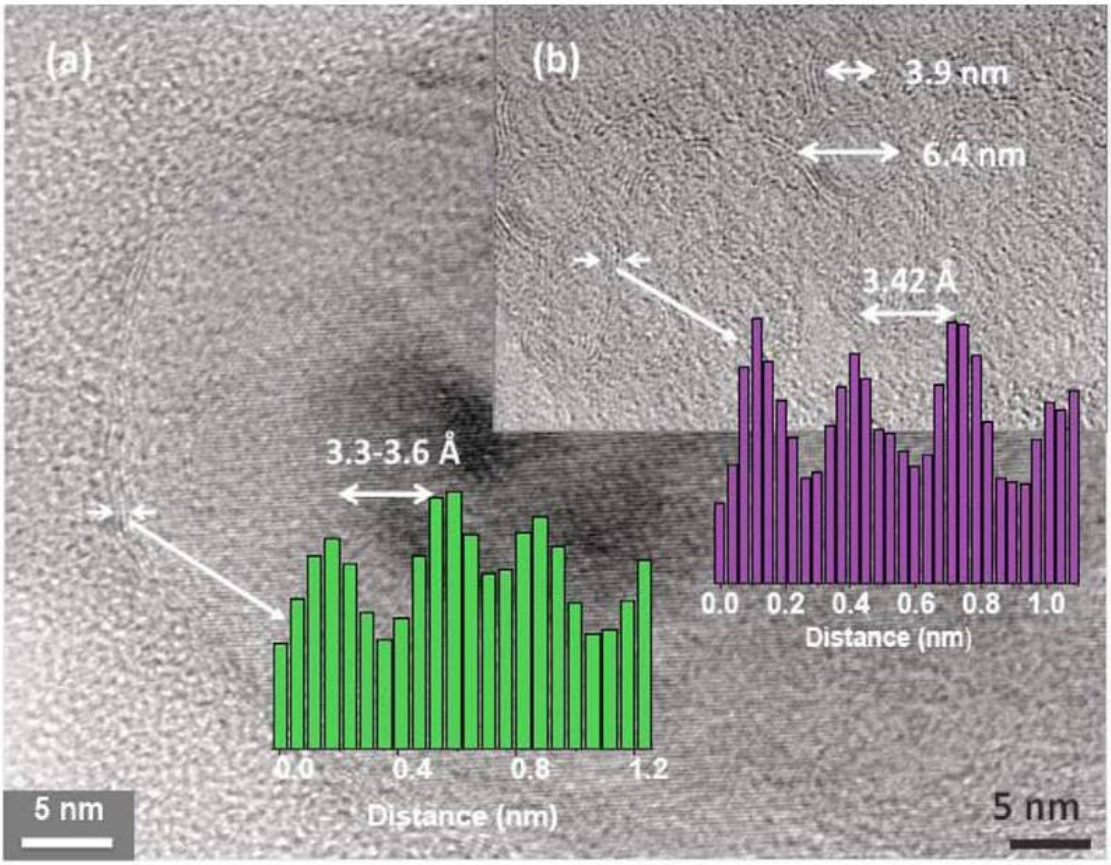

Figure 2.20: (a) HRTEM micrograph of a single polycrystalline NP covered by a multilayer carbon shell. (b) HRTEM image of carbon nano-onions (CNOs) detected in a space between the core–shell NPs. The results of the interlayer distance determination using the digital micrograph software are marked by green and blue colours for graphite and CNO, respectively.

It is known that the distance of 3.4Å is a characteristic of bulk graphite inter-plane spacing. We believe, therefore, that the multilayer structure observed in Figure 2.20(a) along the external border of the NP is a multilayer graphite shell formed, as we suggest,

due to decomposition of chloroform under the high-temperature conditions of the laser ablation (possible mechanisms will be discussed below).

We found that the graphite shells are not the exclusive carbon nanostructures formed during the PLAL experiments in chloroform. In addition, multilayer structures of another type, which are not connected to the polycrystalline Si NPs (Figure 2.20(a)), are observed in the space between them. These multilayer nanostructures demonstrate spherical or onion like shape with a diameter smaller than 10 nm (the size of some nanostructures is indicated by arrows in Figure 2.20(b)). At the same time, the distance between the layers in these nanostructures is the same as that in the case of graphite shells (3.4 Å) that evidences in favor of their carbon nature (carbon nano-onions (CNOs), or onion-like carbon (OLC).[57])

Therefore, NPs produced by UV ns PLAL of a Si target in chloroform possess three main peculiarities:

(i) They are polycrystalline and are composed mainly of Si monocrystallites with an inclusion of silicon carbide (SiC) monocrystallites.
(ii) The polycrystalline NPs are wrapped by a multilayer graphite shell.
(iii) A large number of free CNOs are also produced during the ablation process.

To check whether the absence of C–H group can change the efficiency of the graphitic shell formation or not, we used CCl_4 as a counterpart liquid for laser ablation experiments. Under the same ablation conditions that were used for the case of $CHCl_3$, in CCl_4 we did not observe the formation of multilayer shells around the silicon-based core. Thus, the observation evidences in favor of a crucial role of CH group (likely in the form of CH radicals) in the formation of laser-ablation-induced graphitic multilayer structures.

The XPS data confirm a significant difference in the degree of interaction of the Si NP surface with carbon products, formed due to liquid decomposition, in the case of $CHCl_3$ and CCl_4, as can be deduced from Si 2p and C 1s core-level bands from XPS spectra of Si (Figures 2.21(a) and 2.21 (b), respectively) in NPs produced by ns PLAL in chloroform (curves labeled as 1 in Figure 2.21(a)) and carbon tetrachloride (curves labeled as 2 in Figure 2.21(a)).

The Si 2p peak with the lowest binding energy (99.2 eV) appears to be detected only for NPs produced in CCl_4 (curve 1 in Figure 2.21(a)). The other two Si 2p peaks resolved at 101.4 and 103.7 eV are detected for Si NPs produced in both liquids (curves 1-2 in

Figure 2.21(a)). The first Si 2p peak (about ~99 eV) is usually attributed to non-oxidized Si atoms in the Si(0) state and the next Si 2p peak at~101 eV to Si atoms in the Si(2^+) state in a SiC, SiO_x or SiCl-like environment.[58-59] The Si 2p appearing at the highest binding energy (~103.5 eV) is related to Si atoms in a SiO_2-like environment. Therefore, the surface of Si NPs produced in CCl_4 is practically not functionalized by carbon or any other atoms. In the case of Si NP synthesis in $CHCl_3$, Si atoms in the Si(0) state are not observed at all on the Si NP surface. The Si 2p peak resolved at 101.4 eV can be assigned to the Si(2+) state and corresponds to SiC_x ,$SiCl_x$ or SiO_x environment.

In the spectra related to the C 1s core-level bands of Si NPs produced by PLAL in both liquids (Figure 2.21(b)) a lowest energy peak at 284.5 eV is observed that we attribute to C–C and/or SiC-like bonding. In addition to these peaks, two broad C 1s features appear at higher binding energies (286 - 288 eV) coming from C atoms bonded to more electronegative ones. These electronegative atoms would be expected to be O or Cl. In all cases the source of O atoms is the molecular oxygen, O_2, from air dissolved in the liquid.

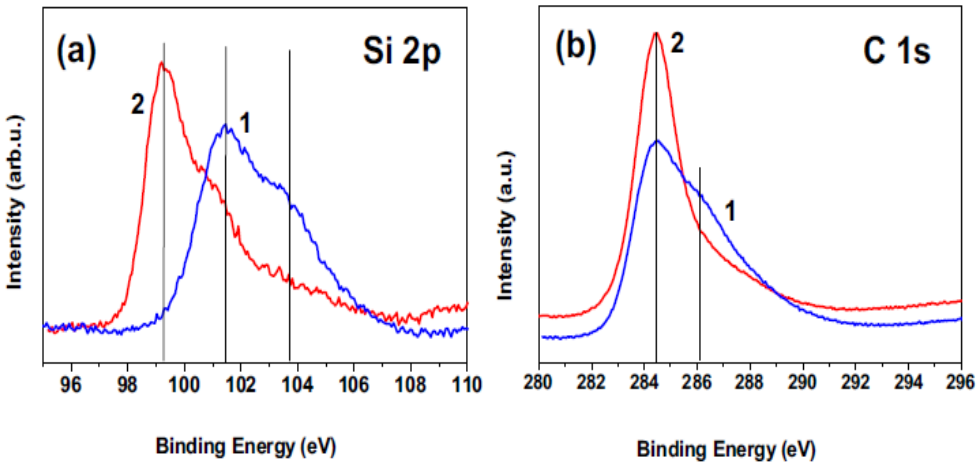

Figure 2.21: Si 2p (*a*) and C 1s (*b*) core-level bands from XPS spectra of Si NPs produced by ns PLAL in chloroform (1) and carbon tetrachloride (2).

The fact that big polycrystalline Si NPs rather than individual 5–10 nm mono-crystallites occur to be coated with a multilayer graphite shell suggests that the polycrystalline Si core forms first followed by carbon multilayer shell formation around the polycrystalline Si core. To confirm this, we carried out special experiments, in which laser ablation of a Si target in $CHCl_3$ was stopped after the first 60 s of pulsed laser irradiation and the ablation products were analyzed by HRTEM. It turned out that large

clusters of diameter about 50 nm and irregular shape are produced during this time, the clusters being composed of single crystalline NPs with a size of about 10 nm.

It is worth to note that the formation of any carbon layer and nanostructure is not observed at this initial stage of Si target ablation in chloroform. On the basis of this information we suggest that the transformation of these bare Si nanocrystal clusters of irregular shape into graphite-coated spherical NPs is caused by direct absorption of the excitation laser light by big Si clusters dispersed in the suspension and that the Si clusters serve as a template to form carbon multilayer structures. On the basis of the data obtained in this work as well as of the literature data,[60] we propose a mechanistic pathway for the formation of carbon multilayer structures around the polycrystalline Si NP core (see this work [61]) *as well as of free multilayer carbon nanostructures under laser ablation of the Si target in $CHCl_3$.*

Thus, the first stage of nanosecond laser ablation of a Si target in organic liquids consists in the formation and coalescence of initially produced Si/SiC clusters to form big Si/SiC NPs, which serve as templates for multilayer carbon nanostructure formation. When the NPs reach a sufficiently big size providing efficient light absorption to increase the NP surface temperature, the high temperature gives rise to two *activation* processes preceding the formation of the Si–C bonds registered by XPS. These processes are the activation of (i) the surface of a silicon NP, and (ii) organic liquid molecules near the Si NP surface (processes 1 and 2, respectively, in scheme 1).

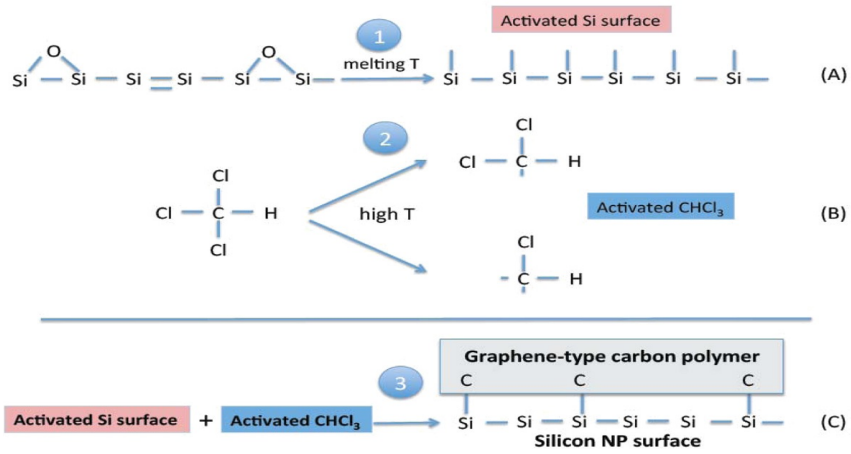

Scheme 1. Suggested mechanism of temperature-induced activation of Si NP surface (process 1) and $CHCl_3$ molecules (process 2) followed by their interaction (process 3) resulting in the formation of a polymeric carbon layer (graphene-type) on the Si surface.

It is worth noting that, in the case of the formation of carbon multilayer structures under ultrasound treatment of Si NPs/NWs [60], Si surface activation was achieved by preliminary etching of Si NPs/NWs with HF that gave rise to a hydrogen-terminated Si surface covered with SiH_x (where x = 1–3) species. It was the crucial step because little or no carbon multilayer material was formed on top of Si templates under ultrasound treatment of the as-prepared (that is oxidized) Si NPs/NWs.[60] Under the extreme local temperature within the acoustic cavity the Si-H bond breaks forming a net of extremely reactive Si dangling bonds, which react with the activated molecules of the liquid. We believe that in the case of laser ablation, the excitation light absorption by big Si NPs in a suspension can ensure activation of the Si NP surface without preliminary surface hydrogenation. It can occur because light absorption by big Si NPs increases the NP surface temperature sufficiently to melt the surface that results in (i) the formation of Si dangling bonds on the surface, and (ii) laser-annealing-induced removal of foreign atoms (such as oxygen) from the near-surface region.[62] As an indirect manifestation of the fusion process we can mention the acquisition of more spherical shape by polycrystalline Si NPs during the process of graphitic shell formation as compared with the angular shapes observed at the beginning of the ablation process.[61] Concerning the temperature, which can be achieved on and near the surface of polycrystalline Si NPs due to the absorption of excitation light, we evaluate it qualitatively to be as high as at least about 1500–2000 K. In fact, the polycrystalline Si NP round shape reveals Si NP surface melting as a result of the transformation of the energy of absorbed photons to heat (light absorption efficiency of silicon NPs is very high in the UV region [64-63]). On the other hand, the melting temperature for Si NPs is between ≈1000 and ≈1700K (bulk Si melting temperature) depending on the Si NP size. [65] Finally, direct measurements carried out for the case of Si surface ablation in inert gas and O_2 atmospheres at excitation energies (1.5 J cm^{-2}) similar to those used in our experiments (≈40 J cm^{-2}) showed that the temperature of hot Si atoms and SiO molecules is about 2000K for at least 5μs after ns laser excitation.[66]

The dangling bonds are rather short-lived species and will react with any suitable counterparts (dissolved molecular oxygen or chlorine atoms formed due to $CHCl_3$ destruction) if they do not meet activated carbon-containing molecules to form Si–C bonds.

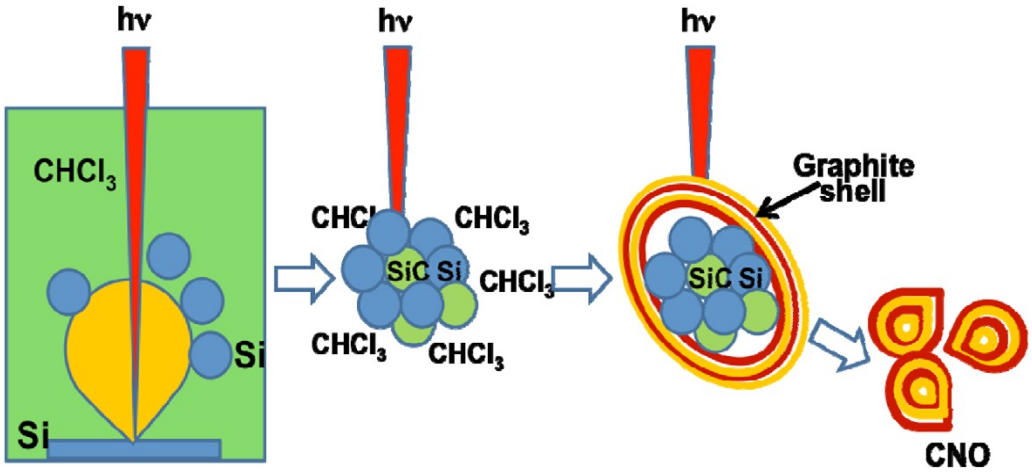

Scheme 2. Diagram illustrating the formation of Si/SiC NPs, graphitic shells around Si/SiC NPs and free CNOs as a result of long-time silicon target ablation in $CHCl_3$.

We believe that Si NP heating by laser pulses ensures not only an activation of Si surface by formation of Si dangling bonds, but also, due to a local surrounding temperature increase, an activation of $CHCl_3$ molecules contacting the surface. This temperature increase will initiate $CHCl_3$ dechlorination (because bond dissociation energy is lower for C–Cl as compared with C–H) with formation of chemically active $CHCl_2$– and CHCl= radicals (the activation process 2 in scheme 1). Importance of these radicals in the formation of graphitic multilayer structures around Si NPs is evidenced by the experimental observations: halogen-free hydrocarbons and hydrogen-free CCl_4 produce little, if any, multilayer carbon nanostructures. [67-60]

Thus, we suggest that under the conditions of laser ablation in chloroform, similarly to the case of ultrasonic treatment of chloroform in the presence of dispersed Si nanostructures [60], the hydrocarbon layers (hydrogenized graphite) should initially be formed around Si NPs, the hydrocarbon layers then being transformed into carbon layers as a result of de-hydrogenation due to further action of high temperatures and high pressures. However, this intermediate stage of chloroform carbonization at which hydrocarbon layers are formed on the surface of the Si polycrystalline NPs is not observed in our TEM measurements, probably because this stage is very fast so that the initially formed hydrocarbon layers efficiently lose hydrogen forming more dense carbon layers. As far as the formation of CNO is concerned, we suggest that this is a secondary process, which is based on the shedding off multilayer graphitic shells formed around the Si NP core. Schematically the suggested pathways of the formation of graphitic shells around Si NPs and free CNOs as a result of silicon target ablation in $CHCl_3$ are shown in

scheme 2. In the mechanistic pathway proposed in this work to describe the formation of graphitic shells (scheme 1) the specific role of CH radicals needs to be investigated in more detail.

2.5. Metal Nanoparticles produced by physicochemical PLAL

Metal nanoparticles (NPs) has attracted much attention due to their electronic and optical properties.[69-68] Many aspects of these optical properties (Localized Surface Plasmon Resonance -LSPR- and Surface Enhanced Raman Scattering -SERS-) and applications (biosensing and single molecule detection) have been reported during the last years.[71-70] Of particular interest is their use in biological labelling and photo-thermal cancer nano-therapy.[72] For such applications it is important to control the size and shape of the NPs,[73] as well as their toxicity.

In this part we describe a simple and powerful technique based on laser ablation of a target immersed in a water solution of a metal salt.[74] With this method nanoparticles of different metals and alloys can be processed very fast. Both the target and the salt solution can be chosen to produce metal nanoparticles of different sizes, surface oxidized nanoparticles (silica-silver, for example) or even more complex structures to be defined by the researcher on one or more steps, because the technique combine the advantages of both physical and chemical methods. We have applied this technique to the fabrication of inert silica-metal (silver, gold and silver-gold (alloy)) nanoparticles with a strong Surface Plasmon Resonance (SPR) all together in a single step. The advantage of the simultaneous production of silica during the metallic nanoparticle production by laser ablation is the stabilisation of the colloid, but also the possibility to obtain metal nanoparticles with good functionalization capabilities.

This method combines the advantages of chemical synthesis and cleaning, with the versatility of the laser ablation technique. In fact, the high yield and fast processing time exhibited by our method is very promising for scalable production of NPs. In addition, in order to influence the size and morphology of the NPs in the (liquid) laser ablation method we can play with the most important variables of the process, such as metallic salts concentration, power density and target material. The chemical characteristics and colloid environment of the NPs can also be independently determined by selecting the target materials.

This physical-chemical method is based on the laser ablation of a solid target immersed in a water solution of a metal salt, as reported in Ref.[75] The local high temperatures and pressures reached during the laser ablation, together with the oxidation of the ablated material, lead to the formation of complex metal-oxide nanoparticles directly into a stable colloid. This is attributed to the simultaneous production of amorphous silicon dioxide nanoparticles (stabilizing agent for the forming colloid) during the ablation of the silicon target, as corroborated by X-ray microanalysis. Spherical and ellipsoidal metal-oxide nanocrystals are mainly obtained in the first second.

The laser used for ablation in the experiments described in this part is the third harmonic (λ =355 nm) of a Q-switch Nd:YVO_4 UV laser, giving pulses of 40 ns duration at the repetition rate of 5 kHz. The laser power densities per pulse on the target surface were always below 40 $J.cm^{-2}$ (1 W of average power). Several targets such as silicon, germanium, and tungsten with a purity of 99.99% were placed and fixed at the bottom of a glass vessel containing 20 ml of $AgNO_3$ ($HAuCl_4$ or a mixture of both salts) in a water solution in order to produce silver (gold and a silver-gold alloy) NPs.

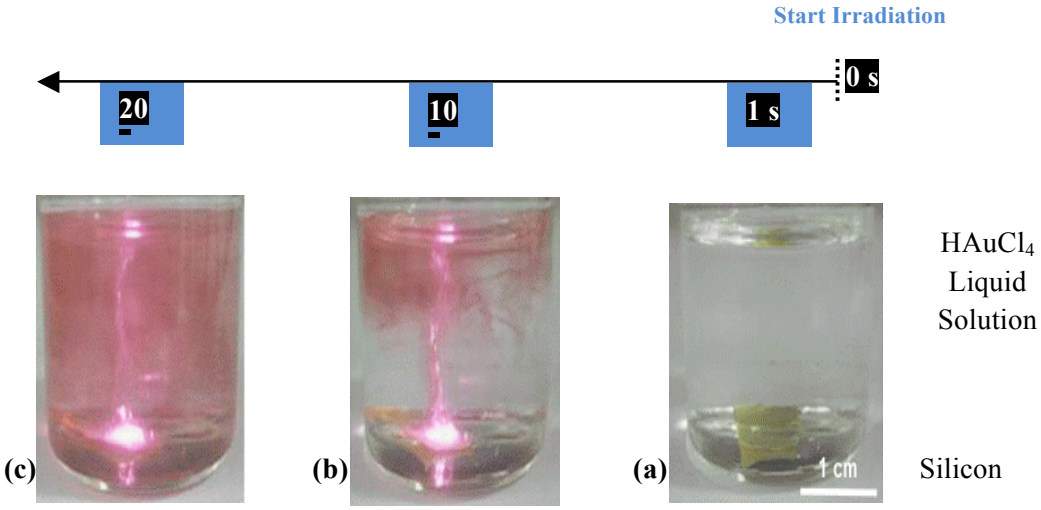

Figure 2.22. Illustration of the laser ablation of a silicon target in a water solution of $HAuCl_4$.[74] From (a) to (c) the irradiation times is increased from 1 to 20 s.

Our method should be useful to develop surface chemistry under extremely non equilibrium conditions. In this way we have developed the synthesis of silver (gold) NPs by using the appropriate salt precursor, $AgNO_3$ ($HAuCl_4$), maintaining constant the other experimental conditions. The gold (silver) colloid exhibits the typical colour after some seconds of PLAL, as observed in Figure 2.22(a-c), and hence the characteristic spectrum

of the Surface Plasmon Resonance (SPR) at around 535 (400) nm, as shown in Figure 2.23(b).

More important is the capability of our method to realize many other single-metal and complex nanoparticles by changing and/or mixing metal salt precursors, as shown for the case of Ag-Au NP colloid presented in Figure 2.23. This complex colloid has been prepared by using the $AgNO_3$:$HAuCl_4$ concentration ratio of 4:1 with $AgNO_3$ concentration equal to that used for pure Ag NPs preparation.

The crystal structure of nanoparticles was examined by HRTEM revealing the presence of amorphous SiO_2, which is mostly concentrated as a shell around the NPs (see Figure 2.24). The SiO_2 shell can arise from a fast oxidation of the sputtered silicon of the ablated target, due to the high local temperatures that can be reached around the target surface. Pure metal (Ag or Au) and alloy (Ag-Au) NPs have very similar crystalline characteristics: typically multiple twin planes are observed in HRTEM images.

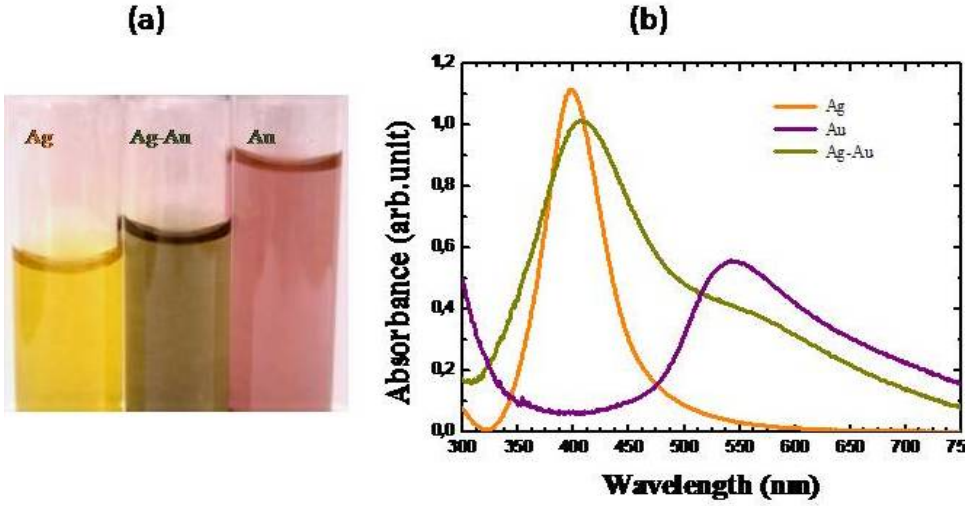

Figure 2.23: (a) Picture and (b) absorbance spectra of the colloids obtained after the single step synthesis developed in the present work under similar conditions, but using different metal salt precursors (indicated in the plot).

Furthermore, silica can be also present in the colloid solution, as demonstrated by chemical mapping TEM (Figure 2.24(a-d)) and EDX performed on drop cast films. The small size attributed to silica NPs should be a consequence of the fast exothermic combustion reaction of Si NPs being produced during the laser ablation process, leading to their fragmentation and oxidation. A possible redox reaction, taking place during the ablation process in order to produce silica and metal NPs, can be written as follows:

$$Si_{(NP)} + 4\,AgNO_3 + 2H_2O \longrightarrow SiO_{2\,(NP)} + 4Ag_{(NP)} + 4H^+ + 4NO^-_3$$

Another relevant parameter during the laser-assisted synthesis of Ag nanoparticles is the laser irradiation time (LIT). As shown in Figure 2.25(a), the increase of the absorbance with the LIT is strongly sub-linear, and when LIT is more than 528 s the intensity of the LSPR decreases and the band broadens in accordance with the exhaustion of the metal salt. The initial blue shift of the LSPR when LIT increases could be associated to the increase of silica nanoparticles in a greater proportion than silver ones, improving the stability of the colloid and reducing the coalescence between metal nanoparticles, as compared to the case of high LIT exhibiting a clear broadening of the LSPR from the long wavelengths side.

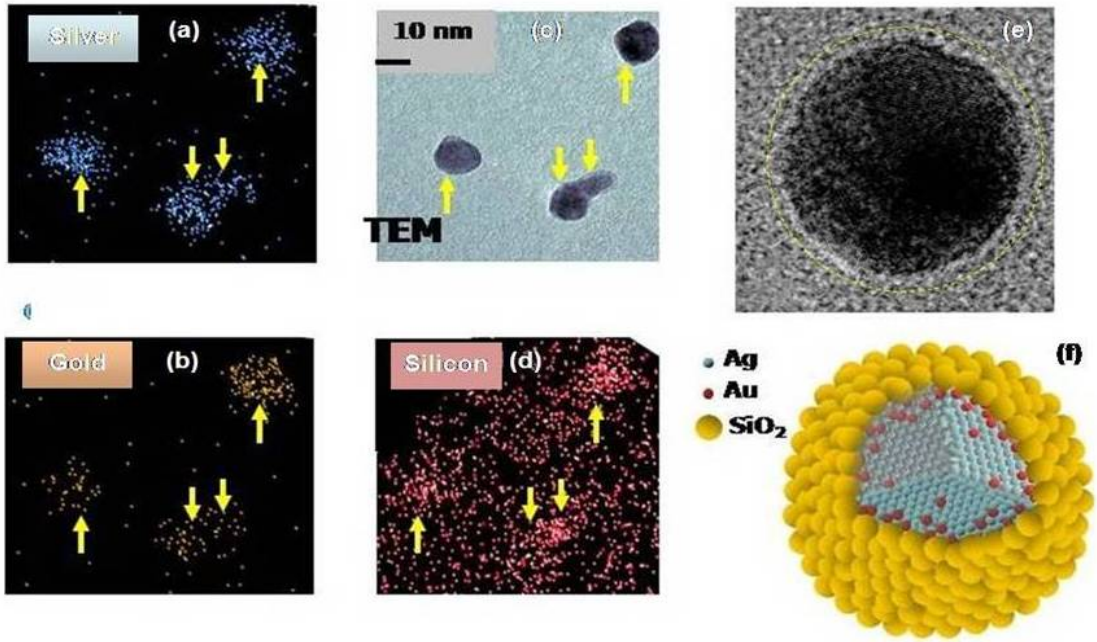

Figure 2.24: EDX-HRTEM chemical mapping images of silver-gold alloy NPs demonstrate the presence of (a) silver and (b) gold in the four NPs marked by yellow arrows and observed in (c) the real-space TEM image. (d) Other than silver and gold, the EDX-HRTEM also reveals the presence of silicon, but it is more concentrated around the NPs. The silicon (from ejected material during ablation) is found to be in the form of amorphous SiO_2 (e), as illustrated in panel (f). The presence of stoichiometric SiO_2 in all colloids is also corroborated from EDX microanalysis performed by SEM on a drop cast sample prepared on a GaAs substrate.

Figure 2.25(b) shows UV-VIS absorbance spectra corresponding to several colloids prepared for different $AgNO_3$ concentrations in water (under a constant average laser power densities per pulse on the target surface of 40 $J.cm^{-2}$ and the same irradiation time (264 s)). The main influence of the $AgNO_3$ concentration is the modification of the Localised SPR peak intensity and width. The LSPR amplitude increases with the metal

salt concentration up to a maximum for $1.25x10^{-4}$ M. Above this concentration the LSPR intensity decreases and the resonance band broadens significantly.

The increase of the salt concentration and hence of the density of NPs obtained in the colloid produces two negative effects:

(i) Increase of the light absorption and scattering by the NPs being produced earlier that reduces the effective laser power density at the target surface.

(ii) Increase of the proportion of NPs adhered to big Si particles due to the increase of the colloid density.

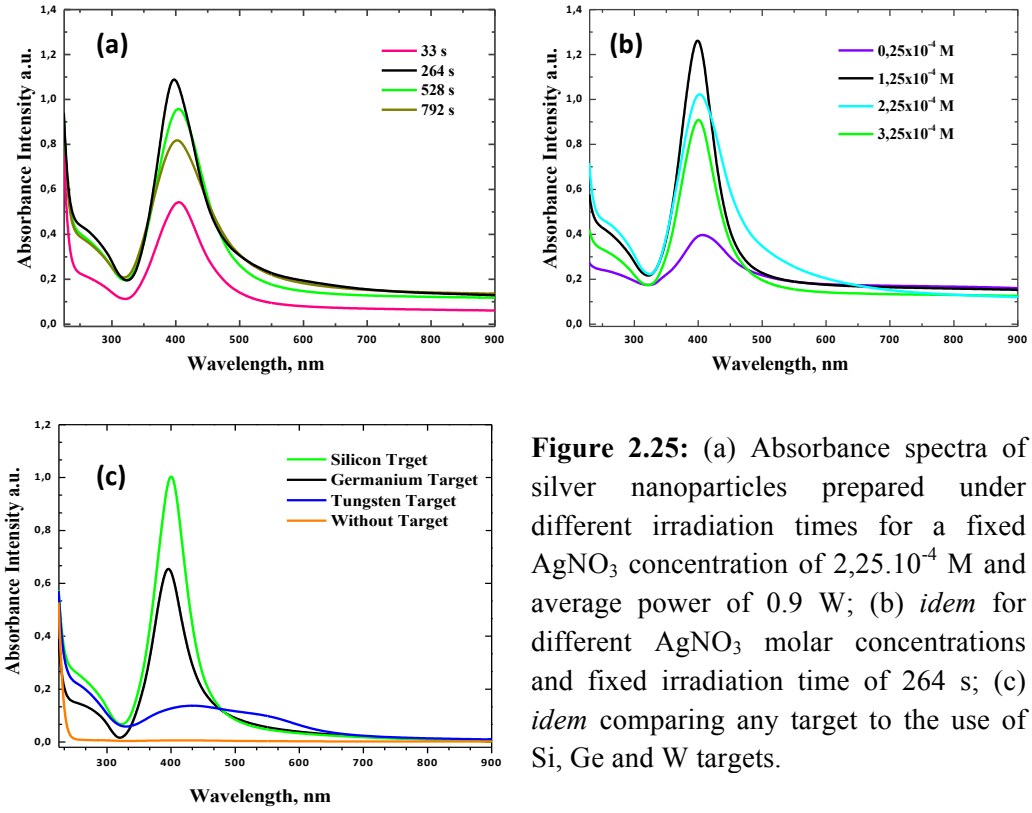

Figure 2.25: (a) Absorbance spectra of silver nanoparticles prepared under different irradiation times for a fixed $AgNO_3$ concentration of $2{,}25.10^{-4}$ M and average power of 0.9 W; (b) *idem* for different $AgNO_3$ molar concentrations and fixed irradiation time of 264 s; (c) *idem* comparing any target to the use of Si, Ge and W targets.

Along with the liquid environment, the metal salt type and the laser properties, another important parameter is the target used in our laser ablation method. Both physical and chemical properties of the target can influence the nanoparticle composition and the colloid stability.[76] In this way we expect different efficiencies in the synthesis of obtained Ag-NPs and even differences in the physical properties of the NPs and colloids,

as shown in Figures 2.25(c) and 2.26. These results show that silver nanoparticles are produced by using different targets, but the size, composition and PLAL efficiency may depend strictly on the physical and chemical properties of solid target.

The XRD spectra of Ag and Au nanoparticles exhibit diffraction peaks associated to FCC crystalline planes (111), (200), (220) and (311). The observation of these diffracting planes can indicate a certain faceting of the NPs, as can be directly seen for some of them at the HRTEM images. For the formation of the nanocrystals, including metastable phases, upon laser ablation of a given target immersed in liquid, a number of factors should be taken into account, mainly the laser parameters and the chemical properties of the liquid.

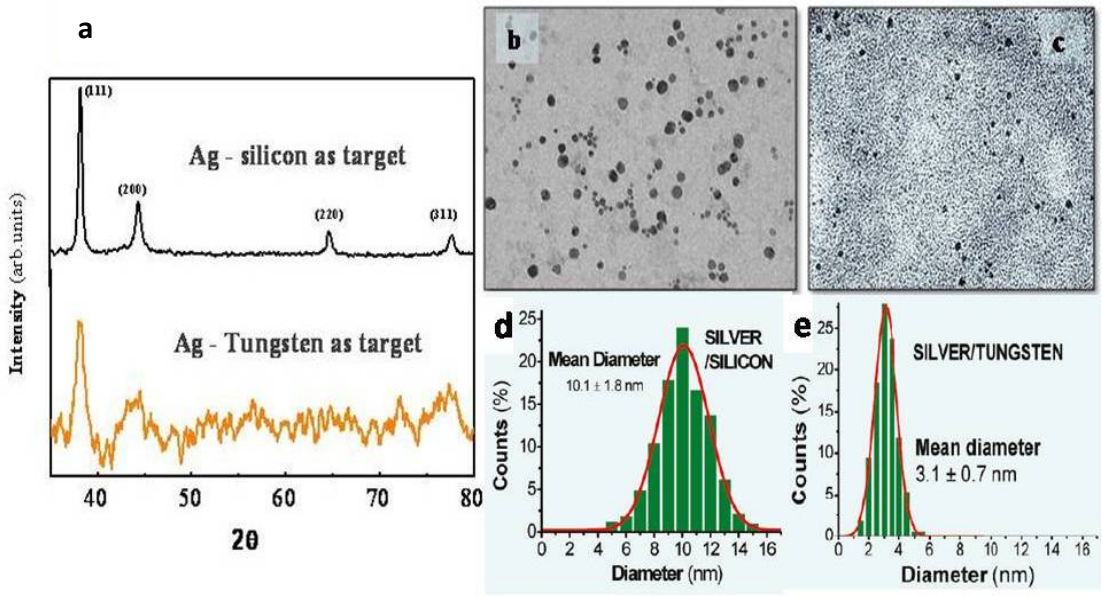

Figure 2.26: (a) X-Ray Diffraction spectra measured in drop cast layers of Ag –NPs produced with Tungsten (yellow line) and Si (black line) targets maintaining equal all the other parameters and conditions. TEM micrographs of these Ag – NPs and their corresponding size histograms produced by using Si (b - d) and Tungsten (c - e) targets.

On the other hand, we clearly obtain that the size of Ag NPs by using a tungsten target is smaller than those produced by using a silicon target, which is consistent with TEM micrographs in Figure 2.26(b-c). Silver NPs in the colloid produced by using a Si target have a diameter around 11 nm, that is, near 4 times bigger than those obtained by using a W target.

The observed differences between the plasmonic absorption bands of the three colloids obtained with ablation of different targets (Silicon -Tungsten-Germanium, see Figure 2.25(c)) can be attributed to the different boiling point and reactivity of the target materials ablated during the process.

Upon laser irradiation, evaporation of targets occurs reducing the limit temperature reached at the target surface during ablation. It is a well-known fact that the lower boiling temperature of a target the higher material evaporation. The laser ablation of silicon leads to the formation of Si NPs.[78-77] Because Si NPs are expected to be very reactive, it immediately oxidizes to SiO_2 in water at high temperatures[80-79]and pressure.[80] The oxidation of silicon provokes the reduction of Ag(I) to Ag.

If, instead of Si, we irradiate a Ge target, the material evaporation is more massive (higher amount of Ge particles) and local temperatures around the irradiation area are slightly higher than the case of Si. This is because Ge has a lower boiling point, 2830 ºC, and a higher absorption coefficient at 355 nm. At the same time, Ge also passivates to GeO_2, but not as much as occur in case of Si. These small differences can affect the amount of Ag NPs in the colloid, but no relevant changes are expected in the average size of the NPs and the colloid stability

In case of W (Tungsten) the boiling point is 5550 ºC. In this way we would expect that nanoparticle synthesis could take place at a high temperature and hence a capability to reduce Ag(I) faster is available. However, the amount of the evaporated tungsten is small, that affects negatively to the colloid stability. Moreover, we observed a weak formation of by-products on the surface of the tungsten target, that may obviously affect the laser-target interaction.

However, the absence or a negligible amount of a stabilizing agent such as SiO_2 or GeO_2, due to the weak evaporation of tungsten, will favour the agglomeration of NPs. Now we can undoubtedly say that the origin of the red-LSPR component (545 nm) measured for the colloids obtained with the W target is attributed to nanoparticle agglomeration due to the electrostatic interaction. On the contrary, silver NPs made with silicon and germanium targets are more stable and characterized by narrow LSPR spectra during many days.

As aforementioned, alloyed nanoparticles can be obtained by performing laser ablation of a silicon target in a water solution containing mixtures of $AgNO_3$ and $HAuCl_4$ metal

salts. These colloids are stable and exhibit a colour that changes from yellow (pure Ag NPs) to magenta (pure Au NPs), as shown in Figure 2.27 from left to right. Consequently, the LSPR peak wavelength shifts from 400 to 520 nm for pure silver and gold colloids, respectively, and intermediate LSPR peak wavelengths for the different alloys with Au percentages above 30%, as observed in Figure 2.28(a). These intermediate LSPR peak wavelengths would confirm that disordered Ag-Au alloys are formed in these nanoparticles.

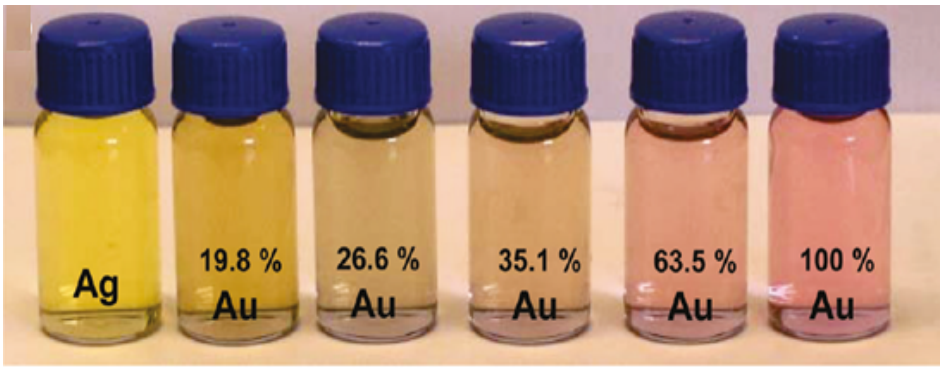

Figure 2.27: Photograph of the metal nanoparticle colloids obtained by this ablation method, from pure silver (left) to pure gold (right) and several Ag-Au alloys.

The process giving rise to Ag-Au alloy NPs differs from standard chemical synthesis, and it has been studied in more detail. On one side, we have measured the average content of Au inside the NPs of every colloid by EDX measurements. On the other side, we have obtained the average size of the Ag-Au NPs from TEM analysis (images and size histograms shown in Figure 2.29) as a function of the Au content in the salt solution, as shown in inset of Figure 2.28(a). The EDX analysis shows that the incorporation of Au atoms from the solution is 1:1, whereas it tends toward 3:1 at very low concentrations (Figure 2.28(b)). This is surely the reason why the diameter of the NPs decreases in the concentration range of 0-30% with respect to the value found for pure Ag (inset of Figure 2.28(a)). When adding small quantities of Au salt to the liquid solution for ablation, each Au(III) atom substitutes up to three Ag(I) atoms at the nanoparticle, which is initially formed with pure Ag when the Au salt concentration tends toward zero. This substitution mechanism would explain the reduction of the size due to the decrease in the total number of atoms at the nanoparticle.

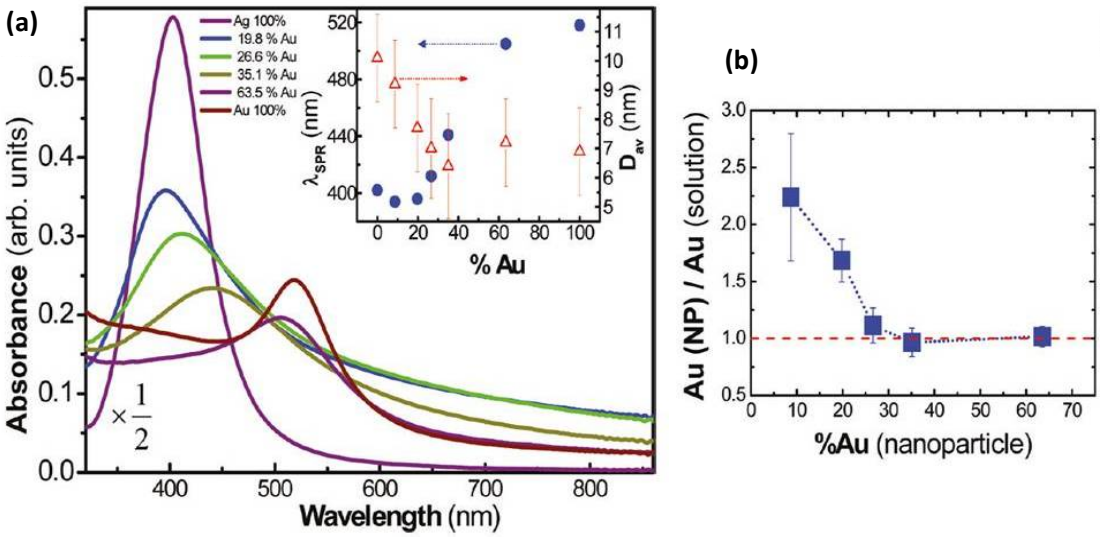

Figure 2.28: (a) A noticeable red shift is observed in the LSPR absorbance spectrum of the Ag-Au nanoparticle colloid when increasing the Au content in the alloy, except below 20% Au content, where a small blue shift is observed because of a change in the NP size (as measured by TEM; see Figure 2.29). (b) Ratio of the gold content in the NP (gold reduction measured by EDX microanalysis) with respect to that in the salt solution, represented as a function of the first quantity. The error in the measurement of % Au(NP) by the EDX microanalysis method is around 4%, approximately the size of the symbols in the inset of (a) and (b).

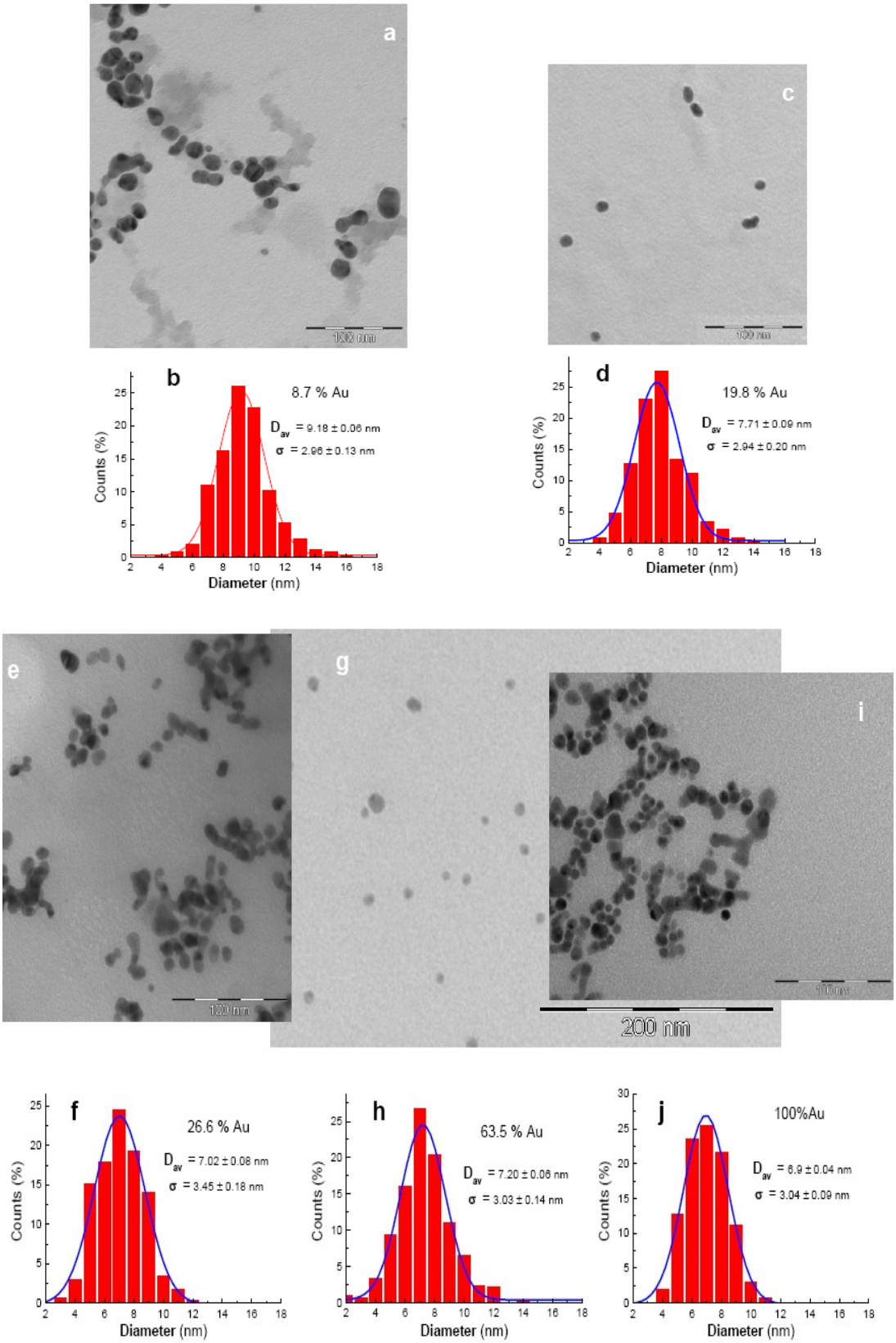

Figure 2.29: TEM images (a, c, e, g, i) and their corresponding size distribution histograms (b, d, f, h, j) of Ag-Au nanoparticles with different Au content: 8.7% (a-b), 19.8 % (c-d), 26.6 % (e-f), 63.5 % (g-h) and pure Au (i-j).

2.6. References to Chapter 2

1. T. H. Maiman, *Nature* **187**, 493 (1960).

2. S. Amoruso, R. Bruzzese, N. Spinelli, R. Velotta, M. Vitiello, X. Wang, G. Ausanio, V. Iannotti, and L. Lanotte, *Appl. Phys. Lett.***84**, 4502 (2004).

3. F. Hillenkamp, M. Karas, *Int. J. Mass Spectrom* **200**, 71 (2000).

4. I. A. Boyd,"*Photochemical Processing of Electronic Materials*", Academic Press London (1992).

5. D. B. Chrisey and G. K. Hubler, "*Pulsed Laser Deposition of thin films*", *Wiley-Interscience,* New York (1994).

6. A. G. Azema and L. D. Laude, "*Excimer Lasers*"; *Kluwer Academic Publishers*: Dordrecht (1994).

7. S. Georgiou, V. Zafiropulos, D. Anglos, C. Balas, V. Tornari and C. Fotakis, *Appl. Surf. Sci.* **127**, 738 (1998).

8. R.W. Eason, "*Pulsed Laser Deposition of Thin Films: Applications - Led Growth of Functional Materials*", *Wiley, New York* (2006).

9. T. Donnelly, B. Doggett and J. G. Lunney, *Appl. Surf. Sci*. **252**, 4445 (2006).

10. J. C. Miller and R. F. Haglund, "*Laser ablation mechanisms and applications*", Berlin: Springer-Verlag (1991).

11. E. Fogarassy and S. Lazare, *"Laser ablation of electronic materials basic mechanisms and applications*", *Amsterdam: Elsevier* (1992).

12. S. I. Anisimov, B. L. Kapeliovivh and T. L. Perelman, *Sov. Phys. JETP.* **39**, 375 (1974).

13. S. S. Mao, X. Mao, R. Greif and R. E. Russo, *Appl. Phys. Lett.* **76**, 31 (2000).

14. R. Kelly and A. Miotello "*Pulsed Laser Deposition of Thin Films*", *New York: John Wiley and Sons,* (1994).

15. G.W. Yang, *Progress in Materials Science* **52,** 648 (2007).

16. E. T. Itina, *J. Phys. Chem. C* **115,** 5044 (2011).

17. D. Devaux, R. Fabbro, L. Tollier and E. Bartnicki, *J .Appl. Phys.* **74,** 2268 (1993).

18. a) A. Sollier, L. Berthe and R. Fabbro, *EurPhys J. Appl. Phys*. **16**, 131 (2001); b) L. Berthe, A. Sollier, R. Fabbro, P. Peyer and E. Bartnicki*, J. Phys. D: Appl. Phys.* **33**, 2142 (2000).

19. T. Sakka, S. Iwanaga, Y. Ogata, A. Matsunawa and T. Takemoto, *J. Chem. Phys.* **112**, 8645 (2000)

20. Y.F. Lu, S.M.Huang, X.B. Wang and Z. X. Shen, *Appl. Phys. A*. **66,** 543 (1988).

21. W. Inoue, M. Okoshi and N. Inoue, *Appl. Phys. A*. **79**, 1457 (2004).

22. H. Zeng, X. W. Du, S. C. Singh , S.A. Kulinich, S. Yang, J. He and W. Cai, *Adv. Funct. Materials* **22**, 1333 (2012).

23. E. Leveugle and L. V. Zhigilei, *Appl. Phys. A* **79**, 753 (2004).

24. J. Hermann, S. Nöel, T. E.Itina, E. Axente and M. E. Povarnitsyn, *Laser Phys.* **18**, 374 (2008).

25. A. Mendes-Manjon, B. N. Chichkov and S. Barcikowski, *J. Phys .Chem. C* **114**, 2499 (2010).

26. a) P. V. Kamat, M. Flumiani and G. V. Hartland, *J. Phys. Chem. B* **102**, 3123 (1998); b) H. Fujiwara, S. Yanagida and P. V. Kamat, *J. Phys. Chem. B* **103**, 2589 (1999).

27. H. Muto, K. Miyajima and F. Mafune, *J. Phys. Chem. C* **112**, 5810 (2008).

28. D. Werner and S. Hashimoto, *J. Phys. Chem. C* **115**, 5063 (2011).

29. A. Pyatenko, M. Yamaguchi and M. Suzuki, *J. Phys. Chem. C* **113**, 9078(2009).

30. S. J. Shaw, W. P. Schiffers, T. P. Gentry and D. C. Emmony, *J. Phys. D* **32**, 1612 (1999).

31. R. Egerton, "*Physical principles of electron microscopy*". Springer (2005).

32. D. Williams and C. B Carter, "*Transmission Electron Microscopy. 1– Basics*". Plenum Press (1996).

33. B. Fultz and J. M.Howe, "*Transmission Electron Microscopy and Diffractometry of Materials*", 2nd ed*.; New York: Springer* (2002).

34. S. Hüfner, "*Photoelectron spectroscopy: principles and applications*", *Springer-Verlag* (1995).

35. B. V. Crist, "*Handbooks of Monochromatic XPS Spectra*" - Fully Annotated, PDF of Volumes 1 and 2, published by *XPS International LLC*, Mountain View (2005).

36. "*Handbook of The Elements and Native Oxides*", XPS *International, Inc. Retrieved* 8 December (2012).

37. Y. Waseda, E.Matsubara and K. Shinoda "*X-Ray Diffraction Crystallography: Introduction, Examples*" ISBN 3642166350, 9783642166358 springer (2011).

38. B.D. Cullity, "*Elements of X-ray Diffraction*", Addison-Wesley (1956).

39. R. John and S. S. Florence, *Chalcogenide Lett*. **6**, 535 (2009).

40. B.J. Clark "*UV Spectroscopy: Techniques, Instrumentation and Data Handling*", *London: Chapman & Hall* (1993).

41. D. A. Skoog, F. J. James, and S. R. Crouch, "*Principles of Instrumental Analysis*", 6th ed. Thomson Learning (2007).

42. S. S. Challa, R. Kumar "*UV-VIS and Photoluminescence Spectroscopy for Nanomaterials Characterization*", *Springer* (2013).

43. W. Stöber, A. Fink, and E. Bohn. *J. Coll. Inte. Sci.* **26**, 62 (1968).

44. S.T .Selvan, C.Li, M. Ando, and N. Murase, *Chem. Lett.* **33**, 4 (2004).

45. M. T. Harris, R. R. Brunson, and C. H. Byers, *J. Non-Cryst. Solids* **121**, 397 (1990).

46. J. Nayak , R. Mythili, M.Vijayalakashmi, and S.N Sahu, *Physica E.* **24**, 227 (2004).

47. E. Nelson, J. Woicik, and P. Pianetta, *J. Synchrotron Rad*. **6**, 341 (1999).

48. M. H. Tsai, P. Shen, and S.Y. Chen, *J. Europ. Cer. Soc.* **28**, 1631 (2008).

49. (a) J. Zi, K. Zhang and X. Xie, *Phys. Rev. B*. **55**, 9263 (1997); (b) V. Paillard, P. Puech, M. A. Laguna, R. Carles, B. Kohn, and F. Huisken, *J. Appl. Phys*. **86**, 1921 (1999).

50. N. Maley, D. Beeman and J.S. Lannin, *Phys. Rev. B.* **38**, 10611 (1988).

51. M. S. Hybertsen, *Phys. Rev. Lett*. **72**, 1514 (1994).

52. W.Wilson, P.Szajovsky and L. Brus, *Science* **262**, 1242. (1993).

53. K. S. Min, K. V. Shcheglov, C. M. Yang, H. A. Atwater, M. L. Brongersma and A. Polman, *Appl. Phys. Lett.* **69**, 2033 (1996).

54. G. Belomoin, J. Rogozhina, J. Therrien, P.V. Braun, L. Abuhassan, M.H. Nayfeh, L. Wagner, and L. Mitas, *Phys. Rev. B.* **65**, 193406 (2002).

55. M. V. Wolkin, J. Jorne, P. M. Fauchet, G. Allan, and C. Delerue, *Phys. Rev. Lett.* **82**, 197 (1999).

56. G. Santana, B. M. Monroy, A. Ortiz, L. Huerta, J. C. Alonso, J. Fandiño, J. A. Hernandez, E. Hoyos, F. C. Gandarilla, and G. C. Puentes, *Appl. Phys. Lett*. **88**, 041916 (2006).

57. D. Ugarte, *Nature.* **359**, 707 (1992).

58. J. F. Moulder and J. Chastain, *"Handbook of X-ray photoelectron spectroscopy*", Perkin-Elmer Corporation, Physical Electronic Division (1992).

59. F. Klauser, R. Stijepovic, N. Endstarasser, S. Jaksh, N. Memmel, and P. Scheier, *Surf. Sci.* **603**, 2999 (2009).

60. K. Abderrafi, R.G. Calzada, M.B. Gongalsky, I. Suarez, R. Abarques, V. Chivrony, Yu. Timoshenko, R. Ibañez and J.M. Martinez-Pastor, *J. Phys. Chem. C* **115**, 5147 (2011).

61. K. Abderrafi, R.G. Calzada, J. F. Sanchez-royo, V. Chivrony, S. Agouram, R. Abarques, R. Ibañez, and J.M. Martinez-Pastor, *J. Phys. D: Appl. Phys.* **46**, 135301 (2013).

62. J. Solis, F. Vega, and C. N. Alfonso, *Appl. Phys. A* **62,** 197 (1996).

63. M. C. Beard, K. P. Knutsen, P. Yu, J. M. Luther, Q .Song, W. K. Metzger, R. J. Ellingson, and A. J. Nozik, *NanoLett*. **7**, 2506 (2007).

64. R. Intartaglia, K. Bagga, F. Brandi, G. Das, A. Genovese, E. Di Fabrizio, and A . Diaspro, *J. Phys. Chem. C* **115,** 5102 (2011).

65. G. Schierning, R. Theissmann, H. Wiggers, D. Sudfeld, A. Ebbers, D. Franke, V. T. Witusiewicz, and M . Apel, *J. Appl. Phys*. **103**, 084305 (2008).

66. H. C. Le, R. W. Dreyfus, W. Marine, M. Sentis, and I. A. Movtchan, *Appl. Surf. Sci.* **96**, 164 (1996).

67. C. C. Huang, K. Y. Chuang, C. J. Huang, M. Liu, and C. S. Yeh, *J. Phys. Chem. C* **115**, 9952 (2011)

68. S. Link and M. A. El-Sayed, *Int. Rev. Phys. Chem*. **19**, 409 (2000).

69. K. Lee and M. A. El-Sayed, *J. Phys. Chem. B* **110**, 19220 (2006).

70. L. N. Lewis, *Chem. Rev,* **93**, 2693 (1993)

71. A. L. Oldenburg, M. N. Hansen, D. A. Zweifel, A.Wei, and S. A. Boppart, *Opt. Express.* **14**, 6724 (2006).

72. X. Huang, I. H. El-Sayed, W. Qian, and M. A El-Sayed, *J. Am. Chem. Soc*. **128**, 2115 (2006).

73. M. A. Garcia, *J. Phys. D: Appl. Phys*. **44**, 283001 (2011).

74. K. Abderrafi, E. Jiménez, R. Abargues, J. P Martínez-Pastor, J. L. Valdés, and R. Ibáñez, *"Method for thesynthesis of inert metal nanoparticles"*, Universitat de Valencia Estudi General, *WO 2009/030799 A1,* March (2009).

75. E. Jiménez, K. Abderrafi, R. Abargues, J. L Valdés, and J. P Martínez-Pastor, *Langmuir* **26**, 745 (2010).

76. M. N. R. Ashfold, F. C. Fuge, and G. M S. Henley, *J. Chem. Soc. Rev*. **33**, 23 (2004).

77. A. Fojtik, M. Giersig, and A. Henglein, *Berichte der Bunsengesellschaft für physikalische Chemie* **97**, 1493 (1993).

78. S.I. Dolgaev, A. V. Simakin, V. V. Voronov, G. A. Shafeev, and B. Verduraz, *Appl. Surf. Sci.* **186**, 546 (2002).

79. T. Sakka, H. Yamagata, H. Oguchi, K. Fukami, and Y. H. Ogata, *Appl. Surf. Sci.* **255**, 9576 (2009).

80. H. Ushida, N. Takada, and K. Sasaki, *J. Phys Conf. Ser.* **59**, 563 (2007).

3. Conclusions

3. Conclusions

The most outstanding results from this thesis can be summarized as follows:

• ***GaAs Nanoparticles***

Pulsed laser ablation of a solid target in a confining liquid has been demonstrated to be an effective and general route to synthesize GaAs nanoparticles with crystalline/polycrystalline structure.

- Systematic studies of the influence of laser fluence carried out in this work to optimize conditions of the GaAs NPs formation.
- The average diameter of GaAs NPs as well as its dispersion were found to decrease with increasing the laser power.
- The stabilization of the GaAs colloidal solution was achieved by growing a thin film of SiO_2 around GaAs NPs, thus GaAs/SiO_2core/shell nanostructures were obtained.
- Measured optical absorbance spectra exhibit features consistent with size quantum confinement in these NPs.

• ***Silicon nanoparticles***

Small silicon nanoparticles were produced by ns-laser ablation in chloroform. The results show that small Si nanocrystals (3-5 nm in diameter following HRTEM images)were produced in a two-stage process including:

1st stage: Nanosecond laser ablation of a Si target in an organic liquid (chloroform) results in the formation of big composite polycrystalline NPs (about 20-100nm of average diameter).

2nd stage: An ultrasonic post-treatment of Si-composite NPs in the presence of HF is used for the disintegration of the big Si NPs, form small individual nanocrystals and reduce their size due to HF-induced etching of Si oxide.

- A downshift and broadening of the ~520 cm^{-1} Raman phonon band in small Si nanocrystals with respect to the bulk Si values are consistent with a colloid formed of Si nanocrystals ~4.5 nm of average diameter.
- The photoluminescence spectra (450-900 nm) and decay kinetics of small Si nanocrystals were analyzed and the possible origin of the luminescence attributed to

contributions from surface and core of Si nanocrystals affected of quantum size confinement.

With the use of HRTEM microscopy, selected area electron diffraction and x-ray photoelectron spectroscopy methods of analysis we show that the ns-laser ablation of a Si target in chloroform ($CHCl_3$) yields 50–80 nm core–shell nanoparticles with a polycrystalline core composed of small (5–10 nm) Si and SiC mono-crystallites, the core being coated by several layers of carbon with the structure of graphite (the shell). In addition, free carbon multilayer nanostructures (carbon nano-onions) are also found as free structures in suspension.

-The chemical formation of multilayer graphite nanostructures is due to the decomposition of chloroform molecules near the surface of big Si NPs, which is caused by NP heating as a result of laser absorption.
- The process consists in the formation of CH radicals and their interaction to form hydrocarbon polymers (as an intermediate product) and then graphite structures.
- An alternative preliminary hypothesis involves hydrogenation of the Si NP surface by hydrogen released due to thermal decomposition of $CHCl_3$ followed by photochemical cleavage of the Si–H bond under illumination by the 355 nm laser pulses and an interaction of the formed Si dangling bonds with products of the chloroform thermal decomposition.

On the basis of a comparison with similar laser ablation experiments implemented in carbon tetrachloride (CCl_4), where only bare (uncoated) Si nanoparticles are produced, we suggest that a chemical (solvent decomposition giving rise to highly reactive CH containing radicals) rather than a physical (solvent atomization followed by carbon nanostructure formation) mechanism is responsible for the formation of graphitic shells.

The results obtained in this work reveal that the process of graphitic shell formation under conditions of laser ablation in chloroform can be interesting for Si surface passivation, functionalization and protection.

• ***Metal nanoparticles***

We have developed an original, powerful technique based on the laser ablation of a target immersed in a water solution of a metal salt.

- With this method NPs of different metals and alloys can be processed very quickly. Both the target and the salt solution can be chosen to produce metal nanoparticles of different sizes, surface-oxidized nanoparticles (silica-silver, for example), or even more complex structures to be defined by the researcher on one or more steps, because the technique combines the advantages of both physical and chemical methods.
- Inert gold and silver NPs shielded by silica have been successfully synthesized by using a simple technique by means of the laser ablation of a solid target immersed in a water solution of a salt containing the metal desired to form the NPs, such as $AgNO_3$, $HAuCl_4$, or mixtures of them, with a strong surface plasmon resonance all together in a single step.
- This method has been validated by using several target materials, such as Si,Ge, and W. The local high temperatures reached during laser ablation allow fast and efficient chemical reactions to form metal NPs, mainly spherical with sizes in the range from 3 to 18nm. These chemical reactions together with the oxidation of the ablated material (Si, for example) lead to the direct formation of a stable colloid from (silica) shielded metal oxide NPs.
- Both the silica-metal formation and the presence of silica in the colloid ensure the use of our NPs in biotechnology/biomedical applications, given their inert character and stability, as was shown elsewhere (see other contribution of the authors in the Introduction to this thesis). The proposed method has been developed by using metal salts because of the high efficiency of the reduction reaction of metallic ions to metal atoms, but the application of the method to other salts in order to obtain different NPs(semiconductor, dielectric, magnetic, ...) could be also possible.

According to the results reported in this thesis, the remarkable advantages of PLAL and the resulting nanomaterials can be briefly summarized as follows. PLAL is an easy, “clean” and rapid fabrication method for different nanoparticles, nanocrystals and

nanostructures, due to the reduced number of by-products during the process, the use of simple precursors and the absence of catalysts, as general characteristics.

It is a versatile method to obtain diverse nanomaterials: metals, metal oxides and semiconductors, and combination of them. This is based on the strong ability of laser to ablate various targets in liquid or vacuum. It is also a method developed under ambient temperature and pressure conditions to obtain metastable and new-phase nanostructures that may not be attainable by other methods, especially under these conditions. This is due to the high temperature and pressures reached at the plume region formed during laser ablation.

4. Paper reprints

PUBLICACIÓN I

Production of nanometer-size GaAs nanocristals by nanosecond laser ablation in liquids

K. Abderrafi, E. Jiménez, T. Ben, S.I. Molina, R. Ibáñez, V. Chirvony, and J.P. Martínez-Pastor

J. Nanosci. Nanotechnol. **12**, 6774-6778 (2012).

Journal of
Nanoscience and Nanotechnology
Vol. 12, 6774–6778, 2012

Production of Nanometer-Size GaAs Nanocristals by Nanosecond Laser Ablation in Liquid

Kamal Abderrafi[1], Ernesto Jiménez[1], Teresa Ben[2], Sergio I. Molina[2], Rafael Ibáñez[1], Vladimir Chirvony[1], and Juan P. Martínez-Pastor[1,*]

[1] *UMDO (Unidad Asociada al CSIC-IMM), Instituto de Ciencia de Materiales, Universidad de Valencia, P.O. Box 22085, 46071 Valencia, Spain*
[2] *Dpto. Ciencia de los Materiales e IM y QI, Universidad de Cádiz, Apto.40, 11510 Puerto Real, (Cádiz), Spain*

This paper reports the formation and characterization of spherical GaAs quantum dots obtained by nanosecond pulsed laser ablation in a liquid (ethanol or methanol). The produced bare GaAs nanoparticles demonstrate rather narrow size distribution which depends on the applied laser power density (from 4.25 to 13.9 J/cm^2 in our experiments) and is as low as 2.5 nm for the highest power used. The absolute value of the average diameter also decreases significantly, from 13.7 to 8.7 nm, as the laser power increases in this interval. Due to the narrow nanoparticle size dispersion achieved at the highest laser powers two absorption band edges are clearly distinguishable at about 1.72 and 3.15 eV which are ascribed to E_0 and E_1 effective optical transitions, respectively. A comparison of the energies with those known for bulk GaAs allows one to conclude that an average diameter of the investigated GaAs nanoparticles is close to 10 nm, i.e., they are quantum dots. High resolution transmission electron microscopy (HRTEM) images show that the bare GaAs nanoparticles are nanocrystalline, but many of them exhibit single/multiple twin boundary defects or even polycrystallinity. The formation of the GaAs crystalline core capped with a SiO_2 shell was demonstrated by HRTEM and energy dispersive X-ray (EDX) spectroscopy. Effective band edges can be better distinguished in SiO_2 capped nanoparticles than in bare ones, In both cases the band edges are correlated with size quantum confinement effect.

Keywords: Semiconductor Nanoparticles, GaAs Nanocrystal Quantum Dots, Liquid Laser Ablation, High Resolution Transmission Electron Microscopy (HRTEM), Core–Shell Quantum Dots.

1. INTRODUCTION

GaAs is one of the most important III–V semiconductors that finds wide applications in electronic industry (optoelectronic devices)[1] as well as is promising for solar cell production.[2] Even more interesting may be properties of GaAs nanoparticles taking in account their large energy bandgap and a large exciton Bohr radius (15 nm)[3] so that the quantum confinement effect is very pronounced for relatively big nanoparticles (NPs). However, contrary to II–VI compounds (CdTe, CdSe, CdS) the preparation and characterization of nanocrystals of III–V compound semiconductors, and in particular of GaAs is not so well documented. The reason of this is the difficulty in preparing pure GaAs nanocrystals with reproducible properties because, III–V materials are not appropriate to withstand high temperature and oxidizing conditions during NPs chemical synthesis.

The most developed are chemical methods of GaAs NPs synthesis.[4–9] Under such an approach the GaAs NPs tend to be prolate, with an aspect ratio in the range of 1.2–1.3,[4–6] the particles also tend to be gallium rich with a Ga:As ratio as high as 5:4.[4,6] Several studies found the presence of an amorphous oxide layer on the GaAs particle surface,[5] as well as of molecular species[8] and a chlorine impurity,[4,6,7] the latter being a common problem when $GaCl_3$ is used as the Ga source.

Among other methods of GaAs NPs preparation, such as molecular beam epitaxy,[10] rf sputtering,[11] ion implantation,[12,13] and laser ablation[14–17] the latter one seems to be the less expensive and the most promising from the point of view of chemical purity and crystallinity of the final product, as it was earlier shown for the case of Si nanocrystals.[18] However, very little was

*Author to whom correspondence should be addressed.

1533-4880/2012/12/6774/005 doi:10.1166/jnn.2012.4548

done in this direction for GaAs nanocrystals. In particular, in the nanosecond regime of the pulsed laser ablation (PLA) stoichiometric GaAs NPs have been produced provided the ablation is carried out in the presence of a buffer gas.[14] On the other hand, films of GaAs NPs deposited by nanosecond PLA *in vacuum* were found to be noncrystalline and to lack stoichiometric concentrations of Ga and As.[15] Application of the femtosecond regime of the PLA has confirmed that mainly stoichiometric GaAs NPs are produced in presence of a buffer gas, whereas excess amorphous Ga or As was observed in case of ablation in vacuum.[16] Gallium-rich GaAs NPs were synthesized by nanosecond PLA of a GaAs wafer *in liquids* of different viscosity (water, ethanol, ethylene glycol, silicon oil).[17] As our analysis shows, common drawbacks of the above PLA studies are an absence of

(i) statistical investigation of the GaAs NPs size distribution,

(ii) analysis of the NPs crystallinity and its quality,

(iii) correlation between such structural/morphological information with basic optical properties of the NP colloids.

In the present work we report the preparation of stable colloidal solutions of GaAs quantum dots (QDs, i.e., NPs possessing sufficiently small size to exhibit quantum confinement effect) by PLA of the corresponding bulk material in liquids and the investigation of their optical and structural properties. The absorption spectra of the colloids exhibit blue shift of the bandgap edge as compared to bulk GaAs, better observed in the case of NPs capped with SiO_2, the shift being consistent with the measured average size of GaAs QDs in the colloids (about 8–10 nm depending on the PLA conditions). The NPs are typically polycrystalline, but perfectly nanocrystalline NPs or nanocrystalline with planar defects were also detected. As a way to improve a stability of the GaAs NP colloids and to have more possibilities for their applications, we have also encapsulated GaAs NPs in SiO_2 shell by a standard chemical technique. Silica surface is known to be well suitable for easy functionalization by thiol, amine, and carboxylate molecules[19, 20] that is a necessary preliminary step to use these NPs in biomolecule conjugation protocols.

2. EXPERIMENTAL DETAILS

GaAs colloidal QDs were grown by using a simple experimental approach based on the laser irradiation of a bulk GaAs target placed at the bottom of a glass vessel containing 20 ml of a liquid such as methanol or ethanol with a purity of 99.99%. The laser used for ablation is a 2nd harmonic (green) Nd:YAG laser ($\lambda = 532$ nm) generating pulses of 10 ns duration at a maximum repetition rate of 5 KHz. The laser radiation was focused on the target surface to deliver power densities (fluences) per pulse below 14 J/cm^2. After a few minutes of GaAs target irradiation at room temperature, an appearance of nanoparticles is clearly seen by a change of the liquid color. In a second stage, the NPs were covered with amorphous SiO_2 by hydrolysis of Tetra-Ethyl-Ortho-Silicate [TEOS, formula $Si(OCH_2CH_3)_4$] at $T = 0$ °C by using the well-known Stöber method. The preparation consisted in mixing 20 ml of the NP colloidal solution with 250 μl of TEOS and 25 μl of water in an ultrasonic bath. The injection of water and TEOS was made separately to prevent agglomeration and sedimentation effects of SiO_2. The use of that low temperature ($T = 0$ °C) during the process of the NP capping by SiO_2 enables one to avoid a rapid TEOS hydrolysis since the reaction rate is proportional to H_2O concentration and temperature.[21]

Optical absorption investigations of the colloids were performed with a UV-VIS SHIMADZU 2501 spectrophotometer. Transmission Electron Microscopy (TEM) images were obtained with a JEOL 1200EX and a JEOL 2011EX microscopes operating at 120 and 200 kV, respectively. Energy Dispersive X-Ray (EDX) spectroscopy measurements were performed with an Oxford Instruments ultrathin-window detector. The specimens for TEM and EDX studies were prepared by dropping colloid solution of the GaAs NPs on a carbon coated copper grid, which was left to dry before transferring into the microscope.

3. RESULTS AND DISCUSSION

Figure 1 shows TEM images obtained for drop coated films of GaAs NPs produced by laser ablation. The GaAs NPs are predominantly spherical in shape (Fig. 1(a)) and exhibit a size dispersion, which depends on the laser power density used for a GaAs target ablation (Fig. 1(b)): the dispersion is rather wide for the low laser powers (4.2 J/cm^2) and considerably narrows under increase of the power density. In particular, the dispersion of the NPs diameter measured at half of the dispersion curve maximum is only 2.5 nm for the highest laser fluence used that is rather close to the values known for NPs obtained by chemical synthesis (around 1 nm).[22] The absolute value of the average diameter also decreases significantly, from 13.7 to 8.7 nm, as the laser power increases from 4.25 to 13.9 J/cm^2. Figure 1(c) shows this variation, which can be well fitted by an exponential decrease of NP diameter as a function of PLA laser power. This behavior is consistent with the existence of a threshold power to obtain NPs that can be a result of the plume plasma confinement in a liquid and the corresponding increase of temperature and pressure caused by increasing laser power.[23]

High density of defects has been observed in HRTEM micrographs of GaAs colloidal QDs produced in our PLA experiments in a liquid. Most of them have been identified as edge dislocations, promoting some portions of the

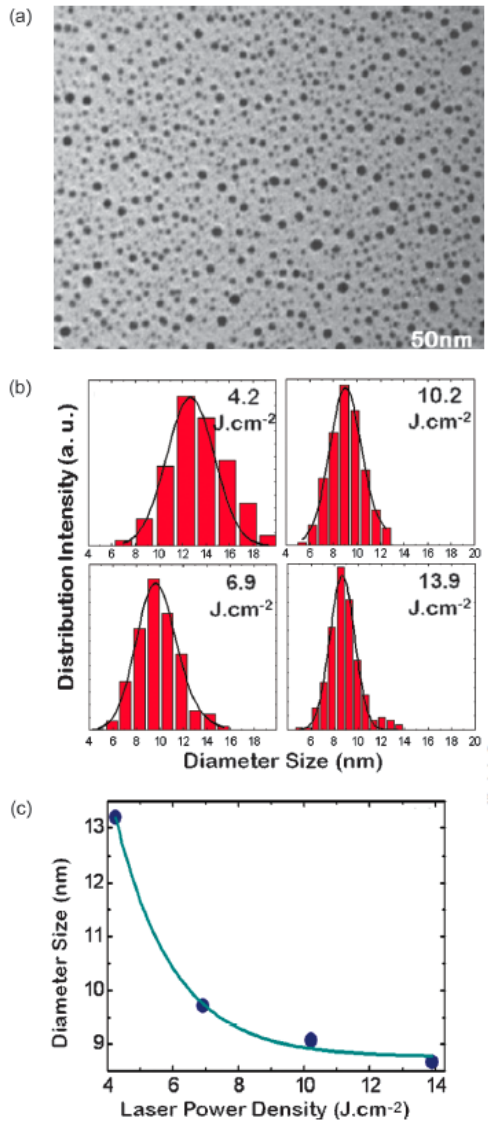

Fig. 1. (a) TEM micrograph of GaAs nanoparticles grown by laser ablation in methanol using a laser power density of 4.25 J/cm^2. (b) Size distributions of GaAs nanoparticles produced by laser ablation in methanol for several laser powers. (c) The average size is plotted as a function of the laser power density.

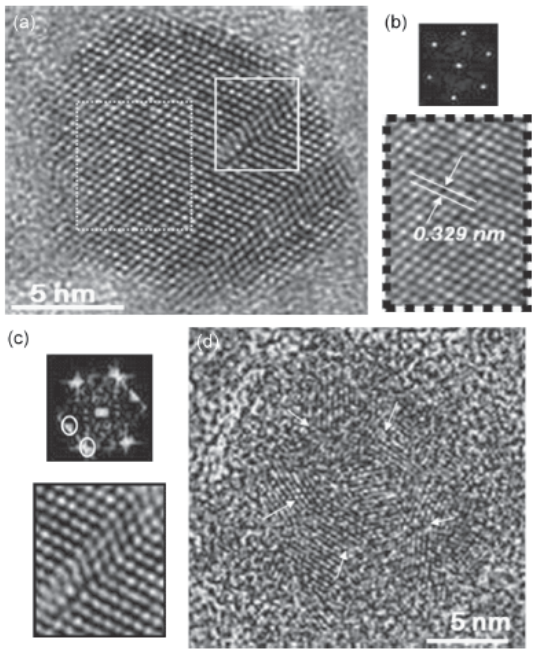

Fig. 2. (a) HRTEM image of a nanoparticle of GaAs prepared by laser ablation in methanol with the laser power density 4.25 J/cm^2. (b) Perfect crystalline area within the dashed square of HRTEM image (a) with its corresponding FFT. (c) Area within the solid square in (a) exhibiting twinning with its corresponding FFT showing characteristics spots from this defect. (d) HRTEM image of a polycrystalline nanoparticle. White arrows mark the position of polycrystalline grains in the nanoparticle.

nanocrystals along the direction perpendicular to the dislocation, as well as micro-twin boundaries and even multi-twin defects. However, as shown in Fig. 2(a), single twin boundaries do not exclude that the growth of the particles can occur following a preferential crystallographic orientation. This orientation can be determined, for example, on the basis of the magnified images of the two areas marked by solid and dotted squares in HRTEM micrographs shown in Figure 2(a). The magnified image of the dotted square area is shown in Figure 2(b). It corresponds to a face-centered cubic (fcc) structure with a periodic fringe spacing of 0.329 nm, associated to {111} planes of bulk GaAs.[27] This can be clearly observed in the Fast Fourier Transformation (FFT) image obtained from the real image of the GaAs quantum dot crystalline material (upper image in Fig. 2(b)). On the other hand, an example of crystalline defects is displayed in the HRTEM image of Figure 2(c), the image corresponds to the solid square area of Figure 2(a). An analysis of this image and its respective FFT (see Fig. 2(c)) shows that the defect is a microtwin. Such twin defects can alter the right crystal growth giving rise to surfaces with multiple crystallographic orientations. Figure 2(d) shows an example of a HRTEM image of the NP consisting of several polycrystalline grains, which are marked by white arrows. These defects can arise from condensation effects of laser ablation during NPs production rather than from strain relaxation.[28] The temperature gradient between the external surface of the plasma and the liquid solution, where the growth of GaAs nanocrystals takes place,[29] can lead to the formation of a new thermodynamic stage characterized by an adiabatic cooling of the plasma. However, during this period the exerted pressure is too small to cause crystalline deformations.[30] Additionally, after NPs formation some chemical reactions can take

place at the interface between atoms forming solid NPs and molecules in liquid solution. This can lead to chemical modification of the NP surface by means of incorporation or elimination of some ions or molecules that can result, in its turn, to unbalanced stoichiometry. These features of the surface structure are able to form new crystallographic defects such as vacancies or interstitials.

GaAs/SiO_2 core–shell structured particles of nanometer-size dimensions have also been prepared in the present work via the chemical procedure based on hydrolysis of TEOS ($Si(OCH_2CH_3)_4$) at 0 °C from a GaAs NP colloidal solution previously fabricated by laser ablation at a laser fluence close to the maximum values used. The SiO_2-covered NPs have an average diameter of about 14 nm (Figs. 3(a, b)), that is they are more larger than bare NPs obtained with use of a similar laser fluence (13.9 J/cm^2 in Fig. 1(b)). This difference is consistent with the incorporation of SiO_2 as an outer shell capping GaAs NPs that is demonstrated by the HRTEM image in Figure 3(c) and by the EDX spectrum in Figure 3(d). The core diameter and the thickness of the silica shell measured for several NPs by HRTEM were found to be in the ranges of 8–13 nm and 3–5 nm, respectively. These numbers are consistent with the average GaAs/SiO_2 diameter (around 14 nm) and that of bare GaAs NPs (around 8.7 nm), i.e., the average SiO_2 shell thickness would be 2.75 nm, very close to the values measured by HRTEM in some NPs ramdonly selected.

As one can see from the Figure 4, the absorbance spectra of uncapped and SiO_2 capped GaAs NPs are rather

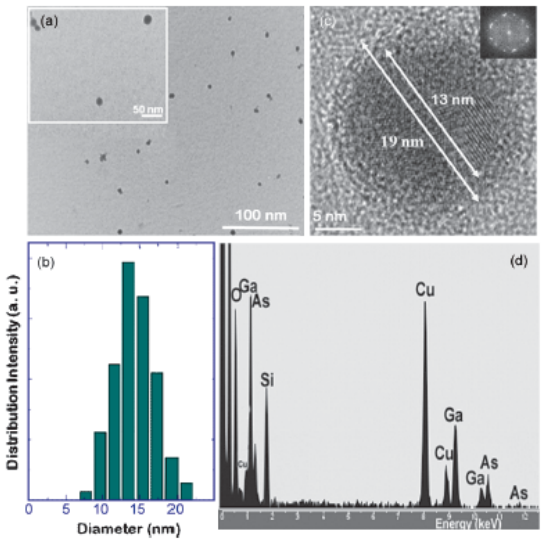

Fig. 3. TEM micrographs (a), size distribution (b), HRTEM image (c), and EDX spectrum (d) of GaAs/SiO_2 core/shell nanoparticles. The core radius is about 13 nm and the shell thickness is 3 nm. The inset shows the FFT from the HRTEM image. The Cu peaks in EDX spectrum arise from the grid.

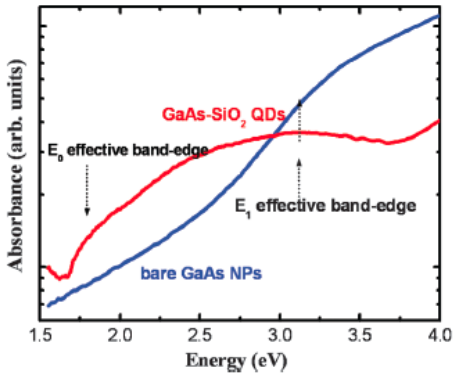

Fig. 4. The absorption spectra of uncapped and SiO_2 capped GaAs nanoparticles.

different. The plot is made logarithmic after substracting a λ^{-4} background in order to better distinguish intrinsic features that could be associated to optical transitions in the NPs. A first absorption edge can be distinguished at around 1.75 eV in the case of SiO_2 capped GaAs NPs, whereas any feature (a monotonous increase) is observed in bare GaAs NPs. In the range 3.1–3.3 eV a second band edge is observed in both kinds of NPs (a broad maximum in the case of capped NPs).

The origin of the two band edges observed in our NP colloids can be ascribed to the effective E_0 (direct bandgap at Γ-point) and E_1 (direct bandgap at L-point) band gaps formed due to quantum confinement effect. Indeed, the values for E_0 (E_g^{bulk}) and E_1 in bulk GaAs are 1.42 and 2.9 eV, respectively.[24] Using a simple model for quantum confinement in a semiconductor QD with infinite barriers the effective band gap for the QD is $E_g^* = E_g^{\text{bulk}} + 2\hbar^2\pi^2/m^*D^2$, where D is the NP diameter and m^* is the reduced effective mass (about $0.067m_0$). According to the above formula the first experimental band edge near 1.75 eV would correspond to a QD diameter of 9.2 nm that is not very far from the average value, 8.5 nm, in SiO_2 capped GaAs NPs. In case of the E_1 optical transition the quantum confinement effect should be less pronounced, because the band curvatures at L-point are smaller than those at Γ-point, i.e., the effective absorption band edge would be expected below 3.13 eV, which is within the experimental incertainty caused by the observed broad and smooth absorption spectra.

4. CONCLUSION

Pulsed laser ablation of a solid target in a confining liquid has been demonstrated to be an effective and general route to synthesize GaAs nanocrystals and nanostructures. Systematic studies of the influence of laser power and irradiation time were carried out in this work to optimize conditions of the GaAs NPs formation. The average diameter as well as the dispersion of the diameter of the produced

GaAs NPs, were found to decrease with increasing the laser power. The stabilization of the GaAs colloidal solution was realized by growing a thin film of SiO_2 around GaAs NPs, thus a GaAs/SiO_2 core/shell nanostructure was built up. Measured optical absorbance spectra exhibit features consistent with size quantum confinement in our NPs.

Acknowledgment: This work was supported by through the Spanish MCINN Grant Nos. TEC-2008-06756-C03-03/-02, the "Generalitat Valenciana" project PROMETEO/2009/074, and the "Junta de Andalucia" (PAI research group TEP-0120; project PAI05-TEP-00383).

References and Notes

1. A. Bar-Lev, Semiconductors and Electronic Devices, 2nd edn., Prentice Hall, New York (**1984**).
2. A. Luque, A. Marti, and A. J. Nozik, *MRS bulletin* 32, 236 (**2007**).
3. Y. Fu, M. Willander, and E. L. Ivchenko, *Superlattices Microstruct.* 27, 255 (**2000**).
4. M. A. Olshavsky, A. N. Goldstein, and A. P. Alivisatos, *J. Am. Chem. Soc.* 112, 9438 (**1990**).
5. P. C. Sercel, W. A. Saunders, H. A. Atwater, and R. C. Flagan, *Appl. Phys. Lett.* 61, 696 (**1992**).
6. S. S. Kher and R. L. Wells, *Chem. Mater.* 6, 2056 (**1994**).
7. O. V. Salata, P. J. Dobson, P. J. Hull, and J. L. Hutchison, *Appl. Phys. Lett.* 65, 189 (**1994**).
8. H. Uchida, C. J. Curtis, P. V. Kamat, K. M. Jones, and A. J. Nozik, *J. Phys. Chem.* 96 1156 (**1992**).
9. M. A. Malik, P. O'Brien, S. Norager, and J. Smith, *J. Mater. Chem.* 13, 2591 (**2003**).
10. C. J. Sandorff, J. P. Harbicon, R. Ramesh, M. J. Andrejco, M. S. Hedge, D. M. Hwang, C. C. Chang, and E. M. Vogel, *Science* 245, 391 (**1989**).
11. M. Hirasawa, H. Shirakawa, H. Hamamura, Y. Egashira, and H. Komiyama, *J. Appl. Phys.* 82, 1404 (**1997**).
12. Y. Kamenitsu, H. Tanaka, T. Kushida, K. S. Min, and H. A. Atwater, *J. Appl. Phys.* 86, 1762 (**1999**).
13. C. W. White, J. D. Budai, J. G. Zhu, S. P. Withrow, R. A. Zhur, D. M. Hembree, Jr, D. O. Henderson, A. Ueda, Y. S. Tung, R. Mu, and R. H. Magruder, *J. Appl. Phys.* 79, 1876 (**1996**).
14. J. Perriere, E. Millon, M. Chamarro, M. Morcrette, and C. Andreazza, *Appl. Phys. Lett.* 78, 2949 (**2001**).
15. L. N. Dinh, S. Hayes, C. K. Saw, W. McLean, M. Balooch, and J. A. Reimer, *Appl. Phys. Lett.* 75, 2208 (**1999**).
16. T. W. Trelenberg, L. N. Dinh, C. K. Saw, B. C. Stuart, and M. Balooch, *Appl. Surf. Sci.* 221, 364 (**2004**).
17. R. A. Ganeev, M. Baba, A. I. Ryasnyansky, M. Suzuki, and H. Kuroda, *Appl. Phys. B* 80, 595 (**2005**).
18. V. Svrcek, *Pure Appl. Chem.* 80, 2513 (**2008**).
19. S. T. Selvan, C. Li, M. Ando, and N. Murase, *Chem. Lett.* 33, 4 (**2004**).
20. M. T. Harris, R. R. Brunson, and C. H. Byers, *J. Non-Cryst. Solids* 121, 397 (**1990**).
21. L. Zhou, W. Yuan, J. Yuan, and X. Hong, *Mater. Lett.* 62, 1372 (**2008**).
22. J. Nayak, R. Mythili, M. Vijayalakshmi, and S. N. Sahu, *Physica E* 24, 227 (**2004**).
23. A. Borowiec, M. Mackenzie, G. C. Weatherly, and H. K. Haugen, *Appl. Phys. A* 77, 411 (**2003**).
24. S. Adachi, Properties of Group-IV, III-V, and II-VI Semiconductors, Wiley & Sons Ltd., Chichester, West Sussex, England (**2005**).
25. T. Takagahara, *Phys. Rev. B* 17, 9293 (**1987**).
26. M. Nisoli, S. Stagira, S. De Silvestri, A. Stella, P. Tognini, P. Cheyssac, and R. Kofman, *Phys. Rev. Lett.* 78, 3575 (**1997**).
27. E. Nelson, J. Woicik, and P. Pianetta, *J. Synchrotron Rad.* 6, 341 (**1999**).
28. M. H. Tsai, P. Shen, and S.-Y. Chen, *J. Europ. Cer. Soc.* 28, 1631 (**2008**).
29. D. B. Geohegan, A. A. Puretzky, G. Duscher, and S. J. Pennycook, *Appl. Phys. Lett.* 72, 2987 (**1998**).
30. J. Feder, K. C. Russel, J. Lothe, and G. M. Pound, *Adv. Phys.* 15, 111 (**1966**).
31. G. Pellegrini, G. Mattei, and P. Mazzoldi, *J. Appl. Phys.* 97, 073706 (**2005**).

Received: 15 September 2010. Accepted: 18 February 2011.

PUBLICACIÓN II

Silicon quantum dots produced by nanosecond laserablation in an organic liquid

K. Abderrafi, R. García Calzada, M.B. Gongalsky, I. Suárez, V. Chirvony, R. Abargues, V.Yu. Timoshenko, R. Ibáñez, and J. Martínez-Pastor

J. Phys. Chem C **115**, 5147–5151 (2011)

THE JOURNAL OF PHYSICAL CHEMISTRY C

ARTICLE

pubs.acs.org/JPCC

Silicon Nanocrystals Produced by Nanosecond Laser Ablation in an Organic Liquid

Kamal Abderrafi,[†] Raúl García Calzada,[†] Maxim B. Gongalsky,[‡] Isaac Suárez,[†] Rafael Abarques,[†] Vladimir S. Chirvony,[†,*] Victor Yu. Timoshenko,[‡] Rafael Ibáñez,[†] and Juan P. Martínez-Pastor[†]

[†]UMDO - Unidad Asociada a CSIC-IMM, Instituto de Ciencia de los Materiales, Universidad de Valencia, P.O. Box 22085, 46071 Valencia, Spain

[‡]Department of Physics, Lomonosov Moscow State University, Leninskie Gory 1, 119992 Moscow, Russia

ABSTRACT: Small (3−5 nm in diameter following HRTEM images) Si nanocrystals were produced in a two-stage process including (1) nanosecond laser ablation of a Si target in an organic liquid (chloroform) that results in formation of big composite polycrystalline particles (about 20−100 nm average diameter) and (2) ultrasonic post-treatment of Si nanoparticles in the presence of HF. The post-treatment is responsible for disintegration of the composite Si particles, release of small individual nanocrystals, and reduction of their size due to HF-induced etching of Si oxide. The downshift and broadening of the ~520 cm^{-1} Raman phonon band of the small Si nanocrystals with respect to the bulk Si Raman band is consistent with the presence of ~4.5 nm Si nanocrystals. The photoluminescence spectra (450−900 nm) and decay kinetics of small Si nanocrystals were detected, and the possible origin of the luminescence is discussed.

1. INTRODUCTION

Silicon nanocrystals (NCs) are a promising new material. A broad interest in this system is stimulated by its potential applications in light sources,[1] nonvolatile memory devices,[2] solar cells,[3] medicine (Photodynamic Therapy),[4] and bioimaging.[5] The most considerable obstacle on the way to a wide use of Si NCs in different applications is the lack of simple and inexpensive methods of their production. Besides, strict requirements are imposed for the nanoparticles used in living systems: first of all, the chemical purity of the product is important, a requirement which is difficult fulfill when the most commonly used chemical (wet) methods of synthesis are applied. Laser ablation in liquids (first of all in deionized water) is considered in the literature as a contamination-free green synthesis method[6] which meets, in general, all the above requirements.

An application of the method of a laser ablation in liquids (LAL) for production of Si NCs is still in its infancy. As a rule, Si NCs produced by this method are reported to be rather big (tens of nanometers and more) and possessing wide size distribution,[7] whereas most interesting for applications are nanoparticles, which exhibit quantum-confinement effect; in the case of Si NCs it corresponds to a diameter of the order of 5 nm and less. Only very recently Si NCs with an average size of several nanometers have been obtained by the LAL method.[8,9] In ref 8 very small Si NCs of the average diameter of 2.5 nm were produced in water by femtosecond laser ablation (120 fs pulses at 800 nm wavelength) at very low, near-threshold fluences of excitation light (0.05 J cm^{-2}). In ref 9 small-size Si NCs (average diameters of 3−7 nm) were produced by means of nanosecond laser ablation in ethanol, whereas much bigger particles were synthesized in water.[9]

Therefore, an important role of a liquid in LAL experiments directed to produce small-size Si NCs was discovered in ref 9, but details of this effect are not yet clear. The aim of the present work is to investigate the possibility of manufacturing small-size Si NCs by means of nanosecond laser ablation in organic liquids. We used chloroform, $CHCl_3$, as a medium to produce Si NCs by the LAL method because there is evidence in the literature about interactions of halogen-substituted hydrocarbons with Si nanostructures.[10] One can suggest that this interaction can be helpful for Si NC size limitation during the NC growth process similarly to the case of Au nanoparticle (NP) size limitations induced by the presence of organic molecules in water during laser ablation.[11]

2. EXPERIMENTAL DETAILS

A *p*-type Cz-silicon wafer of (100) plane with a resistivity of 10−20 Ω cm was ultrasonically rinsed first with deionized water and then ethanol for 1 h. The cleaned silicon wafer was used as a target, immersed in liquid medium ($CHCl_3$, or chloroform, 20 mL in an open glass vessel) and irradiated with the third

Special Issue: Laser Ablation and Nanoparticle Generation in Liquids

Received: September 30, 2010
Revised: January 17, 2011
Published: February 14, 2011

dx.doi.org/10.1021/jp109400v | *J. Phys. Chem. C* 2011, 115, 5147–5151

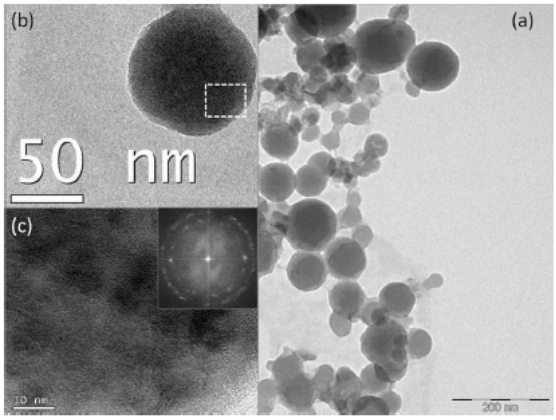

Figure 1. (a) TEM micrograph of silicon nanoparticles produced by laser ablation in chloroform. (b) HRTEM image of one big nanoparticle. (c) Amplified HRTEM image of the rectangular area outlined in (b). X-ray diffraction pattern is shown in the inset.

harmonic of pulsed Nd:YAG laser (355 nm, 40 ns pulse duration, 5 kHz repetition rate). The laser beam was focused by a lens having a focal length of 60 mm on the silicon target surface with a spot of about 30 μm diameter giving power densities per pulse ~40 J cm^{-2}. The solution was continuously stirred during laser irradiation. The target was scanned by the beam over the area of 56 mm^2 by means of an electro-optical beam deflector. A twenty-time repetition of the surface full scanning was found to be sufficient to observe the appearance of brownish color of the liquid, but usually hundreds of repetitions were applied.

After finishing the laser ablation procedure, an appropriate physicochemical post-treatment was applied as a second stage to obtain small-size monocrystalline silicon nanoparticles (NPs). First, chloroform suspension was transferred to plastic vessel. Then chloroform was evaporated under vacuum, and the precipitate formed on the vessel bottom was covered by the mixture of isopropanol, HF, and hexane (3:1:3). The vessel with the suspension was immersed in an ultrasound bath. Ultrasonic homogenizer "Sonoplus" HD 2200 (Bandelin) was applied for 30 min (power 80 W) for ultrasonic treatment of suspensions of Si NPs. All liquids used ($CHCl_3$, isopropanol, HF, hexane) were from Aldrich.

Si NPs obtained after the first (laser ablation) and second (post-treatment) stages were examined by transmission electron microscopy (TEM) with a JEOL-1200EX microscope and by High Rresolution TEM (HRTEM) with a FEI-TECNAI G2 instrument which were operated, respectively, at 100 and 200 KV. A suspension of Si NPs was placed on a copper mesh TEM grid coated on one side with carbon, and a solvent was completely evaporated at room temperature before transferring a grid with NPs into the microscope. NP size distributions were acquired by counting more than 500 NPs.

Raman scattering measurements were carried out under excitation with a 488 nm Ar-ion laser line using a Lab RAM HR800 micro-Raman system. Laser power was 100 mW, with accumulation time −3 scans of 60 s, and a 10× objective was used. Si NPs were deposited on the stainless steel surface by dropping a suspension and evacuation of a solvent by heating at 60 °C. This procedure was repeated about 10 times to increase

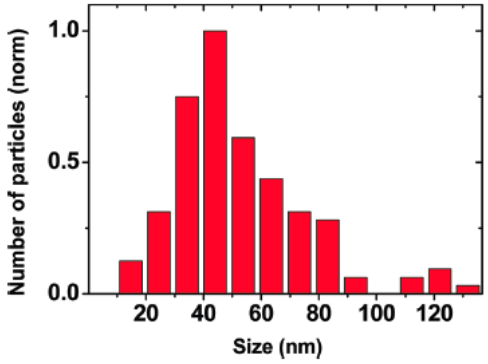

Figure 2. Size distribution calculated from TEM images of Si nanoparticles obtained by nanosecond laser ablation in chloroform.

the final concentration of Si NPs. All spectral experiments were done at room temperature in air.

The photoluminescence (PL) and PL kinetics were measured under excitation with a N_2-laser (wavelength λ = 337 nm, pulse duration τ = 10 ns, pulse energy E = 1 μJ, repetition rate ν = 100 Hz). The laser beam was focused by using a 20 cm lens into a spot of about 1 mm in diameter onto the sample (Si NPs on a quartz plate deposited by suspension dropping method). PL emission was collected on a 50 cm spectrometer equipped with a Si photomultiplier (time resolution of 100 ns).

3. RESULTS AND DISCUSSION

Laser ablation of a silicon target immersed in chloroform produced Si nanoparticles of a rather big size (tens of nanometers, see Figure 1). Particles are spherical in shape (Figure 1a and b), and their average size is about 50 nm. The size distribution of particles is shown in Figure 2. It should be noted that small particles with sizes less than 10−20 nm are practically absent in this distribution. HRTEM analysis of the morphology of these large-size particles shows that they have a polycrystalline microstructure. It was difficult to determine size distribution of the elementary crystallites inside the spherical particles shown in Figure 1a, but HRTEM images show the presence of monocrystallites with size of about 10 nm (Figure 1c; the corresponding XRD pattern is also shown as an inset).

We suggested that these polycrystalline Si NPs may consist of at least two materials: small Si crystallites visible in HRTEM images and Si oxide produced due to the presence of dissolved molecular oxygen in a liquid. We hypothesized that these complex structures can be disintegrated with simultaneous release of monocrystalline Si nanoparticles in the case when ultrasonic impact (for disconnection of the constituents) will be applied together with chemical treatment by HF (for silicon oxide etching).

The post-treatment procedure was implemented as follows. A transparent brownish suspension of silicon nanoparticles in chloroform was transferred into a plastic vessel. Then chloroform was evaporated, and the vessel was filled with a mixture of solvents isopropanol/HF/hexane (3:1:3). After shaking for a few seconds, the liquid mixture split into two parts: (1) a bottom (polar) part, consisting of isopropanol, water (as a part of HF solution), and HF, and (2) an upper (nonpolar) part, consisting of hexane.

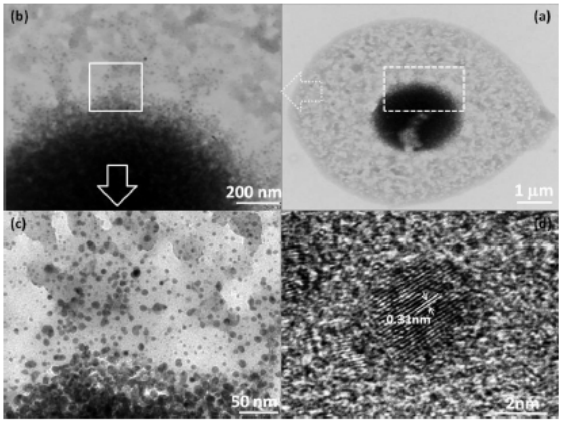

Figure 3. TEM micrographs of Si NCs after combined ultrasonic and chemical (HF) treatment: general view of NC agglomeration formed on the carbon membrane of the TEM grid (a and b); a view of individual NCs on the periphery of the agglomeration (c); and HRTEM of an individual Si NC (d).

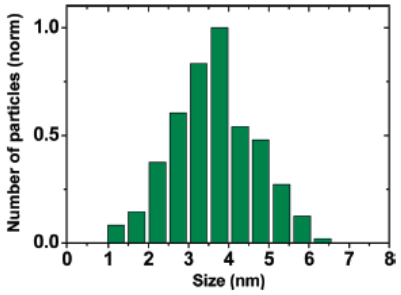

Figure 4. Size distribution calculated from TEM images of Si nanoparticles obtained by laser ablation in chloroform and then subjected to ultrasonic/HF post-treatment.

Before the beginning of the ultrasonic treatment all nanoparticles are in the bottom (polar) part of the liquid mixture. The location of nanoparticles in the bottom layer implies that their surface contains polar groups (usually Si−O and Si−OH formed due to Si surface interaction with molecular oxygen dissolved in liquids[12]).

Next, the suspension was subjected to ultrasonic treatment for 30 min. After the treatment, the bottom layer of the mixture became transparent, whereas the upper layer (hexane) acquired a yellowish color because all Si NPs turned out to be here. It implies that the Si NP surface became hydrophobic (due to surface covering by hydrogen[12]). Our preliminary FTIR measurements (in KBr tablets, not shown) performed with Si NPs extracted from hexane solution have also demonstrated the presence of a Si−H_x group characteristic band near 2100 cm^{-1}.

TEM micrographs of Si NCs after combined ultrasonic and chemical (HF) treatment are shown in Figure 3. For implementation of TEM measurements a drop of hexane suspension was deposited on the carbon membrane of the TEM grid. Evaporation of the solvent (hexane) led to the formation of a large agglomerate of nanoparticles with a total size of about 1 μm (Figure 3a, b). One can see in Figure 3c the presence of single

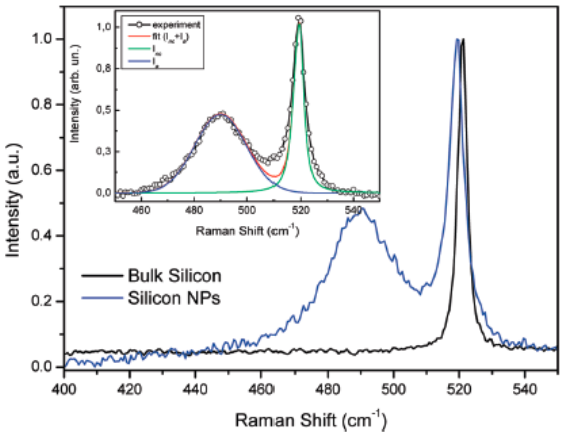

Figure 5. Raman spectrum of Si NCs after post-treatment (blue) as compared to the spectrum of bulk silicon (black). In the inset the same experimental Raman spectrum is shown (open circles) along with the model spectrum (red) obtained by summation of the model Gaussian (blue, for wide band at ~490 cm^{-1}) and modified Lorentzian (green, for narrow band at ~520 cm^{-1}) contours.

nanoparticles and their small clusters (consisting of a few particles) on the periphery of the agglomeration. Individual Si NPs (Figure 3d) exhibit a lattice fringe image spacing of 0.31 nm, which coincides with the (111) lattice constant for the Si diamond structure. Figure 4 shows typical size distribution of individual nanoparticles obtained by laser ablation in chloroform followed by ultrasonic post-treatment in the presence of HF. The maximum of this distribution is around 4 nm.

Raman spectroscopy provides information important for understanding the microstructure of Si NPs. Figure 5 shows Raman spectra of Si NPs after post-treatment (blue) and of bulk silicon (black). It is well-known that the bulk Si crystal displays a narrow optical phonon band at ~520.5 cm^{-1}. When Si crystallites become small enough (≤10 nm), the Raman phonon band broadens and shifts down in energy, and the shift can be connected with the crystallite size in the quantitative phonon confinement model by eq 1[13]

$$\Delta\nu = -52.3(0.543/D)^{1.586} \quad (1)$$

when $\Delta\nu$ is the shift (due to spatial confinement) of the Raman peak position of Si nanocrystals compared with the bulk value, and D is Si nanocrystal size ($\Delta\nu$ and D are in cm^{-1} and nm, respectively).

Namely, such a broadened and downshifted (2.0 cm^{-1} as compared to bulk Si) Raman band is observed for Si NPs produced in chloroform and then subjected to ultrasonic/HF post-treatment (Figure 5). Following (1), such a shift corresponds to 4.3 nm size of Si nanocrystals that is in good agreement with TEM-based size distribution.

Besides the band near 520 cm^{-1}, a broad band centered at 490 cm^{-1} is also detected for Si NPs produced by laser ablation in chloroform and subjected to post-treatment (Figure 5). It is known from the literature that this lower-energy Raman band belongs to disordered (amorphous) Si structures.[14] As one can see in the inset of Figure 5, the experimental two-band Raman spectrum (open circles) can be satisfactorily fitted by a sum of the modified Lorentzian (for narrow band at 520 cm^{-1}) and

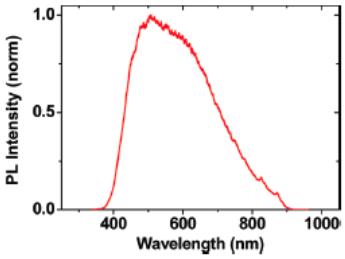

Figure 6. PL spectrum of isopropanol suspension of Si NPs produced by nanosecond LA in chloroform.

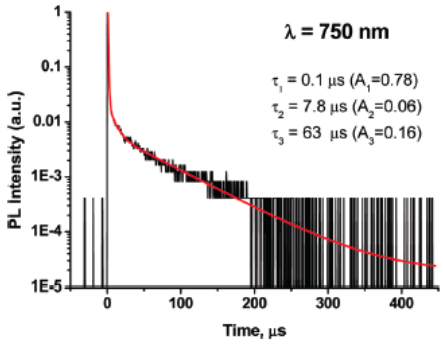

Figure 7. PL decay kinetics (λ_{reg} = 750 nm) of Si NPs produced by nanosecond LA in chloroform (after post-treatment).

Gaussian (for wide band at 490 cm^{-1}). The origin of this amorphous silicon and its relation to Si nanocrystals is not yet understood. One of the possible explanations is that the amorphous Si can form a noncrystalline shell around the Si crystalline core, as has been found for Si NPs produced by LA in an inert gas atmosphere.[15] Indeed, some of our HRTEM images can be interpreted in favor of the presence of some amorphous layer around a crystalline core, but in most cases a distinct borderline of individual crystalline Si NPs is observed. Thus, we preliminarily suggest that the observed amorphous phase of silicon is likely produced independently and my be placed separately from Si NCs.

Luminescence properties of the obtained Si NPs have been also studied. It should be noted that, immediately after ultrasonic/HF post-treatment, Si NPs in hexane suspension do not show any remarkable PL. However, photoluminescence appears if hexane (with HF trace) is replaced by any liquid (in which dissolved oxygen of air is present) or hexane solution is deposited on subtract and kept on air. In both cases the PL is observed in the visible−near IR region, and its spectrum is shown in Figure 6 for the case of isopropanol suspension. The spectrum is rather broad (from ~400 up to 900 nm) with a maximum near 500 nm.

In addition to Si NP luminescence spectra, the luminescence decay kinetics have been also measured. PL spectra of different Si structures can be rather similar, so that Si nanocrystals, Si−O related surface states, oxygenated amorphous Si, and oxygen defects in Si dioxide can exhibit PL spectra in the same spectral region. PL decay kinetics can give additional information and shed further light on the nature of the emitting states,[16] at least to distinguish between optically forbidden and optically allowed transitions.

Decay kinetics of the PL presented in Figure 6 was measured for wavelengths of 600, 675, and 750 nm. Representative PL decay kinetics obtained for 750 nm is shown in Figure 7. We applied the three-exponential decay model (red line in Figure 7)

$$I_{PL}(t) = A_1 \exp(-t/\tau_1) + A_2 \exp(-t/\tau_2) + A_3 \exp(-t/\tau_3) \quad (2)$$

(τ_i and A_i are decay lifetimes and their relative amplitudes) for fitting experimental decay kinetics (black line). For the kinetics measured at 750 nm, the following lifetimes and their amplitudes were obtained: $\tau_1 = 0.1\ \mu s$ ($A_1 = 0.78$), $\tau_2 = 7.8\ \mu s$ ($A_2 = 0.06$), $\tau_3 = 63\ \mu s$ ($A_3 = 0.16$). It was found that with detection wavelength decrease the decay profile remains approximately the same, but the short-lived signal becomes more prevalent, so that for $\lambda = 675$ nm, lifetimes (relative amplitudes) were found to be $\tau_1 = 0.08\ \mu s$ ($A_1 = 0.87$), $\tau_2 = 6.3\ \mu s$ ($A_2 = 0.05$), and $\tau_3 = 34\ \mu s$ ($A_3 = 0.08$) and for $\lambda = 600$ nm $\tau_1 = 0.1\ \mu s$ ($A_1 = 0.95$) and $\tau_2 = 14\ \mu s$ ($A_2 = 0.05$), $A_3 = 0$.

Thus, as shown in Figure 6, the luminescence spectrum is heterogeneous and includes the emission of at least two centers with different lifetimes. Preliminarily, we suggest that emission centers with long-lived luminescence (lifetimes of tens of microseconds) may belong to the excitonic luminescence of silicon nanocrystals passivated by oxygen: in this case, yellow-red PL is usually observed possessing submillisecond lifetimes.[17] As for the nature of the luminescence with a short lifetime (less than 100 ns, time resolution of the setup), we found that relative intensity of the short-lived PL grows with time on the time scale of hours and days as a result of interaction with air that suggests the Si-oxide origin of this PL, the more so as Si−O related PL is usually short lived (nanosecond time scale).[18]

These assumptions about the origin of the two components of luminescence are in agreement with the behavior of Si NP PL in the presence of hydrofluoric acid. Indeed, HF removes silicon oxides that should result in quenching the short-lived photoluminescence. On the other hand, replacement of the oxygen passivation of silicon nanocrystals which emit long-lived PL on hydrogen passivation in the presence of HF should significantly change the PL properties. Indeed, unlike Si NPs passivated by oxygen, hydrogen-passivated silicon nanocrystals exhibit PL with nanosecond lifetimes, and this PL is usually observed in a different (blue-green) region.[19,20] In any case, the long-lived luminescence component belonging to oxygen-passivated Si NPs should be quenched in the presence of HF.

On the other hand, it is known from the literature that Si NCs passivated by chlorine show luminescence in the 1.8−3.1 eV spectral region,[21] which agrees well with the region of the emission of our Si NPs (in our case chlorine atoms can be released from chloroform during the laser ablation). Therefore, the origin of the observed PL and its relation to the Si NC surface require further investigation.

4. CONCLUSIONS

Thus, the results obtained by the methods of TEM, HRTEM, and Raman light scattering indicate that small (3−5 nm in diameter) Si nanocrystals are produced in a two-stage process including (1) nanosecond laser ablation of the Si target in an organic liquid (chloroform) that results in formation of big composite polycrystalline particles (about 20−100 nm average diameter) and (2) ultrasonic post-treatment of Si NPs in the

presence of HF. The post-treatment is responsible for disintegration of the composite Si particles, release of small individual nanocrystals, and likely, reduction of their size due to HF-induced etching of the Si oxide surface.

AUTHOR INFORMATION

Corresponding Author

*E-mail: vladimir.chyrvony@uv.es. Phone: (+34) 96 354 4050. Fax: (+34) 96 354 3633.

ACKNOWLEDGMENT

This work was supported through the Spanish MCINN and Generalitat Valenciana projects Grant Nos. TEC-2008-06756-C03-03 and PROMETEO/2009/074. The Raman spectra were measured by using equipment of the Center of User's Facilities of Lomonosov Moscow State University.

REFERENCES

(1) Walters, R. J.; Bourianoff, G. I.; Atwater, H. A. *Nat. Mater.* **2005**, *4*, 143.

(2) Tiwari, S.; Rana, F.; Hanafi, H.; Hartstein, A.; Crabbe, E. F.; Chan, K. *Appl. Phys. Lett.* **1996**, *68*, 1377.

(3) (a) Stupca, M.; Alsalhi, M.; Al Saud, T.; Almuhanna, A.; Nayfeh, M. H. *Appl. Phys. Lett.* **2007**, *91*, 063107. (b) Timmerman, D.; Izeddin, I.; Stallinga, P.; Yassievich, I. N.; Gregorkiewich, T. *Nat. Photonics* **2008**, *2*, 105.

(4) (a) Kovalev, D.; Gross, E.; Künzner, N.; Koch, F.; Timoshenko, V. Y.; Fujii, M. *Phys. Rev. Lett.* **2002**, *89*, 137401. (b) Chirvony, V.; Chyrvonaya, A.; Ovejero, J.; Matveeva, E.; Goller, B.; Kovalev, D.; Huygens, A.; de Witte, P. *Adv. Mater.* **2007**, *19*, 2967.

(5) (a) Park, J.-H.; Gu, L.; von Maltzahn, G.; Ruoslahti, E.; Bhatia, S. N.; Sailor, M. J. *Nat. Mater.* **2009**, *8*, 331. (b) He, Y.; Kang, Z.-H.; Li, Q.-S.; Tsang, C. H. A.; Fan, C.-H.; Lee, S.-T. *Angew. Chem., Int. Ed.* **2009**, *48*, 128.

(6) Kabashin, A. V.; Meunier, M. *J. Appl. Phys.* **2003**, *94*, 7941.

(7) (a) Dolgaev, S. I.; Simakin, A. V.; Voronov, V. V.; Shafeev, G. A.; Bozon-Verduraz, F. *Appl. Surf. Sci.* **2002**, *186*, 546. (b) Kazakevich, P. V.; Simakin, A. V.; Voronov, V. V.; Shafeev, G. A. *Appl. Surf. Sci.* **2006**, *252*, 4373. (c) Svrcek, V.; Sasaki, T.; Shimizu, Y.; Koshizaki, N. *Appl. Phys. Lett.* **2006**, *89*, 213113. (d) Du, X.-W-; Qin, W.-J.; Lu, Y.-W.; Han, X.; Fu, Y.-S.; Hu, S.-L. *J. Appl. Phys.* **2007**, *102*, 013518. (e) Umezu, I.; Minami, H.; Senoo, H.; Sugimura, A. *J. Phys. Conf. Ser.* **2007**, *59*, 392. (f) Svrcek, V.; Sasaki, T.; Shimizu, Y.; Koshizaki, N. *J. Laser Micro/Nanoeng.* **2007**, *2*, 15. (g) Takada, N.; Sasaki, T.; Sasaki, K. *Appl. Phys. A: Mater. Sci. Process.* **2008**, *93*, 833. (h) Yang, S.; Cai, W.; Zeng, H.; Li, Z. *J. Appl. Phys.* **2008**, *104*, 023516. (i) Svrcek, V.; Sasaki, T.; Katoh, R.; Shimizu, Y.; Koshizaki, N. *Appl. Phys. B: Laser Opt.* **2009**, *94*, 133.

(8) Rioux, D.; Laferriere, M.; Douplik, A.; Shah, D.; Lilge, L.; Kabashin, A. V.; Meunier, M. M. *J. Biomed. Opt.* **2009**, *14*, 021010.

(9) Yang, S.; Cai, W.; Zhang, H.; Xu, X.; Zeng, H. *J. Phys. Chem. C* **2009**, *113*, 19091.

(10) Sun, X.-H.; Li, C.-P.; Wong, N.-B.; Lee, C.-S.; Lee, S.-T.; Teo, B.-K. *J. Am. Chem. Soc.* **2002**, *124*, 14856.

(11) (a) Kabashin, A. V.; Meunier, M.; Kingston, C; Luong, J. H. T. *J. Phys. Chem. B* **2003**, *107*, 4527. (b) Sylvestre, J.-P.; Poulin, S.; Kabashin, A. V.; Sacher, E.; Meunier, M.; Luong, J. H. T. *J. Phys. Chem. B* **2004**, *108*, 16864.

(12) Kobayashi, M.; Liu, S.-M.; Sato, S.; Yao, H.; Kimura, K. *Jpn. J. Appl. Phys.* **2006**, *45*, 6146.

(13) (a) Zi, J.; Zhang, K.; Xie, X. *Phys. Rev. B* **1997**, *55*, 9263. (b) Paillard, V.; Puech, P.; Laguna, M. A.; Carles, R.; Kohn, B.; Huisken, F. *J. Appl. Phys.* **1999**, *86*, 1921.

(14) Maley, N.; Beeman, D.; Lannin, J. S. *Phys. Rev. B* **1988**, *38*, 10611.

(15) Orii, T.; Hirasawa, M.; Seto, T. *Appl. Phys. Lett.* **2003**, *83*, 3395.

(16) Hybertsen, M. S. *Phys. Rev. Lett.* **1994**, *72*, 1514.

(17) Wilson, W.; Szajovsky, P.; Brus, L. *Science (Washington, D.C.)* **1993**, *262*, 1242.

(18) Min, K. S.; Shcheglov, K. V.; Yang, C. M.; Atwater, H. A.; Brongersma, M. L.; Polman, A. *Appl. Phys. Lett.* **1996**, *69*, 2033.

(19) Belomoin, G.; Rogozhina, E.; Therrien, J.; Braun, P. V.; Abuhassan, L.; Nayfeh, M. H.; Wagner, L.; Mitas, L. *Phys. Rev. B* **2002**, *65*, 193406.

(20) Wolkin, M. V.; Jorne, J.; Fauchet, P. M.; Allan, G.; Delerue, C. *Phys. Rev. Lett.* **1999**, *82*, 197.

(21) Santana, G; Monroy, B. M.; Ortiz, A.; Huerta, L.; Alonso, J. C.; Fandiño, J.; Aguilar-Hernandez, J.; Hoyos, E.; Cruz-Gandarilla, F.; Contreras-Puentes, G. *Appl. Phys. Lett.* **2006**, *88*, 041916.

PUBLICACIÓN III

Laser ablation of a silicon target in chloroform: formation of multilayer graphite nanostructures

K. Abderrafi, R. García-Calzada, J.F. Sánchez-Royo, V. Chirvony, S. Agouram, R. Abargues, R. Ibáñez, and J.P. Martínez-Pastor

J. Phys. D: Appl. Phys. 46, 135301 (9 pp) (2013)

J. Phys. D: Appl. Phys. **46** (2013) 135301 (9pp) doi:10.1088/0022-3727/46/13/135301

Laser ablation of a silicon target in chloroform: formation of multilayer graphite nanostructures

Kamal Abderrafi[1], Raúl García-Calzada[1], Juan F Sanchez-Royo[1], Vladimir S Chirvony[1], Saïd Agouram[2], Rafael Abargues[3], Rafael Ibáñez[1] and Juan P Martínez-Pastor[1,2]

[1] UMDO, Instituto de Ciencias de los Materiales, Universidad de Valencia, PO Box 22085, 46071 Valencia, Spain
[2] Dpt. Física Aplicada, Universidad de Valencia, Dr Moliner 50, 46100 Burjassot (Valencia), Spain
[3] Intenanomat SL, C/Catedratico José Beltrán 2, 46980 Paterna (Valencia), Spain

E-mail: Juan.Mtnez.Pastor@uv.es

Received 20 October 2012, in final form 25 January 2013
Published 26 February 2013
Online at stacks.iop.org/JPhysD/46/135301

Abstract
With the use of high-resolution transmission electron microscopy, selected area electron diffraction and x-ray photoelectron spectroscopy methods of analysis we show that the laser ablation of a Si target in chloroform ($CHCl_3$) by nanosecond UV pulses (40 ns, 355 nm) results in the formation of about 50–80 nm core–shell nanoparticles with a polycrystalline core composed of small (5–10 nm) Si and SiC mono-crystallites, the core being coated by several layers of carbon with the structure of graphite (the shell). In addition, free carbon multilayer nanostructures (*carbon nano-onions*) are also found in the suspension. On the basis of a comparison with similar laser ablation experiments implemented in carbon tetrachloride (CCl_4), where only bare (uncoated) Si nanoparticles are produced, we suggest that a chemical (solvent decomposition giving rise to highly reactive CH-containing radicals) rather than a physical (solvent atomization followed by carbon nanostructure formation) mechanism is responsible for the formation of graphitic shells. The silicon carbonization process found for the case of laser ablation in chloroform may be promising for silicon surface protection and functionalization.

(Some figures may appear in colour only in the online journal)

1. Introduction

Pulsed laser ablation of solid targets immersed in liquid (pulsed laser ablation in liquid, PLAL) is a rapidly growing technology, which enables the production of colloidal nanometre-sized particles. Most widely investigated is PLAL in water, but, nevertheless, many papers on laser ablation in organic liquids have recently appeared [1–7]. This is caused by the general interest in studying the formation of nanoparticles (NPs) in different liquids as well as by practical needs, for instance for PLAL-induced NP functionalization by ligands which are soluble only in organic solvents [8, 9]. On the one hand, the PLAL technique is commonly used to produce Si NPs, given the applications envisaged for Si quantum dots in photovoltaics [10–13], as the most important. In order to form the active layer, Si nanocrystals are generated by physical/physico-chemical methods (sputtering, PECVD, etc) in high bandgap materials (SiC, SiO_2, Si_3N_4, etc) [10–12], or prepared by wet chemistry as polymer blends [13] and inks [14, 15], where Si nanocrystals are functionalized with appropriate organic ligands. The size of Si QDs has a significant impact on their optical properties due to size confinement, multiexciton generation being the most important one [16]. On the other hand, the surface chemistry of semiconductor NPs, particularly

silicon, can lead to new functionalities (device patterning, catalysis, hydrogen storage, etc) [17–19], other than new ink formulations.

The interaction of liquid medium with NPs newly synthesized by PLAL is often assumed to be negligible and, therefore, non-destructive with regard to the liquid. However, for many organic (hydrocarbon) liquids this suggestion is found to be incorrect, even when only moderate energies of the exciting laser pulse are used. In particular, it was for the first time revealed by Amendola *et al* that the laser ablation of an Au target in toluene using 9 ns 1064 nm excitation pulses is accompanied by the formation of a multilayer graphite shell around Au NPs [1], the shell being a product of toluene destruction. It was found more recently that PLAL of a Si target in ethanol with the use of 1064 nm excitation pulses of 10 ns [2] and 35–1000 fs [3] duration results in the formation of not only Si, but also of SiC nanocrystals. In another work, the formation of large-sized (hundreds of nanometres) hollow carbon shells and fullerene-like carbon spheres was detected as a result of long-time laser ablation of a Si target in toluene with the use of 1064 nm, 10 ns excitation pulses [4]. The first systematic study was recently performed to investigate the dependence of the efficiency of formation of a graphite shell around Si nanocrystals during PLAL (1064 nm, 5 ns pulse excitation) on the nature of the liquid used (H_2O, ethanol, 2-propanol, hexane, octane, octadecene, tryoctineamine, toluene), and toluene was found to be the medium in which production of graphite shell is the most efficient [5]. Nevertheless, the mechanism of formation of such carbon structures (multilayer graphite shells around NPs, fullerene-like carbon spheres, SiC crystals) needs to be studied.

In this investigation, we show that a long-time laser ablation (40 ns, 355 nm laser pulses) of a Si target in chloroform ($CHCl_3$) results in the formation of (i) multi-crystalline NPs composed of small (5–10 nm) Si and SiC mono-crystallites, (ii) multilayer graphite shells covering the multi-crystalline NPs and (iii) free carbon multilayer nanostructures (onion-like carbon or carbon nano-onions). On the basis of a comparison of the efficiency of formation of carbon nanostructures in $CHCl_3$ versus CCl_4 by laser ablation (this work) and by ultrasound treatment reported in our previous work [7], we suggest that a chemical (solvent decomposition giving rise to highly reactive CH-containing radicals) rather than a physical (solvent atomization followed by carbon nanostructure formation) mechanism is responsible for graphitic shell formation.

It is worth noting that in our recent work [7] we described a two-step process developed to produce small (a few nm) Si nanocrystals in colloidal suspension consisting of (1) a short-time (5 min) PLAL of a Si target in chloroform and (2) a long-time (60–90 min) ultrasound treatment of the suspension in the presence of HF that resulted in a disintegration of the initial big polycrystalline Si NPs to a few nm Si monocrystallites. No carbon nanostructures were found in these NPs, most likely because the Si target was irradiated for a relatively short time that prevented secondary ablation of produced Si NPs. In contrast to the previous work, here we use a long-time (60 min) PLAL process that enables us to achieve high concentrations of Si NPs in the suspension so that the excitation light is mainly absorbed by these suspended NPs that results in thermal reactions with a liquid on their surface.

2. Experimental methods

A p-type Cz-silicon wafer of (1 0 0) plane with a resistivity of 10–20 Ω cm was first ultrasonically rinsed with deionized water and then ethanol for 1 h. The cleaned silicon wafer was used as a target immersed in a liquid medium ($CHCl_3$ or CCl_4, from Aldrich without further purification, 20 ml in an open glass vessel) and irradiated with the third harmonic of a pulsed Nd : YVO_4 laser (355 nm, 40 ns pulse duration, 5 kHz repetition rate) for 60 min. The laser beam was focused by a lens having a focal length of 60 mm on the silicon target surface with a spot of about 30 μm diameter giving a power density per pulse of $\sim$40 J cm^{-2}. The height of the liquid above the target surface was 5 mm. The solution was continuously stirred during laser irradiation. The laser beam scanned the target over an area of 56 mm^2 by means of an electro-optical beam deflector. A brownish colour appeared soon for the liquid and was enhanced with increase in irradiation time. As a control test, the $CHCl_3$ solution was irradiated without any target under identical experimental conditions. In this case, the solvent did not change its colour as a result of the laser irradiation. PLAL experiments in CCl_4 were also implemented for a comparison.

The suspensions produced during PLAL experiments were examined by transmission electron microscopy (TEM) with a JEOL-1200EX microscope and by high-resolution TEM (HRTEM) with a field emission gun (FEI), Tecnai G^2 instrument, which were operated at 100 kV and 200 kV, respectively. The suspensions were dropped on carbon-coated TEM copper grids (300 mesh) until the solvent was completely evaporated at room temperature before transferring the grid with NPs onto the microscope. The size distribution of NPs was determined by measuring 500–600 isolated NPs in several TEM images.

X-ray photoelectron spectroscopy (XPS) measurements of the PLAL-produced NPs were made in an ultrahigh vacuum system ESCALAB 210 (base pressure 1.0×10^{-10} mbar) from Thermo VG Scientific. The NPs in the suspension were dropped on a Cu substrate just before the XPS measurements. The measurements were made over an area of 1 mm^2 of the densely covered Cu substrate. Photoelectrons were excited by the Mg Kα line (1253.6 eV).

3. Results and discussion

The irradiation of a silicon target immersed in chloroform ($CHCl_3$) by nanosecond UV pulses results in the formation of a stable colloidal suspension with a brownish colour. Figure 1 shows a TEM micrograph of the sample collected in the grid after evaporation of chloroform. As the size distribution analysis shows (not presented), PLAL of a Si target in chloroform results in the synthesis of NPs of nearly spherical shape with a broad diameter distribution between 20 and 120 nm with the distribution maximum around 50–80 nm.

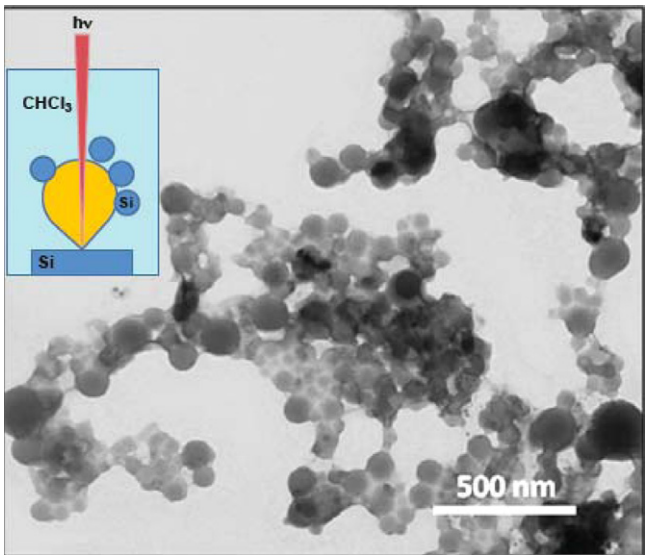

Figure 1. TEM micrograph of NPs produced by PLAL of a silicon target immersed in chloroform.

HRTEM study of the PLAL products allows shedding light on the chemical content and morphology of the structures synthesized in course of PLAL in chloroform. Figure 2(*a*) shows the HRTEM micrograph of a part of one individual NP. The NP presents a polycrystalline structure composed of mono-crystallites (separately analysed in figures 2(*b*)–(*d*)) with mean diameters in the range 5–10 nm. The micrograph shows the coexistence of two types of mono-crystallites with lattice fringe spacings (indicated by parallel lines in figures 2(*b*) and (*d*)) of 2.540 Å (minor contribution) and 3.167 Å (dominant), respectively. These values agree well with the (1 1 1) lattice constants for silicon carbide and silicon, respectively, in standard diamond crystal structures.

The selected area electron diffraction (SAED) analysis, which gives information about a large area (more than 100 × 100 nm^2 that includes many mono-crystallites inside one polycrystalline NP), indicates the coexistence of a relatively weak ring corresponding to $SiC_{(2\,0\,0)}$ and $SiC_{(1\,1\,1)}$ with the rings of $Si_{(1\,1\,1)}$, $Si_{(2\,2\,0)}$ and $Si_{(3\,1\,1)}$, as observed in figure 2(*e*) that includes the assignment of such rings.

The fast Fourier transform (FFT) pattern, which is also known as a digital electron diffraction pattern (figure 2(*c*)) of the selected NP (figure 2(*b*)), shows well-defined spots. The identification and indexation of the spots can be ascribed to SiC nanocrystallites in cubic structure in the [1 1 0] zone axis. The measured interplanar angle and interplanar distance are in good agreement with the calculated values of cubic SiC space group F-43m (JCPDS: 1-75-254). Since FFT offers information about a small selected zone of the HRTEM image, the well-defined spots in the FFT pattern, in comparison with SAED, evidence that the small NPs constituting a big polycrystalline NP possess the structure close to the mono-crystalline one.

As one can see in figure 3(*a*), the surface of an individual Si NP obtained by PLAL in chloroform is coated with several layers of a material, the measured interplane spacing for which, using the digital micrograph software, was ranging from 3.3 to 3.5 Å. It is known that the distance of 3.4 Å is a characteristic of bulk graphite interplane spacing. We believe, therefore, that the multilayer structure observed in figure 3(*a*) along the external border of the NP is a multilayer graphite shell formed, as we suggest, due to decomposition of chloroform under the high-temperature conditions of the laser ablation (possible mechanisms will be discussed below). Such shells are formed around practically all Si polycrystalline NPs produced in our PLAL experiments in chloroform (figure 1).

We found that the graphite shells are not the exclusive carbon nanostructures formed during the PLAL experiments in chloroform. In addition, multilayer structures of another type, which are not connected to the polycrystalline Si NPs (figure 2(*a*)), are observed in the space between them. These multilayer nanostructures demonstrate spherical or onion-like shape with a diameter smaller than 10 nm (the size of some nanostructures is indicated by arrows in figure 3(*b*)). At the same time, the distance between the layers in these nanostructures is the same as that in the case of graphite shells (3.4 Å) that evidences in favour of their carbon nature. Such carbon nanostructures are known in the literature as carbon nano-onions (CNOs), or onion-like carbon (OLC) [20]. As we observed experimentally, they are easily shrunk, collapsed or damaged by the electron beam under TEM. It is interesting to note that, following the literature [21], OLCs easily aggregate in solution that correlates with our observations: carbon nanostructures tend to aggregate rather than to be distributed homogeneously in the suspension (and in films on TEM grids).

Therefore, NPs produced by UV ns PLAL of a Si target in chloroform possess three main peculiarities: (i) they are polycrystalline and are composed mainly of Si monocrystallites with an inclusion of silicon carbide (SiC) monocrystallites; (ii) the polycrystalline NPs are wrapped by a multilayer graphite shell; (iii) a large number of free CNOs are also produced during the ablation process.

In this study, the selection of chloroform as a liquid for ablation was inspired by the recent investigation [7], in which the formation of graphite multilayer structures around nano-silicon templates was achieved by an *ultrasound treatment* of silicon nanodots/nanowires in different organic liquids: the process was found to be the most efficient in the case of short halogen-substituted hydrocarbons, such as $CHCl_3$ and CH_2Cl_2, in a comparison with halogen-free hydrocarbons such as toluene or hexane. We performed our own qualitative laser ablation experiments and showed that, similarly to the case of ultrasound treatment [7], in the case of laser ablation of Si target the formation of a graphite multilayer shell around Si NPs is more efficient in chloroform than in toluene and considerably more efficient than in hexane (data not shown).

Following the choice made in [7] for the case of an ultrasound treatment, we used CCl_4 as a counterpart liquid for laser ablation experiments. In fact, the use of CCl_4 instead of $CHCl_3$ will enable one to check whether the absence of C–H group can change the efficiency of the graphitic shell formation or not, the two molecules being different only by one atom (chlorine instead of carbon). Surprisingly, under the same ablation conditions that were used for the case of $CHCl_3$, in CCl_4 we did not observe the formation of multilayer shells around the silicon-based core (figure 4). Thus, the observation

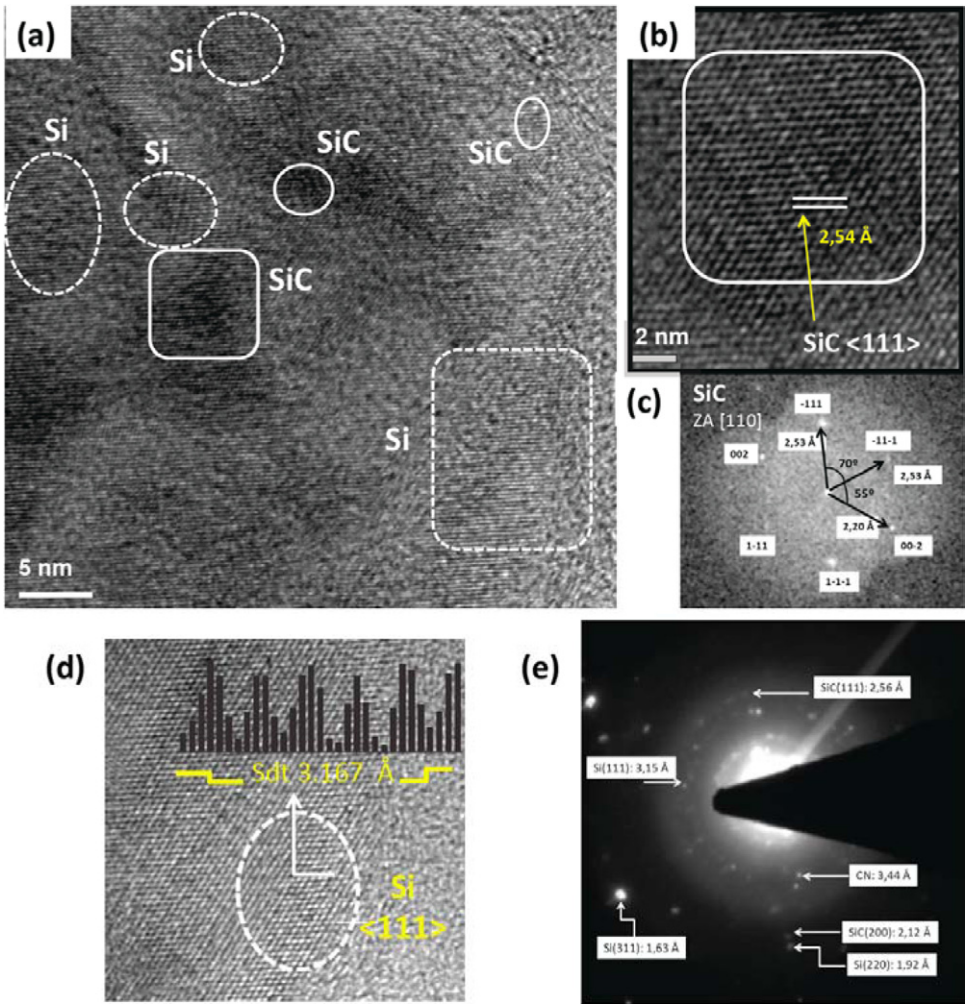

Figure 2. (*a*) HRTEM micrograph of a part of a single polycrystalline NP consisting of Si and SiC mono-crystallites, which are encircled by dashed and solid lines, respectively. A zoom of a SiC nanocrystallite is depicted in (*b*), together with its FFT analysis in (*c*). In (*d*) a zoom corresponding to a Si ⟨1 1 1⟩ nanocrystallite is presented including the details of the plane period (3.167 Å). Finally, the SAED pattern corresponding to the NP in micrograph (*a*) is included as (*e*).

evidences in favour of a crucial role of CH group (likely in the form of CH radicals) in the formation of laser-ablation-induced graphitic multilayer structures.

Additional information confirming the different chemical content of the products of PLAL of the Si target in $CHCl_3$ and CCl_4 can be drawn from the results of our XPS investigation (figure 5).

The XPS data confirm a significant difference in the degree of interaction of Si NP surface with carbon products, formed due to liquid decomposition, in the case of $CHCl_3$ and CCl_4 (spectra 1 and 2, respectively, in figure 5). First of all, it concerns the Si 2p core spectra of Si NPs (figure 5(*a*)). In these spectra the XPS signal is composed of several Si 2p core levels; each of them corresponds to Si atoms with a different chemical environment. The Si 2p peak with the lowest binding energy (99.2 eV) appears to be detected only for NPs produced in CCl_4. The other two Si 2p peaks resolved at 101.4 and 103.7 eV are detected for Si NPs produced in both liquids. Going from lower to higher binding energy, the first Si 2p peak (about ∼99 eV) is usually attributed to non-oxidized Si atoms in the Si(0) state and the next Si 2p peak at ∼101 eV to Si atoms in the Si(2+) state in a SiC, SiO*x* or SiCl-like environment [22–25]. The Si 2p appearing at the highest binding energy (∼103.5 eV) is related to Si atoms in a SiO_2-like environment.

Therefore, the main peak at ∼99 eV observed for the case of Si NPs produced in CCl_4 belongs to the Si(0) oxidation state of silicon, that is it belongs to silicon atoms participating in Si–Si bonds of the silicon crystal lattice. It reveals that the surface of Si NPs produced in CCl_4 is practically *not functionalized* by carbon or any other atoms. On the other hand, in the case of Si NP synthesis in $CHCl_3$, Si atoms in the Si(0) state are not observed at all on the Si NP surface. The Si 2p peak resolved at 101.4 eV can be assigned to the Si(2+) state and corresponds to SiC_x, $SiCl_x$ or SiO_x environment. Since this band is the most intense one for the case of Si NPs produced in $CHCl_3$, and the band at ∼99 eV is absent in this case, it implies that the surface Si atoms (maximum 2–3 nm in depth of the Si NP surface—the depth of escape of photoelectrons) in the case of Si NPs produced in $CHCl_3$ are bound to C (Si–C bond), Cl (Si–Cl bond) or O (Si–O bond) atoms. The Si 2p peak at 103.7 eV can be, more certainly, assigned to the Si(4+) state that corresponds to the SiO_2 environment.

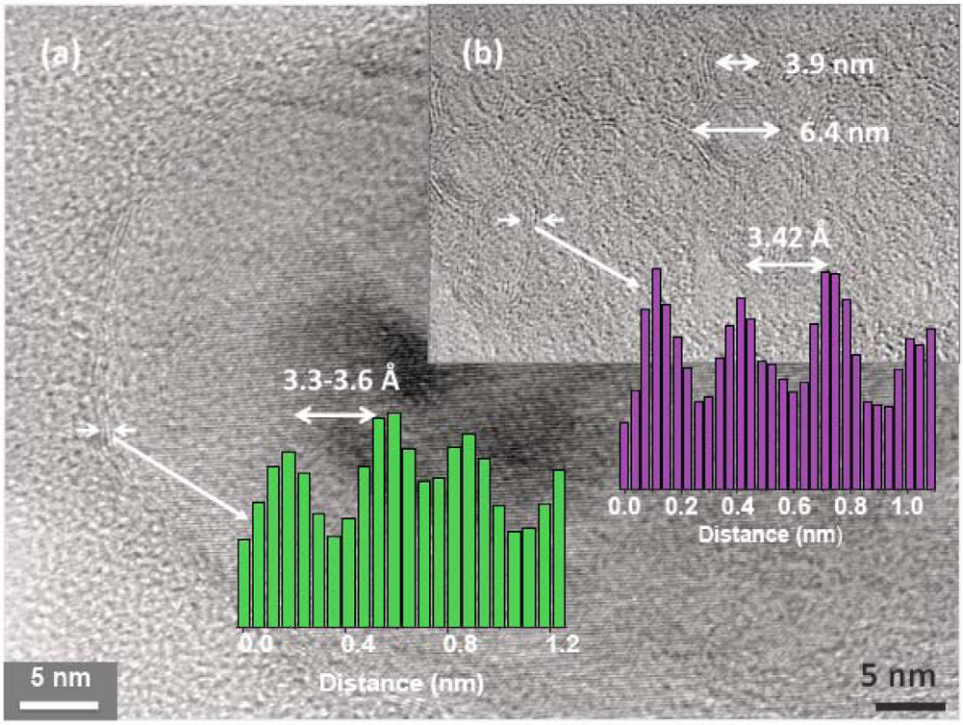

Figure 3. (*a*) HRTEM micrograph of a single polycrystalline NP covered by a multilayer carbon shell. (*b*) HRTEM image of CNOs detected in a space between the core–shell NPs. The results of the interlayer distance determination using the digital micrograph software are marked by green and blue colours for graphite and CNO, respectively.

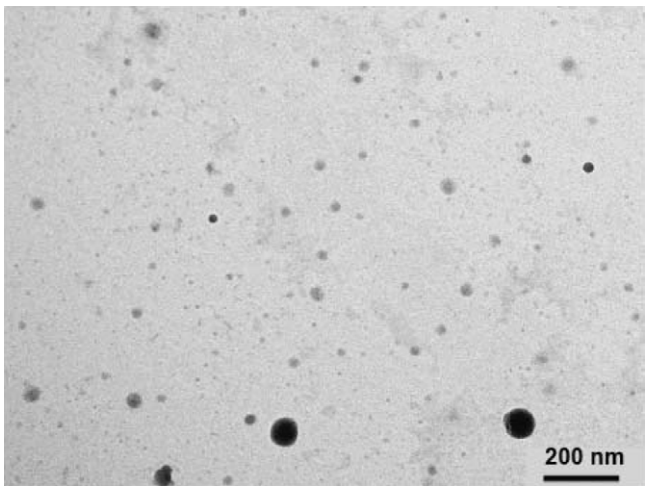

Figure 4. TEM micrograph of Si NPs produced by PLAL of a silicon target in CCl_4 under ablation conditions identical to those applied in the case of PLAL in $CHCl_3$.

Figure 5(*b*) shows the XPS spectra of the C 1s level measured for Si NPs produced by ns PLAL in chloroform and in carbon tetrachloride. In these spectra, a main C 1s peak is observed at 284.5 eV for both samples that we attribute to C–C and/or SiC-like bonding. In addition to these peaks, two broad C 1s features appear at higher binding energies (around 286.0 eV) coming from C atoms bonded to more electronegative ones. These electronegative atoms would be expected to be O or Cl. In all cases, O may originate from air molecular oxygen, O_2, dissolved in the liquid.

Therefore, due to an exchange of only one atom (H to Cl) in the chemical formula of the ablation liquid the formation of multilayer carbon shells around Si NP core stops, which is evidenced by both TEM and XPS (Si 2p) data. Nevertheless, in both cases C 1s XPS measurements demonstrate the presence of carbon atoms (see discussion below).

The fact that big polycrystalline Si NPs rather than individual 5–10 nm mono-crystallites occur to be coated with a multilayer graphite shell suggests that the polycrystalline Si core forms first followed by carbon multilayer shell formation around the polycrystalline Si core. To confirm this, we carried out special experiments, in which laser ablation of a Si target in $CHCl_3$ was stopped after the first 60 s of pulsed laser irradiation and the ablation products were analysed by HRTEM. It turned out that large clusters of diameter about 50 nm and irregular shape are produced during this time, the clusters being composed of single crystalline NPs with a size of about 10 nm (figure 6). The formation of any carbon layer and nanostructure is not observed at this initial stage of Si target ablation in chloroform. On the basis of this information we suggest that the transformation of these bare Si nanocrystal clusters of irregular shape into graphite-coated spherical NPs is caused by direct absorption of the excitation laser light by big Si clusters dispersed in the suspension and that the Si clusters serve as a template to form carbon multilayer structures.

On the basis of the data obtained in this work as well as of the literature data [7] we propose the following mechanistic pathway for *the formation of carbon multilayer structures* around the polycrystalline Si NP core as well as of *free multilayer carbon nanostructures* under laser ablation of the Si target in $CHCl_3$. First of all, since a considerable difference is found in the efficiency of the formation of carbon multilayer structures around the polycrystalline Si NP core for ablation

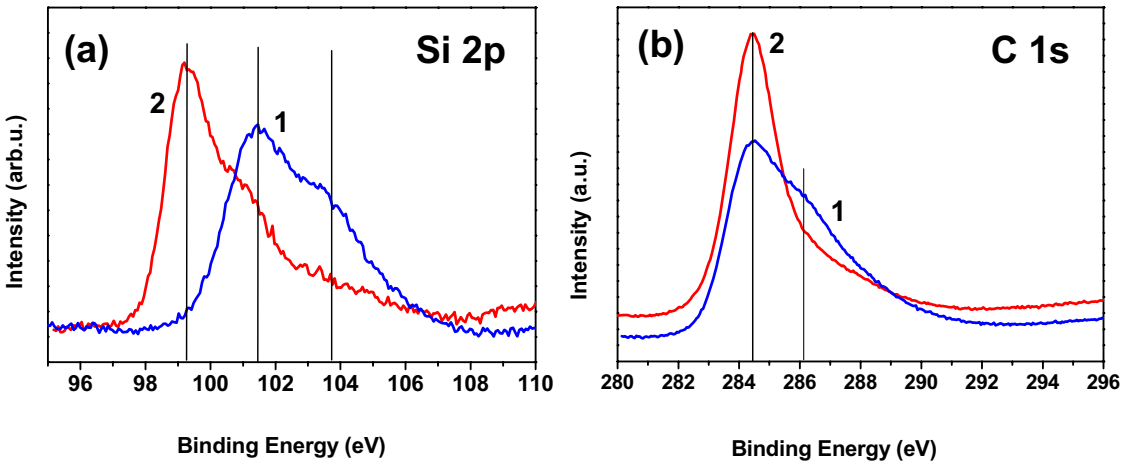

Figure 5. Si 2p (*a*) and C 1s (*b*) XPS spectra of Si NPs produced by ns PLAL in chloroform (1) and carbon tetrachloride (2).

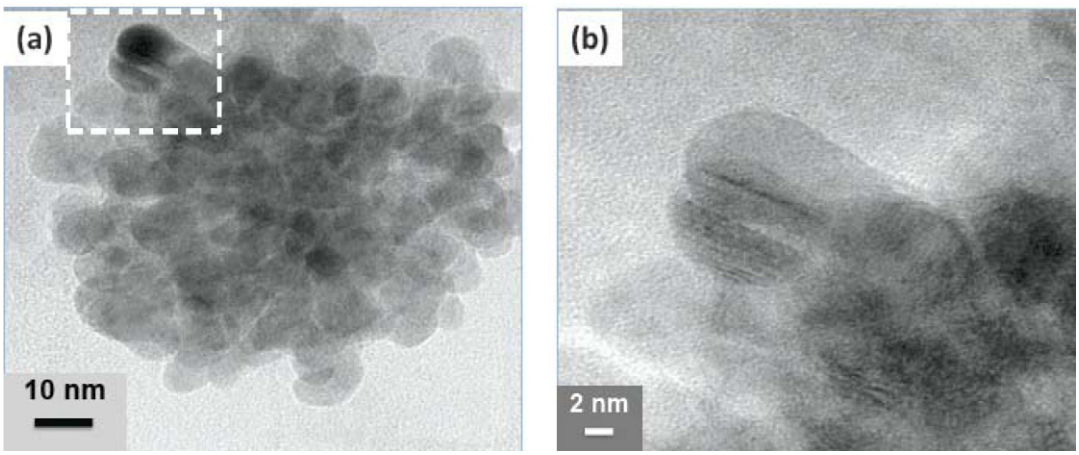

Figure 6. (*a*) HRTEM micrograph of a single polycrystalline NP formed 1 min after the beginning of laser ablation of Si target in chloroform. (*b*) The magnified image of the part of the left micrograph encircled by the white dashed line.

in $CHCl_3$ and CCl_4 (that means that the mechanism of graphitic shell formation depends on the liquid structure), the mechanism has a chemical origin rather than physical. As an example of a physical mechanism of carbon nanostructure formation after laser ablation of a target one can mention the synthesis of fullerenes by laser ablation of graphite where the physical mechanism consists in atomization of graphite in the plasma plume with subsequent formation of carbon layers [26]. In the case of such a *physical* mechanism we could not expect to find a considerable difference in the efficiency of the multilayer carbon shell formation we observe between $CHCl_3$ and CCl_4.

On the other hand, we suggest that such a physical mechanism of hydrocarbon liquid atomization is responsible for the formation of SiC nanocrystals, which are detected by HRTEM (figure 2), at the first stage of laser ablation (this stage is characterized by a low concentration of ablation products when excitation light is absorbed practically by the Si target only). Generally speaking, such SiC nanocrystals should be formed under laser ablation of a Si target in any organic solvent, and even in those cases when multilayer carbon shells are not formed; in fact, this is confirmed by the literature data [2, 3]. In the case of CCl_4 such SiC nanocrystals are responsible for the shoulder around 101 eV in the Si 2p XPS spectrum and, partially, for the peak at 284.5 eV in the C 1s spectrum (figure 5).

Contrary to the above-mentioned physical mechanism of SiC formation, for the formation of multilayer carbon structures around Si NPs as a template, some structural conditions should be fulfilled by ablation liquids: these conditions are fulfilled for $CHCl_3$ but not for CCl_4. We should note here that full identification of these structural requirements is beyond the scope of this paper and will be discussed elsewhere. Nevertheless, below we will propose a qualitative scheme for the carbon multilayer shell formation around the Si NP template.

Thus, the first stage of nanosecond laser ablation of a Si target in organic liquids consists in the formation and coalescence of initially produced Si/SiC clusters to form big Si/SiC NPs, which serve as templates for multilayer carbon nanostructure formation. When the NPs reach a sufficiently big size providing efficient light absorption to increase the NP surface temperature, the high temperature gives rise to two *activation* processes preceding the formation of the Si–C bonds registered by XPS. These processes are the activation of (i) the surface of a silicon NP, and (ii) organic liquid molecules near the Si NP surface (processes 1 and 2, respectively, in scheme 1).

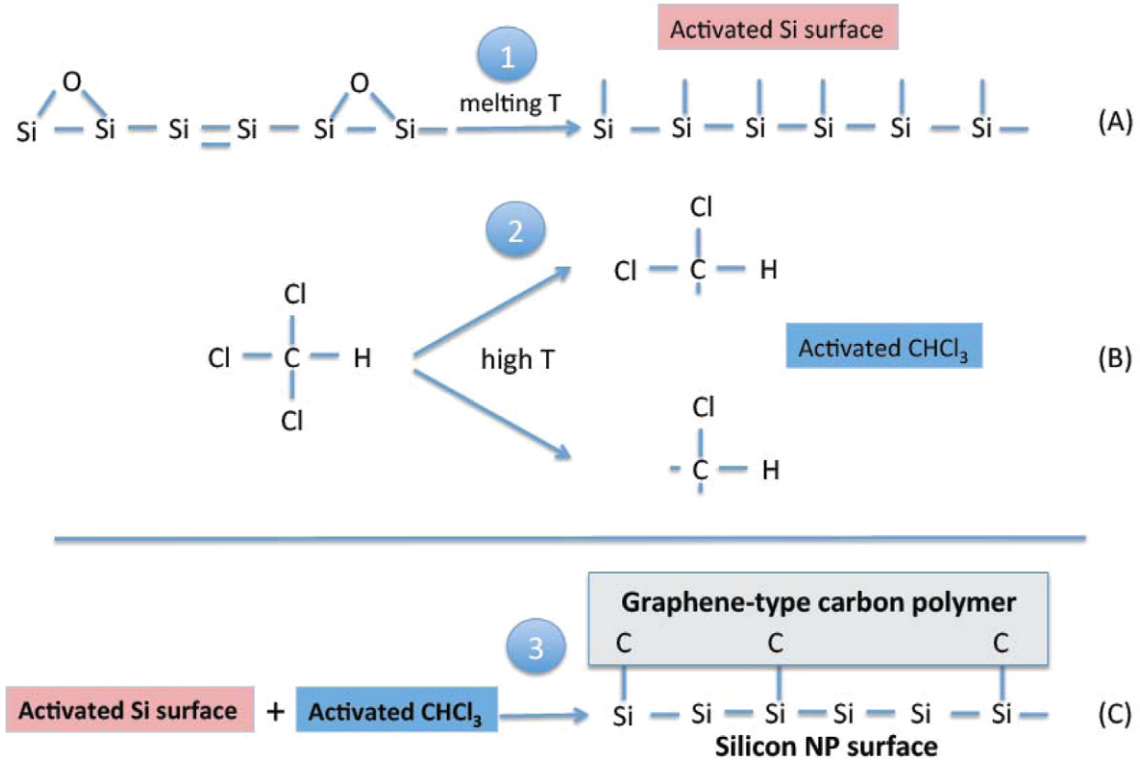

Scheme 1. A sketch schematically describing the suggested mechanism of temperature-induced activation of Si NP surface (process 1) and $CHCl_3$ molecules (process 2) followed by their interaction (process 3) resulting in the formation of a polymeric carbon (graphene-type) layer on the Si surface.

It is worth noting that, in the case of the formation of carbon multilayer structures under ultrasound treatment of Si NPs/NWs [7], Si surface activation was achieved by preliminary etching of Si NPs/NWs with HF that gave rise to a hydrogen-terminated Si surface covered with SiH_x (where $x = 1$–3) species. It was the crucial step because little or no carbon multilayer material was formed on top of Si templates under ultrasound treatment of the as-prepared (that is oxidized) Si NPs/NWs [7]. Under the extreme local temperature within the acoustic cavity the Si–H bond breaks forming a net of extremely reactive Si dangling bonds, which react with the activated molecules of the liquid.

We believe that in the case of laser ablation, the excitation light absorption by big Si NPs in a suspension can ensure activation of the Si NP surface without preliminary surface hydrogenation. It can occur because light absorption by big Si NPs increases the NP surface temperature sufficiently to melt the surface that results in (i) the formation of *Si dangling bonds* on the surface, and (ii) laser-annealing-induced removal of foreign atoms (such as oxygen) from the near-surface region [27]. As an indirect manifestation of the fusion process we can mention the acquisition of more spherical shape by polycrystalline Si NPs during the process of graphitic shell formation as compared with the angular shapes observed at the beginning of the ablation process (figure 6).

Concerning the temperature, which can be achieved on and near the surface of polycrystalline Si NPs due to the absorption of excitation light, we evaluate it qualitatively to be as high as at least about 1500–2000 K. In fact, the polycrystalline Si NP round shape reveals Si NP surface melting as a result of the transformation of the energy of absorbed photons to heat (light absorption efficiency of silicon NPs is very high in the UV region [28, 29]). On the other hand, the melting temperature for Si NPs is between ∼1000 and ∼1700 K (bulk Si melting temperature) depending on the Si NP size [30]. Finally, direct measurements carried out for the case of Si surface ablation in inert gas and O_2 atmospheres at excitation energies ($1.5\,J\,cm^{-2}$) similar to those used in our experiments ($\sim 40\,J\,cm^{-2}$) showed that the temperature of hot Si atoms and SiO molecules is about 2000 K for at least 5 μs after ns laser excitation [31].

The dangling bonds are rather short-lived species and will react with any suitable counterparts (dissolved molecular oxygen or chlorine atoms formed due to $CHCl_3$ destruction) if they do not meet *activated* carbon-containing molecules to form Si–C bonds.

We believe that Si NP heating by laser pulses ensures not only an activation of Si surface by formation of Si dangling bonds, but also, due to a local surrounding temperature increase, an activation of $CHCl_3$ molecules contacting the surface. This temperature increase will initiate $CHCl_3$ dechlorination (because bond dissociation energy is lower for C–Cl as compared with C–H) with formation of chemically active $CHCl_2-$ and CHCl= radicals (the activation process 2 in scheme 1). Importance of these radicals in the formation of graphitic multilayer structures around Si NPs is evidenced by the experimental observations: halogen-free hydrocarbons and hydrogen-free CCl_4 produce little, if any, multilayer carbon nanostructures [5, 7].

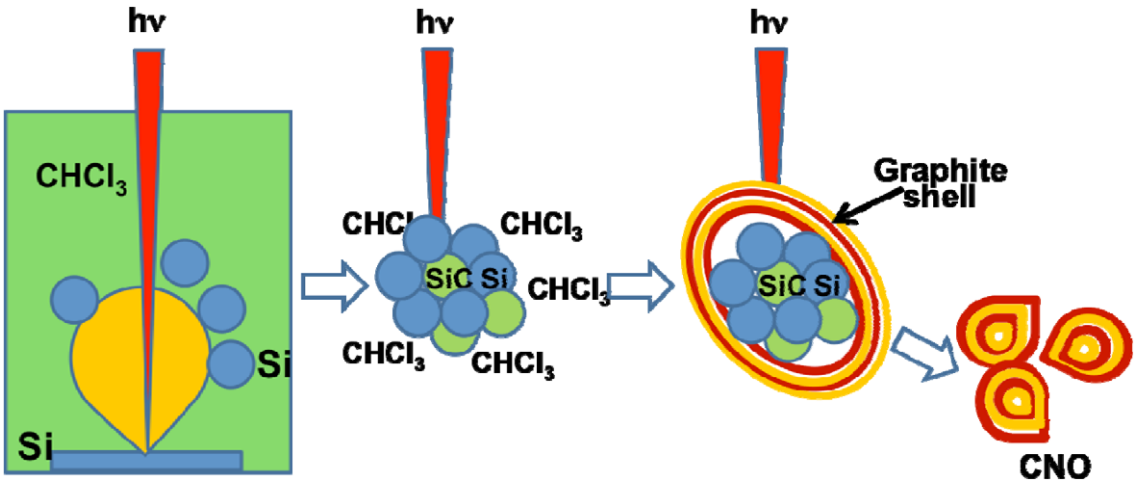

Scheme 2. Schematic diagram illustrating the formation of Si/SiC NPs, graphitic shells around Si/SiC NPs, and free CNOs as a result of long-time silicon target ablation in $CHCl_3$.

After activation of both Si NP surface and molecules of the ablation liquid they interact with each other giving rise to the formation of a (hydro)carbon layer around the Si NP contour (process 3 in the scheme). The layer should not be chemically bound to each Si atom on the surface, as is schematically shown in the scheme. Next, a (hydro)carbon polymeric layer is formed on top of the first one by a similar thermo-activated pathway without formation of valence bonds between the first and second layers.

Thus, we suggest that under the conditions of laser ablation in chloroform, similarly to the case of ultrasonic treatment of chloroform in the presence of dispersed Si nanostructures [7], the hydrocarbon layers (hydrogenized graphite) should initially be formed around Si NPs, the hydrocarbon layers then being transformed into carbon layers as a result of de-hydrogenation due to further action of high temperatures and high pressures. However, this intermediate stage of chloroform carbonization at which hydrocarbon layers are formed on the surface of the Si polycrystalline NPs is not observed in our TEM measurements, probably because this stage is very fast so that the initially formed hydrocarbon layers efficiently lose hydrogen forming more dense carbon layers.

As far as the formation of CNO is concerned, we suggest that this is a secondary process, which is based on the shedding off multilayer graphitic shells formed around the Si NP core. Schematically the suggested pathways of the formation of graphitic shells around Si NPs and free CNOs as a result of silicon target ablation in $CHCl_3$ are shown in scheme 2.

In the mechanistic pathway proposed in this work to describe the formation of graphitic shells (scheme 1) the specific role of CH radicals needs to be investigated in more detail. In this connection, the hypothesis proposed by one of the reviewers of this paper about the possible photochemical origin of the mechanism under discussion is interesting. It is well known in the literature that illumination of hydrogenated Si surface by light with wavelengths shorter than or equal to about 350 nm results in the breaking of Si–H bond and formation of Si dangling bonds, which can easily react with different species, for example with unsaturated hydrocarbons that results in the formation of an aliphatic monolayer on Si [32]. Within the framework of this idea $CHCl_3$ is a source of H for Si surface hydrogenation and subsequent illumination by 355 nm pulses triggers the process of Si–C bond formation. We consider this idea as a working hypothesis for further investigations.

4. Conclusions

The results obtained in this work reveal that the formation of multilayer graphite nanostructures due to decomposition of chloroform molecules near the surface of big Si NPs, which is caused by NP heating as a result of excitation light absorption, occurs through a chemical path. The path consists in the formation of CH radicals and their interaction to form hydrocarbon polymers (as an intermediate product) and then graphite structures. An alternative preliminary hypothesis involves hydrogenation of the Si NP surface by hydrogen released due to thermal decomposition of $CHCl_3$ followed by photochemical cleavage of the Si–H bond under illumination by 355 nm light pulses and an interaction of the formed Si dangling bonds with products of chloroform thermal decomposition. The process of graphitic shell formation under conditions of laser ablation in chloroform can be interesting for Si surface passivation, functionalization and protection.

Acknowledgments

This work was supported through the Generalitat Valenciana Grant PROMETEO/2009/074 and the EU-FP7 NMP-246331 project NanoPV. The authors are grateful to the Central Support Service in Experimental Research (SCSIE) from the University of Valencia for providing HRTEM facilities.

References

[1] Amendola V, Rizzi G A, Polizzi S and Meneghetti M 2005 *J. Phys. Chem.* B **109** 23125
[2] Yang S, Cai W, Zeng H and Xu X 2009 *J. Mater. Chem.* **19** 7119

[3] Kuzmin P G, Shafeev G A, Bukin V V,Garnov S V, Farcau C, Carles R, Warot-Fontrose B, Guieu V and Viau G 2010 *J. Phys. Chem.* C **114** 15266
[4] Yang S, Zeng H, Zhao H, Zhanga H and Cai W 2011 *J. Mater. Chem.* **21** 4432
[5] Huang C C, Chuang K Y, Huang C J, Liu T M and Yeh C S 2011 *J. Phys. Chem.* C **115** 9952
[6] Teo B K, Sun X H, Li C P, Wong N B and Lee S T 2010 *Chem. Mater.* **22** 1297
[7] Abderrafi K, García-Calzada R, Gongalsky M B, Suarez I, Abarques R, Chirvony V, Timoshenko V Yu, Ibáñez R and Martínez-Pastor J P 2011 *J. Phys. Chem.* C **115** 5147
[8] Wagener P, Faramarzi S, Schwenke A, Rosenfeld R and Barcikowski S 2011 *Appl. Surf. Sci.* **257** 7231
[9] Wagener P, Brandes G, Schwenke A and Barcikowski S 2011 *Phys. Chem. Chem. Phys.* **13** 5120
[10] Cho E-C *et al* 2007 *Adv. Optoelectron.* **2007** 69578
[11] Perez-Wurfl I, Hao X, Gentle A, Kim D-H, Conibeer G and Green M A 2009 *Appl. Phys. Lett.* **95** 153506
[12] Löper P *et al* 2012 *Adv. Mater.* **24** 3124
[13] Liu C-Y, Holman Z C and Kortshagen U 2009 *Nano Lett.* **9** 449
[14] Pi X, Li Q, Li D and Yang D 2011 *Sol. Energy Mater. Sol. Cells* **95** 2941
[15] Liu C-Y and Kortshagen U 2010 *Nanoscale Res. Lett.* **5** 1253
[16] Timmerman D, Valenta J, Dohnalová K, de Boer W D A M and Gregorkiewicz T 2011 *Nature Nanotechnol.* **6** 710
[17] Li Y, Lee E J, Cai W, Kim K Y and Cho S O 2008 *ACS Nano* **2** 1108
[18] Zeng J, Su F, Han Y F, Tian Z, Poh C K, Liu Z, Lin J, Lee J Y and Zhao X S 2008 *J. Phys. Chem.* C **112** 15908
[19] Pacula A and Mokaya R 2008 *J. Phys. Chem.* C **112** 2764
[20] Ugarte D 1992 *Nature* **359** 707
[21] Lee J Y, Cho K H, Lim D P, Lee Y B and Lim D S 2007 *Appl. Phys.* A **88** 693
[22] Moulder J F, Stickle W F, Sobol P E and Bomben K D 1992 *Handbook of X-ray Photoelectron Spectroscopy* (Eden Prairie, MN: Perkin–Elmer Corporation Physical Electronics Division)
[23] Hollinger G and Himpsel F J 1983 *Phys. Rev.* B **28** 3651
[24] Hollinger G and Himpsel F J 1983 *J. Vac. Sci. Technol.* A **1** 640
[25] Klauser F, Stijepovic R, Endstrasser N, Jaksch S, Memmel N and Scheier P 2009 *Surf. Sci.* **603** 2999
[26] Kraetschmer W, Lamb L D, Fostiropoulos K and Huffman D R 1990 *Nature* **347** 354
[27] Solis J, Vega F and Afonso C N 1996 *Appl. Phys.* A **62** 197
[28] Beard M C, Knutsen K P, Yu P, Luther J M, Song Q, Metzger W K, Ellingson R J and Nozik A J 2007 *Nano Lett.* **7** 2506
[29] Intartaglia R, Bagga K, Brandi F, Das G, Genovese A, Di Fabrizio E and Diaspro A 2011 *J. Phys. Chem.* C **115** 5102
[30] Schierning G, Theissmann R, Wiggers H, Sudfeld D, Ebbers A, Franke D, Witusiewicz V T and Apel M 2008 *J. Appl. Phys.* **103** 084305
[31] Le H C, Dreyfus R W, Marine W, Sentis M and Movtchan I A 1996 *Appl. Surf. Sci.* **96–98** 164
[32] Cicero R L, Linford M R and Chidsey C E D 2000 *Langmuir* **16** 5688

PUBLICACIÓN IV

A novel method of nanocrystal fabrication based on laser ablation in liquid environment

E. Jiménez, K. Abderrafi, J. Martínez-Pastor, R. Abargues, J.L. Valdés, and R. Ibáñez

Superlattices & Microstructures 43, 487-493 (2008)

Available online at www.sciencedirect.com
ScienceDirect
Superlattices and Microstructures 43 (2008) 487–493
Superlattices and Microstructures
www.elsevier.com/locate/superlattices

A novel method of nanocrystal fabrication based on laser ablation in liquid environment

E. Jiménez*, Kamal Abderrafi, Juan Martínez-Pastor, Rafael Abargues, José Luís Valdés, Rafael Ibáñez

Instituto de Ciencia de los Materiales, Universidad de Valencia, P.O. Box 22085, 46071 Valencia, Spain

Available online 7 September 2007

Abstract

Metal nanoparticles can be prepared by a novel technique that consists of the laser ablation of a solid target immersed in a water solution of a metal salt. Silicon was chosen as the most adequate target to synthesize silver and gold nanoparticles from a water solution of either $AgNO_3$ or $HAuCl_4$. The influence of both the silver nitrate concentrations and the irradiation time of the Si target on the optical properties of the Au and Ag nanoparticles have been investigated. The crystalline nature of the metal nanoparticles has been determined by X-ray diffraction (XRD). Average size and particle size distribution have been measured by means of TEM. The absorbance spectra show the characteristic band of the surface resonant plasmon of silver and gold nanoparticles.

1. Introduction

In the past two decades, metal nanocrystal colloids have attracted much attention from researchers because of their size-dependent electronic and optical properties that arise from the excitation of the free conduction electrons interacting with the electromagnetic radiation. They have been widely exploited for use in photography [1], catalysis [2], biological labeling [3] and information storage [4], among others. They are also being applied to amplify, guide or localize light, which can be conveniently combined with conventional optoelectronics in the future (new concepts of photo-plasmonic devices) [5]. In this sense, much effort has been devoted to the

* Corresponding author.
E-mail address: erjivi@uv.es (E. Jiménez).

0749-6036/$ - see front matter © 2007 Elsevier Ltd. All rights reserved.
doi:10.1016/j.spmi.2007.06.025

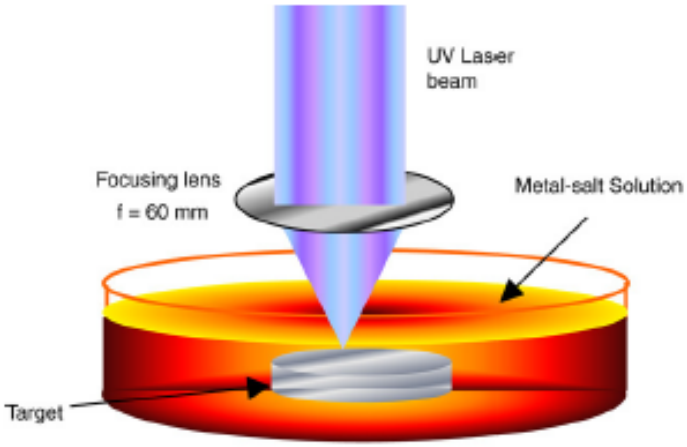

Fig. 1. Schematic diagram of the experimental setup for nanoparticle production.

synthesis of silver nanoparticles with different shapes, such as two-dimensional nanoprisms [6], one-dimensional silver nanorods or nanwires [7,8], and zero-dimensional spherical or tetrahedral dots [8]. These particles have been produced by different methods. It is found that the chemical and physical properties of these particles depend on their size and shape. For example, the shape of silver and gold nanoparticles was found to determine the number and position of surface plasmon resonance (SPR) peaks and the effective spectral range for surface-enhanced Raman scattering (SERS) [10]. So, one of the most important challenges in the preparation of metal nanoparticles is the control of their size, shape and morphology [9–11]. In general, metal nanoparticles can be prepared and stabilized by various methods, such as photochemical reduction [12] and even laser ablation of thin metal films in different solvents [13], as the closest methods to ours. These techniques have some advantages and disadvantages, in terms of the complexity of the method and the obtained size distribution and colloid stability. In this work we present a new method for fast and easy production of stable metal nanoparticles with a relatively narrow particle size distribution. A mixed chemical/physical method based on laser ablation of a silicon target is proposed in order to produce a liquid volume at very high temperature, where the chemical reaction can develop rapidly.

2. Experimental

Fig. 1 illustrates the simple experimental method used to synthesize metal nanoparticles upon laser irradiation of a solid target immersed in a solution of metal salts. The laser used for ablation is a third-harmonic ($\lambda = 355$ nm) Q-Switch Nd:YAG ultraviolet (UV) laser, giving pulses < 40 ns wide at a repetition rate of 5 KHz. The power density per pulse used in the experiments was around 40 J cm^{-2}. A silicon target with a purity of 99.99% was placed and fixed at the bottom of a glass vessel containing 20 ml of water solution of $AgNO_3$ or $HAuCl_4$. Upon irradiation of the Si target at room temperature during a few minutes, the solution gradually changes in color, indicating the formation of colloidal metal nanoparticles. The formation of silver nanocrystals in water solution was investigated by changing the concentration of the salt and laser ablation time. The resulting colloids were examined by transmission electron microscopy (TEM), performed on a 100 kV JEOL model 1200EX, and by X-Ray diffraction (XRD), carried out with a Seifert XR3003TT. Absorbance spectra of the colloids were measured with a UV–visible (UV–vis) spectrophotometer Shimadzu_2501; these colloids were previously purified by centrifugation for

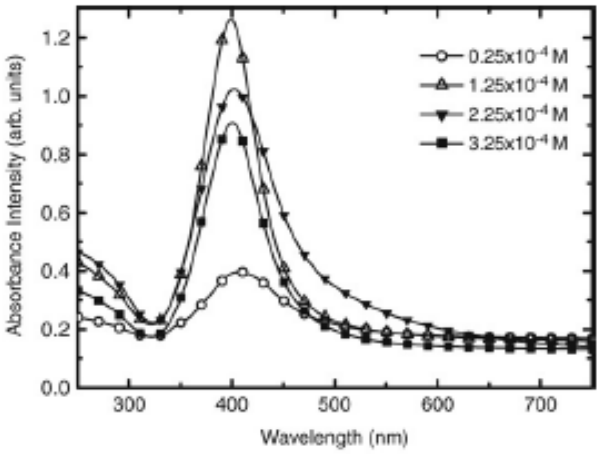

Fig. 2. Absorptance spectra of silver nanoparticles prepared from different concentrations of $AgNO_3$ in water.

20 min at 4000 rpm in order to eliminate the cloudiness. Both the precipitated and the purified colloid were analyzed by XRD.

3. Results and discussion

Fig. 2 shows UV–vis absorptance spectra of samples prepared from different $AgNO_3$ concentrations at a constant irradiation of the silicon target for 264 s with an average power of 0.9 W. The observed absorptance resonance at around 400 nm is the characteristic SPR signature of Ag nanoparticles. We measure an increase in the SPR absorptance when increasing the $AgNO_3$ concentration up to a value of 1.25×10^{-4} M, without a significant modification of its maximum wavelength. Above that concentration the SPR intensity diminishes, broadens and shifts to the red. This effect could be an indication of the formation of silver nanoparticles with larger average size.

Another parameter having an important effect on the formation of Ag nanoparticles is the laser irradiation time (LIT). The increment of LIT from 33 to 264 s results in an increase in the SPR intensity, with the peak position remaining practically constant, as shown in Fig. 3. A LIT greater than or equal to 528 s leads now to a sensible decrease in the SPR intensity, accompanied by a slight change in bandwidth and maximum wavelength. This reduction in intensity can be explained by the increase in the concentration of large silicon nanoparticles formed in solution during the ablation process, resulting in the co-precipitation of them and silver nanoparticles due to electrostatic attraction between them. In fact, the growing importance of these large Si particles in the solution is inferred from the higher cloudiness of samples obtained for long LIT, which also leads to an absorption background increase observed at long wavelengths (above 600 nm in Fig. 3).

At this point, we have presented the possibility of producing Ag nanoparticles with high efficiency when comparing the maximum SPR values with the salt concentration and LIT, but which is the mechanism enabling this efficient process? It is believed that high temperatures reached at the irradiation area on the target surface to be the origin. The high temperatures reached around the laser spot should simultaneously induce both the Ag^+ reduction to Ag in solution, and the subsequent silver nanoparticle formation, together with the Si target ablation. On the other hand, the laser ablation of a Si target must yield Si nanoparticles [14]. Given that the

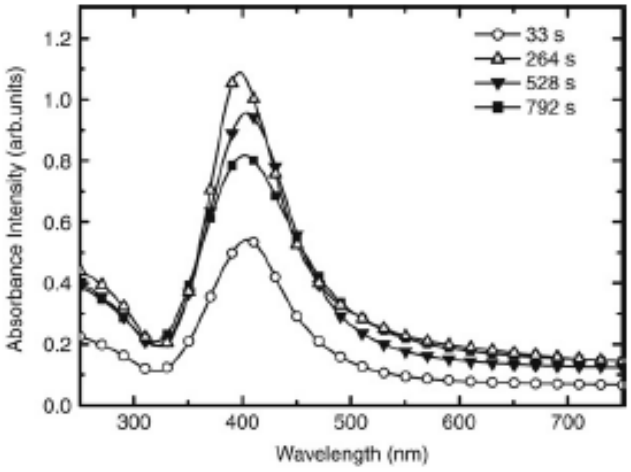

Fig. 3. Absorptance spectra of silver nanoparticles prepared at different irradiation times and constant power, using a silicon target immersed in 20 ml of $AgNO_3$ solution (2.25×10^{-4} M).

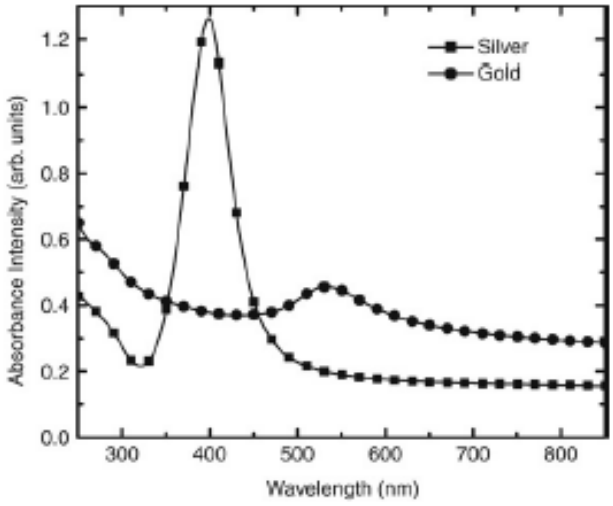

Fig. 4. Absorptance spectra of silver and gold nanoparticles prepared by laser irradiation of a silicon target for 264 s from the same molar concentration (1.25×10^{-4} M) of an aqueous solution of $AgNO_3$ and $HAuCl_4$, respectively.

Si is easily passivated, Si nanoparticles are expected to be oxidized immediately. It is suggested that Ag nanoparticles and SiO_2 nanoparticles are produced during the ablation process, leading to the high stability of our Ag colloids.

In order to prove the efficiency of this novel technique to carry out the synthesis of other materials, we have changed the metal-salt of $AgNO_3$ to another metal source. Therefore gold nanoparticles have also been synthesized from $HAuCl_4$ solution in water under the same experimental conditions as those used for the synthesis of Ag nanoparticles. Fig. 4 compares the UV–visible spectra obtained for both colloids that were obtained. The maximum wavelength of SPR corresponding to Au nanoparticles is located at 537 nm, as expected from the literature [15]. Indeed, the absorptance spectrum is essentially the same as that of gold nanoparticles prepared by other reduction methods, which proves the efficiency of this easy technique in preparing

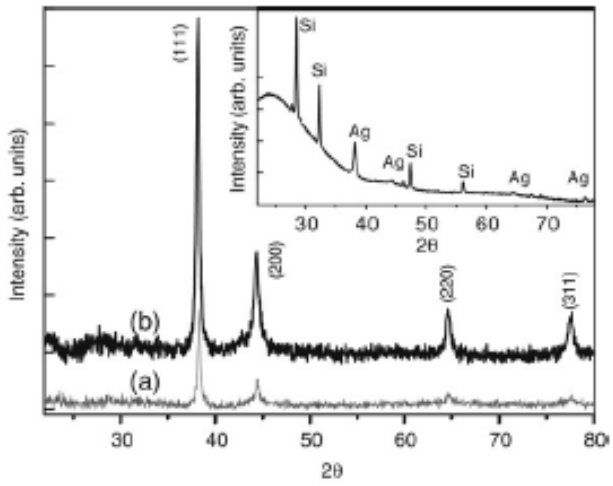

Fig. 5. XRD patterns recorded from drop Ag (a) and Au (b) coated films on glass substrates. The inset shows the diffractogram of the precipitated materials after purification of the Ag colloid.

nanoparticle colloids. The SPR of Au nanoparticles is six times less intense than that of Ag nanoparticles, as a result of a lower reaction yield. This is consistent with the higher temperature for the reduction of $HAuCl_4$ salt. Moreover, it may be suggested that the increasing light scattering phenomena that take place as the Au nanoparticles are synthesized significantly affects the absorption of the laser by the silicon target and therefore the Au(III) reduction yield. This is of special importance in our experiment, since the laser that was used has a wavelength of 355 nm, which is strongly absorbed and scattered by gold nanoparticles upon irradiation. Further work must be focused on optimizing different parameters, such as the irradiation wavelength, in order to minimize the light scattering produced by gold nanoparticles and to maximize the reaction yield.

Another question of interest in the synthesis of nanoparticles is their crystalline nature and the most common facets. It is also important for the demonstration that we predominantly have metal nanoparticles in the colloid. In this way, we have measured XRD spectra of films deposited on glass by dropping silver and gold colloidal solutions (1.25×10^{-4} M). The results are shown in Fig. 5, and compared (inset of Fig. 5) with the XRD spectrum measured for the precipitated material obtained by centrifugation of the colloidal solution. The diffractogram (a) exhibits four distinct diffraction peaks at 2θ values of 38.18°, 44.39°, 64.57° and 77.54° respectively, which correspond to the (111), (200), (220) and (311) crystalline planes of the cubic fcc silver reported on JCPDS cards 4-0783. The diffractogram (b) exhibits a number of strong Bragg reflections at 2θ values of 38.11°, 44.39°, 64.57° and 77.54°, which can be assigned to the (111), (200), (220) and (311) reflections of the cubic fcc gold, also in agreement with the reported JCPDS file No.040784. The XRD diffractogram shown in the inset of Fig. 5 corresponds to the precipitated materials after centrifugation. This shows a number of Bragg reflections associated with crystalline silicon and silver. The most likely explanation is the formation of large Si particles during ablation that attract silver nanoparticles and precipitate (in this way, they are easily removed by centrifugation). The absence of crystalline SiO_2 peaks is remarkable, but this does not mean the absence of this oxide. SiO_2 can be present in the amorphous state, given its fast formation.

The TEM micrograph and the corresponding size distributions of silver nanoparticles prepared from a water solution of $AgNO_3$ 1.25×10^{-4} M are shown in Fig. 6. We observe that most of

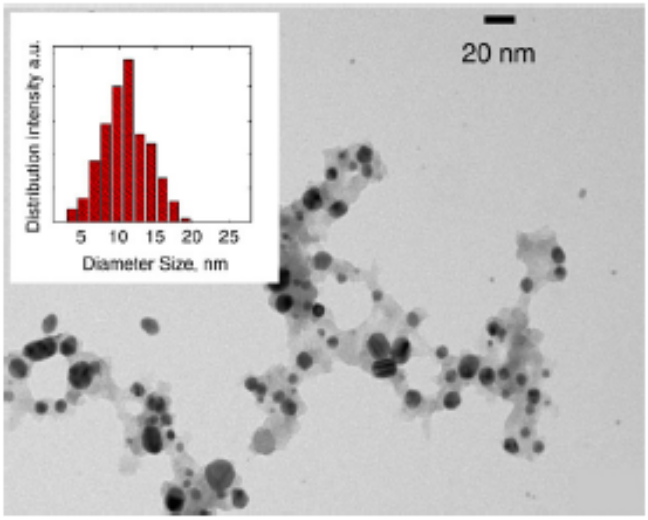

Fig. 6. Electron micrograph and size distribution of the silver nanoparticles produced by irradiating the Si target in a solution with $AgNO_3$ concentration 1.25×10^{-4} M.

the Ag nanoparticles are nearly spherical, within the experimental resolution (1–2 nm), except for a small portion (typically bigger than the average) exhibiting cubic facets, which is consistent with the most important peaks measured in the XRD spectra. After the examination of several micrographs, we measure a diameter distribution in the range 5–20 nm, with an average value of 11 nm. A further increase in the metal-salt concentration of the irradiated solution leads to an increase in the average nanoparticle diameter and a broad size distribution, consistent with the SPR spectra shown in Fig. 1.

4. Conclusion

We have prepared silver and gold nanoparticles by a novel technique consisting of laser ablation of a Si target immersed in a water solution of a metal-salt ($AgNO_3$ and $HAuCl_4$, respectively), as the metal source. Stable colloidal solutions of gold and silver nanocrystals in a single step were successfully prepared by this novel technique. We have investigated the effect of the metal-salt concentration and irradiation time on the silver SPR. The concentration of the metal colloid can be controlled by either the metal-salt concentration or the laser irradiation time. The diameter of the silver nanoparticles can be controlled with the metal-salt concentration. XRD patterns indicate that synthesized silver and gold nanoparticles are perfectly crystalline and exhibit some predominant facets, as is also observed by TEM with enough resolution for the biggest nanoparticles. All these results further confirm the success of this novel technique in forming nanoparticles in stable colloids. We foresee the use of this technique in the future for producing nanoparticles of other materials, such as semiconductors and dielectrics.

Acknowledgments

The authors are grateful for the financial support of the IMPIVA (Generalitat Valenciana) through project IMCOIC/2006/50 and the Spanish MEC through project TEC2005-05781-C03-03.

References

[1] D.M.-K. Lam, B.W. Rossiter, Sci. Am. 265 (1991) 80.
[2] L.N. Lewis, Chem. Rev. 93 (1993) 2693.
[3] S.R. Nicewarner-Peña, et al., Science 294 (2001) 137.
[4] C.B. Murray, S. Sun, H. Doyle, T. Betley, Mater. Res. Soc. Bull. 26 (2001) 985.
[5] E. Cubukcu, E.A. Kort, K.B. Crozier, F. Capasso, Appl. Phys. Lett. 89 (2006) 093120.
[6] I. Pastoriza-Santos, Luis M. Liz-Marzán, Nano Lett. 2 (2002) 903.
[7] Y. Sun, B. Gates, B. Mayers, Younan Xia, Nano Lett. 2 (2002) 165.
[8] Y.-Y. Yu, S.-S. Chang, C.-L. Lee, C.-R. Chris Wang, J. Phys. Chem. B 101 (1997) 6661.
[9] I.O. Sosa, C. Noguez, R.G. Barrera, J. Phys. Chem. B 107 (2003) 6269.
[10] H.-H. Wang, C.-Y. Liu, S.-B. Wu, N.-W. Liu, C.-Y. Peng, T.-H. Chan, C.-F. Hsu, J.-K. Wang, Y.-L. Wang, Adv. Mater. 18 (2006) 491.
[11] M.A. El-Sayed, Accounts Chem. Res. 34 (2001) 257.
[12] K.L. McGilvray, M.R. Decan, D. Wang, J.C. Scaiano, J. Amer. Chem. Soc. 128 (2006) 15980.
[13] A. Henglein, J. Phys. Chem. 97 (1993) 5457.
[14] S.I. Dolgaev, A.V. Simakin, V.V. Voronov, G.A. Shafeev, F. Bozon-Verduraz, Appl. Surf. Sci. 186 (2002) 546.
[15] S. Link, M.A. El-Sayed, J. Phys. Chem. B 103 (1999) 4212.

PUBLICACIÓN V

Laser-ablation induced synthesis of metal-oxide beads in a single step

E. Jiménez, K. Abderrafi, R. Abargues, J.L. Valdés, and J.P. Martínez-Pastor

Langmuir 26, 7458-7463 (2010)

Langmuir
Article
pubs.acs.org/Langmuir

Laser-Ablation-Induced Synthesis of SiO_2-Capped Noble Metal Nanoparticles in a Single Step

Ernesto Jiménez,* Kamal Abderrafi, Rafael Abargues, José L. Valdés, and Juan P. Martínez-Pastor*

Instituto de Ciencias de los Materiales, Universidad de Valencia, P.O. Box 22085, 46071 Valencia, Spain

Received November 3, 2009. Revised Manuscript Received February 16, 2010

Here we describe a simple, powerful technique based on the laser ablation of a target immersed in a water solution of a metal salt. With this method, nanoparticles of different metals and alloys can be processed very quickly. Both the target and the salt solution can be chosen to produce metal nanoparticles of different sizes, surface-oxidized nanoparticles (silica−silver, for example), or even more complex structures to be defined by the researcher on one or more steps because the technique combines the advantages of both physical and chemical methods. We have applied this technique to the fabrication of inert silica−metal (silver, gold, and silver−gold) nanoparticles with a strong surface plasmon resonance all together in a single step. The advantage of the simultaneous production of silica during laser ablation is the stabilization of the metal nanoparticle colloid but also the possibility to reduce the toxicity of these nanoparticles.

1. Introduction

The use of laser radiation as an external source of energy to evaporate materials in vacuum, to be deposited as thin films, was reported for the first time by Smith and Turner in 1965.[1] However, subsequent investigations in this area were sporadic. It was only in the late 1980s when the use of this technique to obtain thin films of high critical temperature superconductors was demonstrated.[2,3] In the following years, laser ablation has been used as a powerful instrument to fabricate nanostructures in three environments: vacuum,[4,5] an inert atmosphere,[6−8] and liquid.[9,10] The irradiation of solid targets immersed in a liquid environment has given rise to nanoparticles (NPs) of the same materials (as the targets).[9−12] The quality and the production rate of the NPs obtained by this method are inferior to those that can be obtained by chemical synthesis.[13−15] The best results with this last technique have been achieved in nonaqueous and nonphysiological pH solution,[15,16] although the collected NPs require further processing in order to be used in biology and medical biophysics.[17−19]

In particular, metal NPs have attracted much attention because of their electronic and optical properties.[20,21] Many aspects of these optical properties (localized surface plasmon resonance, LSPR, and surface-enhanced Raman scattering, SERS) and applications (biosensing and single-molecule detection) have been reported during the last few years.[22−26] Of particular interest is their use in biological labeling and photothermal cancer nanotherapy.[27−30] For such applications, it is important to control the size and shape of the NPs[31−34] as well as their toxicity. Metal NPs have been synthesized by different methods such as photochemical,[35,36] laser ablation in a liquid environment,[9,10]

*Corresponding authors. E-mail: ernesto.jimenez@uv.es, juan.mtnez.pastor@uv.es.

(1) Smith, H. M.; Turner, A. F. *Appl. Opt.* **1965**, *4*, 147–148.
(2) Dijkkamp, D.; Venkatesan, T.; Wu, X. D.; Shaheen, S. A.; Jisrawi, N.; Min-Lee, Y. H.; McLean, W. L.; Croft, M. *Appl. Phys. Lett.* **1987**, *51*, 619–621.
(3) Wu, X. D.; Dijkkamp, D.; Ogale, S. B.; Inam, A.; Chase, E. W.; Miceli, P. F.; Chang, C. C.; Tarascon, J. M.; Venkatesan, T. *Appl. Phys. Lett.* **1987**, *51*, 861–863.
(4) Okano, A.; Takayanagi, K. *Appl. Surf. Sci.* **1998**, *127−129*, 362–367.
(5) Ballesteros, J. M.; Solis, J.; Serna, R.; Afonso, C. N. *Appl. Phys. Lett.* **1999**, *74*, 2791–2793.
(6) Heath, J. R.; Liu, Y.; O'Brien, S. C.; Zhang, Q.; Curl, R. F.; Tittel, F. K.; Smalley, R. E. *J. Chem. Phys.* **1985**, *83*, 5520–5526.
(7) Rodriguez, E.; Jimenez, E.; Padilha, L. A.; Neves, A. A. R.; Jacob, G. J.; Cesar, C. L.; Barbosa, L. C. *Appl. Phys. Lett.* **2005**, *86*, 113117–3.
(8) Yu, D. P.; Sun, X. S.; Lee, C. S.; Bello, I.; Lee, S. T.; Gu, H. D.; Leung, K. M.; Zhou, G. W.; Dong, Z. F.; Zhang, Z. *Appl. Phys. Lett.* **1998**, *72*, 1966–1968.
(9) Neddersen, J.; Chumanov, G.; Cotton, T. M. *Appl. Spectrosc.* **1993**, *47*, 1959–1964.
(10) Fojtik, A.; Giersig, M.; Henglein, A. *Ber. Bunsen-Ges. Phys. Chem. Chem. Phys.* **1993**, *97*, 1493–1496.
(11) Dolgaev, S. I.; Simakin, A. V.; Voronov, V. V.; Shafeev, G. A.; Bozon-Verduraz, F. *Appl. Surf. Sci.* **2002**, *186*, 546–551.
(12) Anikin, K. V.; Melnik, N. N.; Simakin, A. V.; Shafeev, G. A.; Voronov, V. V.; Vitukhnovsky, A. G. *Chem. Phys. Lett.* **2002**, *366*, 357–360.
(13) Danek, M.; Jensen, K. F.; Murray, C. B.; Bawendi, M. G. *Chem. Mater.* **1996**, *8*, 173–180.
(14) Harrison, M. T.; Kershaw, S. V.; Burt, M. G.; Eychmüller, A.; Weller, H.; Rogach, A. L. *Mater. Sci. Eng., B.* **2000**, *69−70*, 355–360.
(15) Mokari, T.; Banin, U. *Chem. Mater.* **2003**, *15*, 3955–3960.
(16) Green, M.; O'Brien, P. *Chem. Commun.* **1999**, 2235–2241.
(17) Bailey, R. E.; Smith, A. M.; Nie, S. *Physica E* **2004**, *25*, 1–12.
(18) Feng, W.; Tan, W. B.; Zhang, Y.; Fan, X.; Wang, M. *Nanotechnology* **2006**, *17*, R1–R13.
(19) Cozzoli, P. D.; Pellegrino, T.; Manna, L. *Chem. Soc. Rev.* **2006**, *35*, 1195–1208.
(20) Link, S.; El-Sayed, M. A. *Int. Rev. Phys. Chem.* **2000**, *19*, 409.
(21) Lee, K.; El-Sayed, M. A. *J. Phys. Chem. B* **2006**, *110*, 19220–19225.
(22) Lewis, L. N. *Chem. Rev.* **1993**, *93*, 2693–2730.
(23) Murray, C. B.; Sun, S.; Doyle, H.; Betley, T. *MRS Bull.* **2001**, *26*, 985–991.
(24) Schaadt, D. M.; Feng, B.; Yu, E. T. *Appl. Phys. Lett.* **2005**, *86*, 063106–3.
(25) Bryant, G. W.; Garcia de Abajo, F. J.; Aizpurua, J. *Nano Lett.* **2008**, *8*, 631–636.
(26) Oldenburg, A. L.; Hansen, M. N.; Zweifel, D. A.; Wei, A.; Boppart, S. A. *Opt. Express* **2006**, *14*, 6724–6738.
(27) Huang, X.; El-Sayed, I. H.; Qian, W.; El-Sayed, M. A. *J. Am. Chem. Soc.* **2006**, *128*, 2115–2120.
(28) Durr, N. J.; Larson, T.; Smith, D. K.; Korgel, B. A.; Sokolov, K.; Ben-Yakar, A. *Nano Lett.* **2007**, *7*, 941–945.
(29) O'Neal, D. P.; Hirsch, L. R.; Halas, N. J.; Payne, J. D.; West, J. L. *Cancer Lett.* **2004**, *209*, 171–176.
(30) Hirsch, L. R.; Stafford, R. J.; Bankson, J. A.; Sershen, S. R.; Rivera, B.; Price, R. E.; Hazle, J. D.; Halas, N. J.; West, J. L. *Proc. Natl. Acad. Sci. U.S.A.* **2003**, *100*, 13549–13554.
(31) Halperin, W. P. *Rev. Mod. Phys.* **1986**, *58*, 533.
(32) Maillard, M.; Giorgio, S.; Pileni, M. *Adv. Mater.* **2002**, *14*, 1084–1086.
(33) Jin, R.; Cao, C. Y.; Hao, E.; Metraux, G. S.; Schatz, G. C.; Mirkin, C. A. *Nature* **2003**, *425*, 487–490.
(34) Chen, J.; Wiley, B. J.; Xia, Y. *Langmuir* **2007**, *23*, 4120–4129.
(35) McGilvray, K. L.; Decan, M. R.; Wang, D.; Scaiano, J. C. *J. Am. Chem. Soc.* **2006**, *128*, 15980–15981.
(36) Huang, H. H.; Ni, X. P.; Loy, G. L.; Chew, C. H.; Tan, K. L.; Loh, F. C.; Deng, J. F.; Xu, G. Q. *Langmuir* **1996**, *12*, 909–912.

electrochemical,[37] and chemical reduction.[38] These different methods may also determine their size and shape.[31,39] Generally, NPs are unstable in solution with respect to their size, resulting in agglomeration into large particles and subsequent precipitation. To avoid this situation, NPs have to be protected or encapsulated with organic capping agents such as thiols, amines, and polymers or oxides such as SiO_2 and TiO_2. The selection of an appropriate capping agent is of significant importance for biotechnology and biomedical applications to achieve high solubility in organic fluids, adequate binding properties to the desired proteins or cells, and low cytotoxicity.[40] Silica is particularly advantageous for solubility, low density, and the inertness of NPs while introducing numerous possibilities for their use. It has many potential applications in biomedicine because of negligible harm to live cells.[41,42]

Here, we report a simple single-step method for the fast (2 to 3 min), scalable synthesis of inert colloidal metal−silica NPs in stable colloids. The method is based on the laser ablation of a solid target submerged in an aqueous solution of the metal salts, whose reduction will give rise to nanoparticles.[43] At the same time, the evaporated material from the target (Si) produces (other than large Si particles eliminated from the final colloid by a simple centrifugation filtering) nanometer-sized silica NPs that are capping metal nanoparticles, as deduced from spatially resolved chemical analysis (using a transmission electron microscope). The method described here combines the advantages of chemical synthesis with the versatility of the laser ablation technique. In fact, the high yield and fast processing time exhibited by our method are very promising for the scalable production of NPs. In addition, ablation parameters, target materials, and metal salts can be combined and controlled to influence the size, morphology, and composition of nanoparticles.

2. Experimental Section

The proposed method of synthesis is based on the laser irradiation of a given solid target immersed in a solution of metal salts. The laser used for ablation is the third harmonic (λ = 355 nm) of a Q-switch Nd:YAG UV laser, giving pulses < 40 ns wide at a repetition rate of 5 kHz. The laser power densities per pulse on the target surface were always below 40 J/cm^2 (1 W of average power). Several targets such as silicon, germanium, and tungsten with a purity of 99.99% were placed and fixed at the bottom of a glass vessel containing 20 mL of $AgNO_3$ ($HAuCl_4$ or a mixture of both salts) in a water solution in order to produce silver (gold and a silver−gold alloy) NPs. The liquid solution was not stirred during the 120 s (longer times were used in the results shown in the Supporting Information) of the ablation process, but 1 cm^2 of the target surface was swept at a rate of 30 lines/s (1000 lines per cm). The samples prepared with this physicochemical method based on the laser ablation of a silicon target, for example, were purified by centrifugation or filtration prior to their characterization in order to eliminate large Si particles formed during the ablation process.

The optical characterization (LSPR spectra) of colloids was performed on a UV−vis Shimazu_2501 spectrophotometer. X-ray diffraction was carried out on both the NPs in the colloidal suspension and the recovered precipitate after centrifugation (depositied on a glass substrate) in a Saifert XR3003TT using Cu Kα radiation with λ = 1.54056 Å. The colloidal solutions were examined by transmission electron microscopy (TEM) with a JEOL-1200EX microscope operated at 100 kV and by energy dispersive X-ray spectrometry (EDX) microanalysis with a field-emission scanning electronic microscope (Hitachi S-4100). The films prepared for EDX microanalysis were deposited onto a GaAs substrate (i.e., chemically different from the materials under study). The samples were prepared by drop casting metal alloy nanoparticle colloids in order to obtain the Si−O and Au−Ag ratios. High-resolution TEM (HRTEM) was performed in a FEI-TECNAI G2. Spatially resolved chemical analysis was also performed with this microscope by using an EDAX detector, whose active area is 30 mm^2 with an energy resolution equal to 127.83 eV.

3. Results and Discussion

Metal NPs were synthesized using the simple experimental setup shown in Figure 1a. This method is based on the laser irradiation of a given solid target immersed in an aqueous solution of metal salts. After the irradiation of the target (silicon is the one selected in this work) at room temperature for a few minutes, the solution gradually changes color (Figure 1b), indicating the formation of colloidal metal NPs: silver (yellow colloid), gold (purple colloid), and silver−gold alloys (intermediate colloid colors). After the simple centrifugation (or filtering) of samples produced by the ablation of a Si target, we obtain perfectly stable colloids; that is, we do not observe material precipitation. The colloids shown in Figure 1 have been obtained by using a solution containing 1.25×10^{-4} M $AgNO_3$ (silver colloid), $HAuCl_4$ (gold colloid), and mixtures of $AgNO_3$−$HAuCl_4$ (silver−gold colloids) metal salts. In the case of a water solution containing $AgNO_3$, we have deduced the optimal laser irradiation time (around 120 s) and salt concentration (1.25×10^{-4} M) when using the maximum power and repetition rate of the UV laser, as summarized in the Supporting Information furnished with this article (Figure 1sup).

The process giving rise to Ag−Au alloy NPs differs from standard chemical synthesis, and it has been studied in more detail. On one side, we have measured the average content of Au inside the NPs of every colloid by EDX measurements of drop-cast layers, and it is used as the abscissa in Figure 1c and the inset in Figure 1d. On the other side, we have obtained the average size of the Ag−Au NPs from TEM images (images and size histograms included in Figure 2sup of the Supporting Information), and it is represented as a function of the Au content in the inset of Figure 1d. Above 25−30% Au content in the NPs, the incorporation of Au atoms from the solution is 1:1, whereas it tends toward 3:1 at very low concentrations, as shown in Figure 1c. This is the reason that the diameter of the NPs decreases in the concentration range of 0−30% with respect to the value found for pure Ag, as illustrated in the inset of Figure 1d. When adding small quantities of Au salt to the liquid solution for ablation, each Au(III) atom substitutes up to three Ag(I) atoms at the nanoparticle, which is initially formed with pure Ag when the Au salt concentration tends toward zero. This substitution mechanism would explain the reduction of the size depicted in the inset of Figure 1d due to the decrease in the total number of atoms at the nanoparticle.

The absorbance spectra measured for Ag−Au colloids are shown Figure 1d. The wavelengths of the characteristic localized surface plasmon resonance (LSPR) for pure silver and gold colloids are 400 and 520 nm, respectively (i.e., the expected

(37) Mahapatra, , S. K.; Bogle, , K. A.; Dhole, , S. D.; Bhoraskar,, V. N. *Nanotechnology* **2007**, *18*.
(38) Taleb, A.; Petit, C.; Pileni, M. P. *Chem. Mater*. **1997**, *9*, 950–959.
(39) Burda, C.; Chen, X.; Narayanan, R.; El-Sayed, M. A. *Chem. Rev*. **2005**, *105*, 1025–1102.
(40) Huff, T. B.; Tong, L.; Zhao, Y.; Hansen, M. N.; Cheng, J.-X.; Wei, A. *Nanomedicine* **2007**, *2*.
(41) Baca, H. K.; Ashley, C.; Carnes, E.; Lopez, D.; Flemming, J.; Dunphy, D.; Singh, S.; Chen, Z.; Liu, N.; Fan, H.; Lopez, G. P.; Brozik, S. M.; Werner-Washburne, M.; Brinker, C. J. *Science* **2006**, *313*, 337–341.
(42) Bharali, D. J.; Klejbor, I.; Stachowiak, E. K.; Dutta, P.; Roy, I.; Kaur, N.; Bergey, E. J.; Prasad, P. N.; Stachowiak, M. K. *Proc. Natl. Acad. Sci. U.S.A*. **2005**, *102*, 11539–11544.
(43) Jiménez, E.; Abderrafi, K.; Martínez-Pastor, J.; Abargues, R.; Valdés, J. L.; Ibáñez, R. *Superlattices Microstruct*. **2008**, *43*, 487–493.

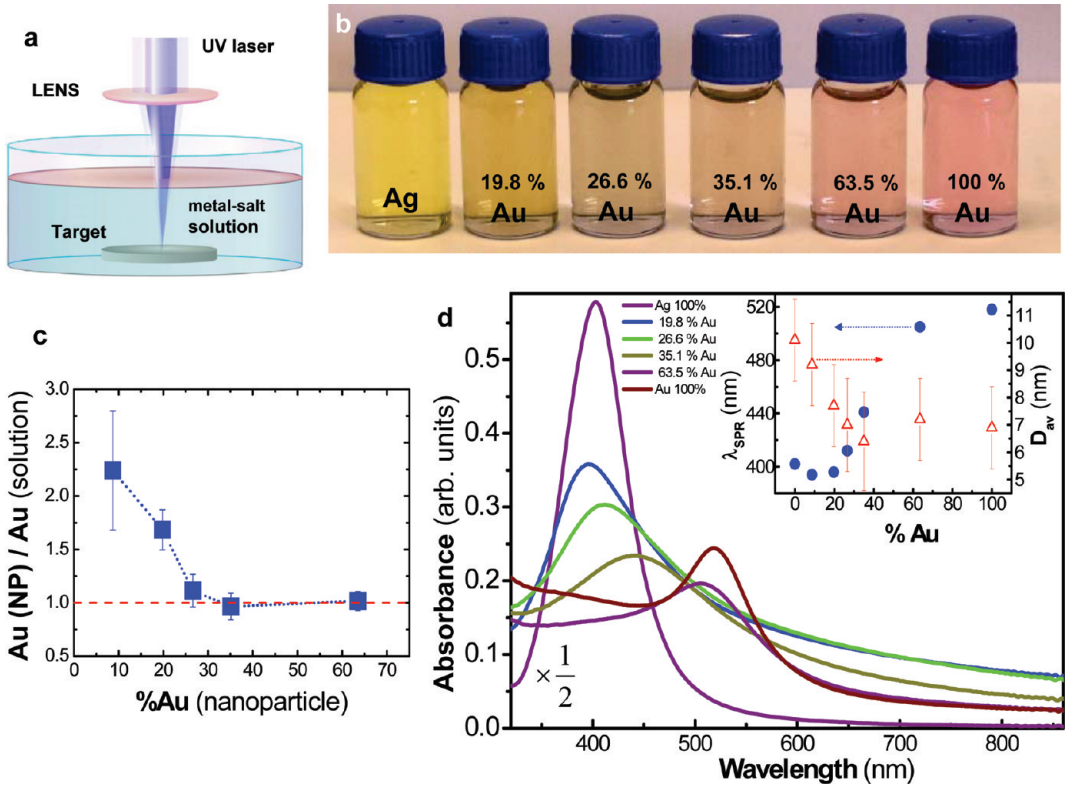

Figure 1. (a) Scheme of the proposed ablation method in which a (silicon) target is immersed into a metal salt solution in water. (b) Photograph of the metal nanoparticle colloids obtained by this ablation method, from pure silver (left) to pure gold (right) and several Ag−Au alloys. (c) Ratio of the gold content in the NP (gold reduction measured by EDX microanalysis) with respect to that in the salt solution represented as a function of the first quantity. (d) A noticeable red shift is observed in the LSPR absorbance spectrum of the Ag−Au nanoparticle colloid when increasing the Au content in the alloy, except below 20% Au content, where a small blue shift is observed because of a change in the NP size (as measured by TEM; see Figure 2supp in the Supporting Information). The error in the measurement of % Au(NP) by the EDX microanalysis method is around 4%, approximately the size of the symbols in panel c and the inset in panel d.

wavelengths for these kinds of colloids). Intermediate LSPR wavelengths are obtained for alloys with Au percentages above 30%, which can be due to the formation of perfectly disordered Ag−Au alloys. When the molar concentration of gold is below 25−30%, the formation of Au shells around the initially formed Ag cores is the most probable constitution of the NPs, consistently with the atom-substitution mechanism dominant in this Au concentration range, as explained above. This is why we observe in Figure 1d a small blue shift of the LSPR wavelength (associated with the average size reduction of the NPs) and an important broadening of the extinction coefficient of the NPs toward the infrared. Similar behavior has been described in the literature for strictly chemical synthesis procedures.[44,45] Above a 30% molar percentage of Au in the solution, we measure the same percentage in the NPs, as shown in Figure 1c. The atom-substitution mechanism does not hold anymore, and the size of the NPs remains constant at a value of around 7 nm, as observed in the inset of Figure 1d. Within this % Au range, the absorbance curves of the colloids narrow again and the LSPR wavelength increases linearly with increasing % Au as shown in Figure 1d, consistently with perfect alloy formation, as described in ref 46 for laser -irradiated core−shell NPs.

Our method is versatile because many other single metals and complex NPs can be synthesized by changing and/or mixing appropriate metal salts. Together with the metal salt solution, a second important variable in our method is the target, whose physical and chemical properties can influence the nanoparticle composition and the colloid stability. Laser ablation depends necessarily on the physicochemical parameters of the target,[47] and hence we expect different efficiencies in the synthesis of silver NPs and even differences in the physical properties of the NPs and colloids. Figure 2a−d shows the different size of pure silver NPs obtained by ablating Si and W targets under similar conditions: 10 and 3 nm, respectively. This difference is consistent with their extinction coefficient spectra shown in Figure 2e (blue and red curves): the LSPR of the silver colloid obtained when using the W target is very broad and red-shifted. Two Lorentzian components at around 425 and 545 nm can be deconvoluted from its corresponding LSPR spectrum. The peak intensity is nearly a factor of 10 smaller than the maximum intensity reached for the colloid prepared with the silicon target, but the integrated intensity decreases only by less than a factor of 3. This factor would be ascribed to the different efficiency of nanoparticle production in both targets. The fact that two LSPR bands appear is attributed to the formation of agglomerated ensembles in the colloid. This effect is not observed in the colloids synthesized by using silicon and germanium (green curve) targets, which exhibit a very similar LSPR narrow band with a peak at around 398 nm with similar intensity. More important is the fact that any appreciable LSPR feature is observed when no target (orange flat curve) is placed at the focus of the laser beam at the bottom

(44) Moskovits, M.; Srnova-Sloufova, I.; Vlckova, B. *J. Chem. Phys.* **2002**, *116*, 10435–10446.
(45) Chen, H.; Liu, R.; Jang, L.; Lee, J.; Hu, S. *Chem. Phys. Lett.* **2006**, *421*, 118–123.
(46) Hodak, J.; Henglein, A.; Giersig, M.; Hartland, G. *J. Phys. Chem. B* **2000**, *104*, 11708–11718.
(47) Ashfold, M. N. R.; Claeyssens, F.; Fuge, G. M.; Henley, S. J. *Chem. Soc. Rev.* **2004**, *33*, 23–31.

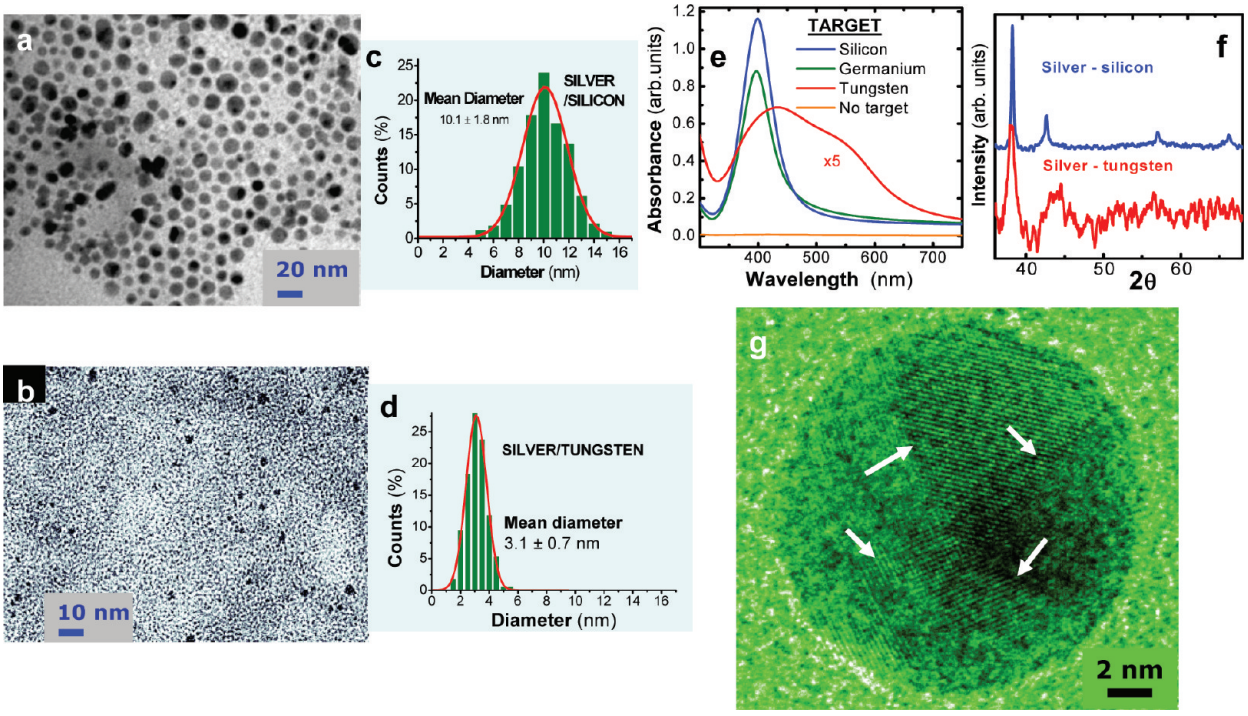

Figure 2. TEM images of silver nanoparticles produced by using the same metal salt solution but different ablation targets: (a) silicon and (b) tungsten. (c, d) NP size histograms obtained from several TEM images: a strong average size reduction is observed when using a tungsten target. (e) LSPR spectra of silver NP colloids obtained when changing the ablation target from silicon (blue curve) to germanium (green curve) and tungsten (red curve) targets, as compared to the silver salt solution irradiated without a target (yellow curve), which clearly does not show any appreciable formation of nanoparticles. The crystalline structure of silver NPs obtained by laser-ablation-assisted synthesis is demonstrated by (f) X-ray diffraction and (g) HRTEM. The arrows in the HRTEM images indicate the intersection of twinning planes.

of the vessel containing the silver nitrate solution. Of course, there should be some silver ion reduction and nanoparticle production,[36,48] but the efficiency of the photochemical reaction is very weak as compared to the ablation-assisted metal reduction of a target (Si, Ge, W, ...) for 120 s.

The observed differences between the plasmon-related extinction coefficient spectra of the three colloids obtained with ablation of different targets (Figure 2e) can be attributed to the different boiling point and reactivity of the target materials. Upon laser irradiation, the evaporation of targets occurs, reducing the limiting temperature reached at the target surface during ablation. It is well known that the lower the boiling temperature of the target, the higher the material evaporation. The laser ablation of silicon (boiling point equal to 1900 °C) leads to the formation of Si NPs.[10,11] At the same time, Si NPs are expected to be very reactive, immediately oxidizing to SiO_2 in water. Moreover, high temperatures[49,50] and pressures[50] in the ablation plume formed upon target irradiation may lead to fast silicon oxidation, also contributing to the simultaneous reduction of Ag(I) to Ag.

If, instead of Si, we irradiate a Ge target, then the material evaporation will be slightly more important because of its lower boiling point, 1800 °C, and higher absorption coefficient at 355 nm. At the same time, Ge also passivates to GeO_2 but not as much as occurs in Si. These small differences can slightly affect the Ag nanoparticle production consistently with the LSPR spectra shown in Figure 2e (blue and green curves). More differences are expected in the case of using a W target, whose boiling point is 5550 °C and has a reasonably high absorption coefficient at 355 nm. In this case, material evaporation would occur to a lesser extent and nanoparticle synthesis would take place at a higher temperature than in the ablation of Si and Ge targets. Moreover, the weak formation of a byproduct on the surface of the tungsten target was observed, which may obviously affect the laser−target interaction. According to Bottjer et al.,[51] Ag(I) reduction and WNO_3 formation may also take place on the tungsten target surface. Therefore, we expect silver NPs smaller than those obtained with Si and Ge targets, given the higher temperature reached at the W surface enhancing the reaction kinetics, as shown in Figure 2a−d. The absence (or a negligible amount) of a stabilizing agent, such as SiO_2 in the case of using a Si target, due to the weak evaporation of tungsten will favor the agglomeration of NPs. Now we can say that the origin of the red LSPR component (545 nm) measured for the colloids obtained with the W target is attributed to nanoparticle agglomeration by electrostatic interaction. On the contrary, silver NPs made with Si and Ge targets form stable colloids characterized by single LSPR spectra.

Some signatures of the metal NPs dispersed in the colloids obtained by our ablation method can be indirectly deduced from the LSPR spectra, given the literature available at present. However, the ablation-induced synthesis of metal NPs does not have a precedent, and we present in Figure 2f,g their more important structural data, other than the morphology and size shown in Figure 2a−d. Nanoparticles produced by our laser-assisted synthesis are crystalline, as demonstrated by X-ray diffraction (Figure 2f) and HRTEM (Figure 2g), similar to the case of NPs obtained by standard chemical methods based on the metal reduction in metal salt aqueous solutions. In X-ray diffraction spectra, we typically measure peaks associated with (111), (200), (220), and (311) crystalline planes, as indicated in Figure 2f.

(48) Zheng, X.; Xu, W.; Corredor, C.; Xu, S.; An, J.; Zhao, B.; Lombardi, J. R. *J. Phys. Chem. C* **2007**, *111*, 14962–14967.
(49) Sakka, T.; Yamagata, H.; Oguchi, H.; Fukami, K.; Ogata, Y. H. *Appl. Surf. Sci.* **2009**, *255*, 9576–9580.
(50) Ushida, H.; Takada, N.; Sasaki, K. *J. Phys.: Conf. Ser.* **2007**, *59*, 563–566.
(51) Bottjer, W. G.; Haendler, H. M. *Inorg. Chem.* **1965**, *4*, 913–915.

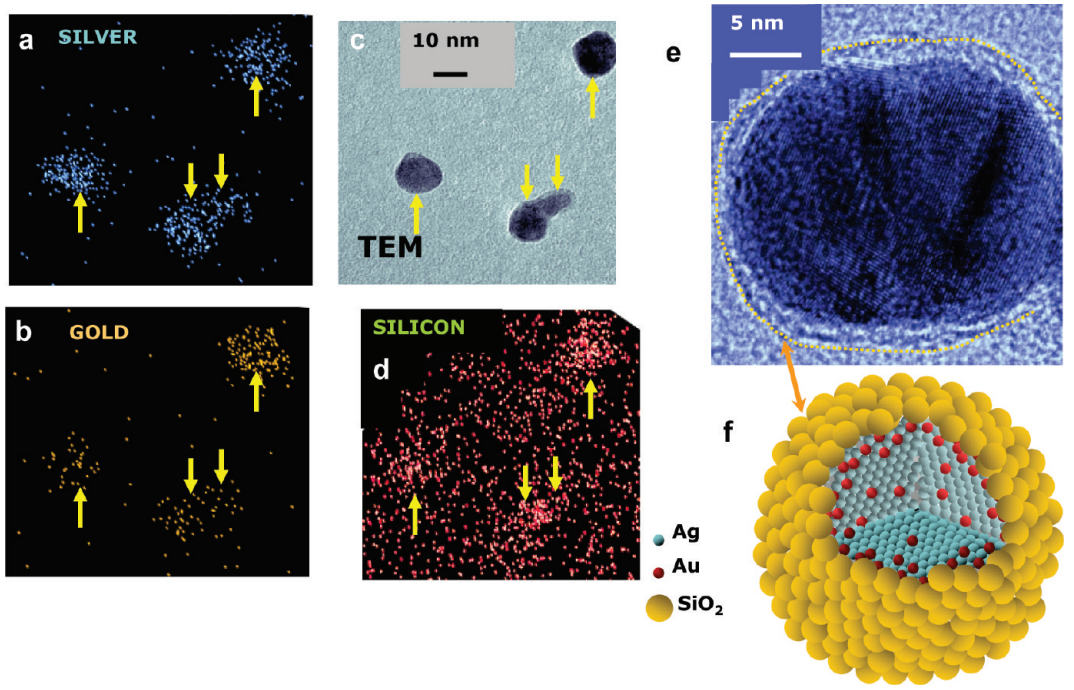

Figure 3. EDX-HRTEM chemical mapping images of silver−gold alloy NPs demonstrate the presence of (a) silver and (b) gold in the four NPs marked by yellow arrows and observed in (c) the real-space TEM image. (d) Other than silver and gold, the EDX-HRTEM also reveals the presence of silicon, but it is more concentrated around the NPs. The silicon (from ejected material during ablation) is found to be in the form of amorphous SiO_2, like a thin shell around the NP whose limit is indicated by a dotted yellow line in (e) the HRTEM real image and illustrated in panel f. The presence of stoichiometric SiO_2 in all colloids is extracted from EDX microanalysis performed by SEM on a drop-cast sample prepared on a GaAs substrate.

The larger line width of the X-ray diffraction peaks observed in Ag NPs synthesized by using a W target is consistent with their smaller average size (Figure 2d) if calculated through the Scherrer formula. The reason to measure X-ray diffraction spectra dominated by the (111) peak in drop-cast films prepared with our metal NPs, as observed in Figure 2f, can be attributed to the presence of twinning planes. The observation of {111}-type multiple twinning planes in metal NPs requires a special symmetry orientation with respect to the electron beam and it is not observed in all micrographs, but we can still find some of them on the prepared copper grid, such as the one shown in Figure 2g.[52]

Silver−gold NPs have crystalline characteristics similar to pure metal NPs, as shown in Figure 2g, typically characterized by multiple twinning planes. Silver and gold signals in HRTEM chemical mapping images can be measured at the NPs, as indicated by the arrows in Figure 3a−c, despite the intensity difference which is due to a smaller content of gold in the alloyed NPs (26.6%). Other than gold and silver signals in chemical mapping images (Figure 3a,b), we also measure a weak signal attributed to the presence of silicon all around the examined HRTEM area, being more intense at the position of the NPs, as shown in Figure 3d. One would say that an amorphous silica shell can be observed in some HRTEM micrographs such as the one indicated by the dotted yellow line in Figure 3e and illustrated in Figure 3f. The silicon dioxide present in the colloid can be due to the fast oxidation of sputtered silicon of the ablated target resulting from the high local temperatures that can be reached around the target surface,[49,50] as explained above. Large silicon particles can be perfectly eliminated from the colloid after standard mechanical centrifugation or filtration. Indeed, a signal was not detected in X-ray diffraction for silicon or silicon dioxide materials (Figure 2f), in the latter case because of its amorphous nature. We corroborate the presence of silica by independent EDX microanalysis carried out with SEM in drop-cast films prepared on GaAs using colloids fabricated by ablating Si targets both with and without metal salt in water. We detect the presence of Si and O with an O/Si ratio close to 2 in both films. Therefore, we propose a nanoparticle-type (they proceed from ejected Si NPs) core−shell metal−silica as illustrated in Figure 3f, where silica NPs smaller than 2 nm cover the core metal (pure or alloy) nanoparticle. The maximum size of these silica NPs is extracted from the shell thickness measured in HRTEM images, such as the one shown in Figure 3e. Furthermore, silica can also be present in the colloid solution, as demonstrated by chemical mapping HRTEM (Figure 3d). The small size attributed to silica NPs should be a consequence of the fast exothermic combustion reaction of Si NPs being produced during the laser ablation process, leading to their fragmentation and oxidation. A possible redox reaction taking place during the ablation process in order to produce silica and metal NPs is

$$\mathrm{Si(NP) + 4AgNO_3 + 2H_2O \rightarrow SiO_2(NP) + 4Ag(NP) + 4H^+ + 4NO_3^-}$$

In conclusion, inert gold and silver NPs shielded by silica have been successfully synthesized by using a simple technique in a single step by means of the laser ablation of a solid target immersed in a water solution of a salt containing the metal desired to form the NPs, such as $AgNO_3$, $HAuCl_4$, or mixtures of them. The method has also been validated by using several target materials such as Si, Ge, and W. The local high temperatures reached during laser ablation allow fast and efficient chemical reactions to form metal NPs, mainly spherical with sizes in the range from 3 to 18 nm. These chemical reactions together with the

(52) Wiley, B.; Herricks, T.; Sun, Y.; Xia, Y. *Nano Lett.* **2004**, *4*, 1733–1739.

oxidation of the ablated material (Si, for example) lead to the direct formation of a stable colloid from (silica) shielded metal oxide NPs. Both the silica−metal formation and the presence of silica in the colloid ensure the use of our NPs in biotechnology/biomedical applications, given their inert character and stability, as will be shown elsewhere. The proposed method has been developed by using metal salts because of the high efficiency of the reduction reaction of metallic ions to metal atoms, but the application of the method to other salts in order to obtain different NPs (semiconductor, dielectric, magnetic, ...) is also possible.

Acknowledgment. We gratefully acknowledge financial support from the Generalitat Valenciana (IMPIVA-IMCITA/2007/02 and ACOMP07-120) and the Spanish MEC through projects TEC2005-05781-C03-03 and TEC2008-06756-C03-03. E.J. thanks the MICINN for a Juan de la Cierva program fellowship.

Supporting Information Available: Information about laser ablation conditions and the nanoparticle size distribution as a function of the alloy composition. This material is available free of charge via the Internet at http://pubs.acs.org.

SUPPORTING INFORMATION

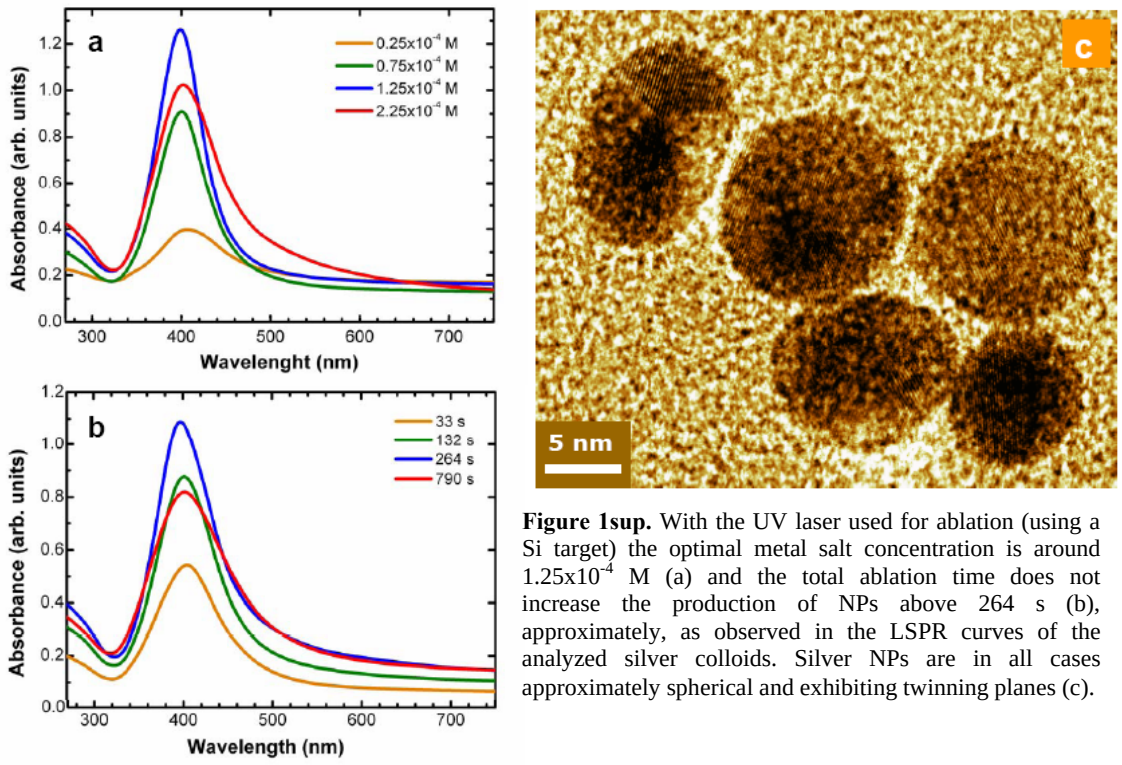

Figure 1sup. With the UV laser used for ablation (using a Si target) the optimal metal salt concentration is around $1.25x10^{-4}$ M (a) and the total ablation time does not increase the production of NPs above 264 s (b), approximately, as observed in the LSPR curves of the analyzed silver colloids. Silver NPs are in all cases approximately spherical and exhibiting twinning planes (c).

The maximum absorbance due to SPR of metal nanoparticles is achieved when using concentrations of the silver salt as low as $1.25x10^{-4}$ M. Above this concentration the LSPR intensity decreases and the resonance broadens significantly, as shown in Fig. 1sup(a). The increase of the salt concentration and hence the density of NPs obtained in the colloid produces a main effect: the increase of the light absorption and dispersion by the nanoparticles being produced that are reducing the effective laser power density at the target surface. This effect is particularly important and limits the maximum density of nanoparticles yielded by the optimal metal salt concentration (around $1.25x10^{-4}$ M). It can be observed in Fig. sup1(a) that absorbance of the colloid is around 0.45 for colloids prepared above $0.5x10^{-4}$ M, which means a reduction of laser density at the target surface by a factor three. Added to this reduction we must also take into account the refractive

index change induced by the presence of metal nanoparticles that will spread the beam waist at the target surface. Therefore, a sublinear behaviour and even saturation is expected in the maximum density of nanoparticles produced by ablating with 355 nm, because this process needs an appropriate laser density. The use of other wavelengths (532 nm or 1064 nm) for the ablation of the target can lead to higher density colloids (and hence using $AgNO_3$ concentration above $1.25x10^{-4}$ M). One would expect differences in silicon (primary) and silica (secondary) particles produced by the ablation process using other laser wavelengths.

Another relevant parameter during the laser assisted synthesis of Ag nanoparticles is the laser irradiation time (LIT), whose effect can be observed from the evolution of the LSPR spectrum in Fig. sup1(b). The increment of LIT from 33 s to 264 s (by swiping a surface of 1 cm^2 with our laser at a rate of 30 lines/s, 1000 lines/cm, that means around 150 pulses per pixel) produces an increase in the LSPR intensity, accompanied by a detectable blue shift from 401 to 397 nm and a slight linewidth narrowing, as shown in Fig. 1(d). The increase of the absorbance with the LIT is now strongly sublinear, because the colloids are produced by using the same initial solution (each experiment for a given LIT is made with a new metal salt solution). Let note that 33 s (a single 1 cm^2 surface sweep) is enough to produce half of the maximum density of nanoparticles achievable with the optimal salt concentration ($1.25x10^{-4}$ M). Above 528 s the intensity of the LSPR decreases and broadens again, which would be explained if the reduction of the metal salt is exhausted before this time interval (surely the exhaustion is taking place between 132 and 264 s). In all examined conditions to produce silver nanoparticles by using a silicon

target we obtain them with round shape, but exhibiting twining planes, as shown in Fig. sup1(c).

Fig. 2sup shows low resolution TEM micrographs to extract average diameters of Ag-Au alloy nanoparticles. The average diameter of the alloyed nanoparticle as a function of the Au weight percentage was represented in the inset of Fig. 1(d).

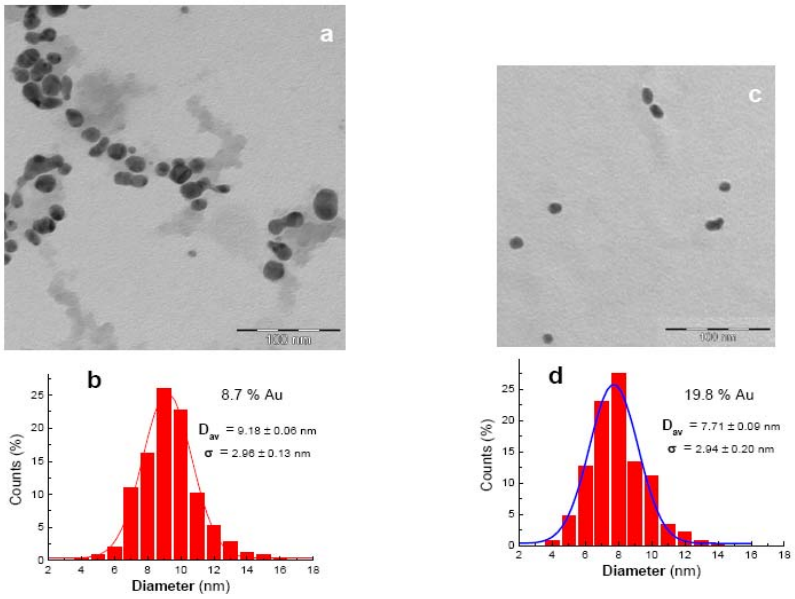

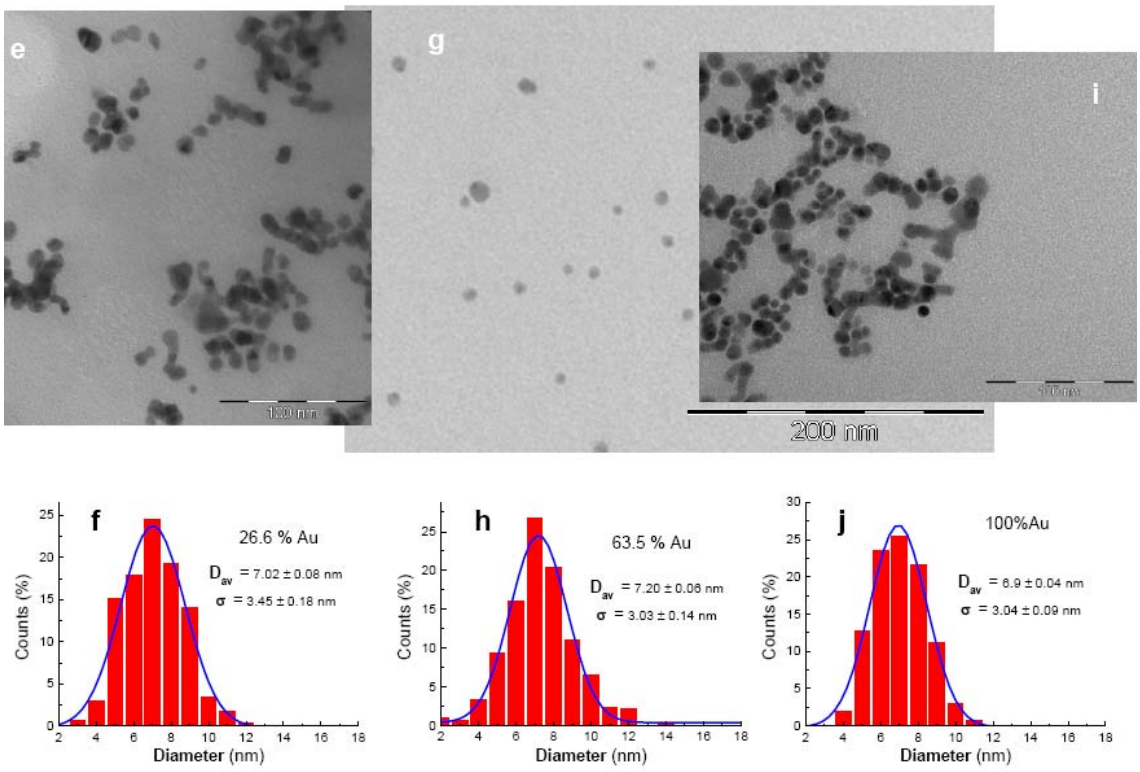

Figure 2sup. TEM images (a, c, e, g, i) and their corresponding size distribution (b, d, f, h, j) of Ag-Au nanoparticles with different Au content: 8.7% (a-b), 19.8 % (c-d), 26.6 % (e-f), 63.5 % (g-h) and pure Au (i-j).